Title

THE ELECTRICAL TRANSPORT AND MECHANICAL PROPERTIES OF TANTALUM-MOLYBDENUM ALLOY SINGLE CRYSTALS

Permalink

Author

Torne, Lenon I. Van

Publication Date

1965

University of California

Ernest O. Lawrence Radiation Laboratory

THE ELECTRICAL TRANSPORT AND MECHANICAL PROPERTIES OF
TANTALUM-MOLYBDENUM ALLOY SINGLE CRYSTALS

Berkeley, California

DISCLAIMER

UNIVERSITY OF CALIFORNIA

Lawrence Radiation Laboratory
Berkeley, California

AEC Contract No. W-7405-eng-48

THE ELECTRICAL TRANSPORT AND MECHANICAL PROPERTIES

OF TANTALUM-MOLYBDENUM ALLOY SINGLE CRYSTALS

Lenon I. Van Torne

(Ph.D. Thesis)

January 1965

Table of Contents

THE ELECTRICAL TRANSPORT AND MECHANICAL PROPERTIES

OF TANTALUM - MOLYBDENUM ALLOY SINGLE CRYSTALS

Inorganic Materials Research Division, Lawrence Radiation Laboratory,
Department of Mineral Technology, College of Engineering,
University of California, Berkeley, California

By

Lenon I. Van Torne

January 1965

ABSTRACT

The binary alloys of the refractory metals, Nb, Ta, Mo and W are reported to form complete bcc solid solutions with each other. Of the six possible binary alloys, only Nb-Ta and Mo-W are ductile at all compositions. The others show cleavage behavior at high alloy compositions. The purpose of this investigation is two fold; the first being to determine the reasons and mechanisms for the occurrence of cleavage and the second to increase the knowledge of electrical transport in transition metal alloys.

The binary alloy series Ta-Mo was selected as being representative of the alloys which show cleavage. Single crystals of the Ta-Mo series were grown at about 10 atomic percent increments by electron beam zone refining. The methods of investigation of the prepared crystals included: specific resistivity at 273°K, 77°K and 4.2°K, critical resolved shear stress for plastic flow or cleavage at 273°K, lattice parameter determination, transmission electron microscopy and quantitative

X-ray diffracted intensity measurements of {200} and {220} planes on spherical alloy single crystals.

This investigation revealed that the alloys in the composition range of Mo-19 Ta to Mo-58 Ta cleave on the {100} planes. The lattice parameter measurements and transmission electron microscopy revealed that the alloy series is bcc with no long range or short range order of a dimension greater than 300Å or intermediate phases. X-Ray diffracted intensity measurements from {200} and {220} indicate that there exists a deviation from random solid solution in the crystals. The ratio of constituent atoms on {100} and {110} differ from the ratio of atoms corresponding to the total composition of the crystal in such a way as to generate quasi-cubic domains for {100} and quasi-dodecehedral for {110} deviations. However, even though there is a deviation from random solid solution composition on particular crystallographic planes, no periodic arrangement of atoms on these planes is evident. The increase in critical resolved shear stress for plastic flow with alloy composition results from a corresponding increase in the Peierls-Nabarro friction of dislocations produced by alloying, composition deviations on {100} or {110} and concomitant changes in the elastic coefficients. Cleavage occurs due to a violation of the strain energy restrictions on the elastic coefficients in a local region of the crystal. Alloying and the existence of composition deviations change the elastic coefficients, in the range of alloys which cleave, to values which marginally fulfill the strain energy restrictions. The presence of a critical density of dislocations in a local region produces changes in the values of the

elastic coefficients such that the crystal is locally energetically unstable. The crystal then cleaves on a {100} plane which relieves the maximum strain energy.

Marked changes in the slope of $(\rho_{273°K}$ minus $\rho_{4.2°K})$ versus alloy composition at Mo-20 Ta, Mo-50 Ta and Ta-12 Mo reveal that there is a relatively large change occurring in the density of states in the d and s bands and/or marked changes in the elastic coefficients at these alloy compositions.

I. INTRODUCTION

In recent times there has been considerable theoretical and practical interest focused upon the elements niobium, tantalum, molybdenum and tungsten and the alloys formed by combinations among these four elements. There is theoretical interest in the electrical transport and mechanical properties of these transition elements and their alloys, since the mechanisms involved in the behavior of these properties is not well understood. There is interest in the practical application of these elements and their alloys, since they exhibit very high melting points which is an obvious requisite for structural materials employed in high temperature environments.

As shown in Fig. 1, these elements all possess the body centered cubic crystal structure. A preliminary investigation of the binary alloying behavior of the elements with each other have shown that all the alloys form complete bcc solid solutions.[1] However, as shown in Fig. 1 four of the six binary alloys formed by mixing between elements of group V and VI, exhibit the undesirable property of cleavage for alloy compositions in the central portion of the binary diagram.[2,3] The reasons for such behavior are not well understood.

The purpose of this investigation was to determine the origin of this behavior and the mechanisms involved, in addition to gaining new knowledge concerning bcc refractory metal alloys. To achieve this goal, several methods of investigation were employed, namely specific electrical resistivity at 273°K, 77°K and 4.2°K, tensile tests at 273°K, lattice parameter measurements, transmission electron microscopy and x-ray diffracted intensity measurements. These investigative methods were necessary in

V	VI
AT. NO. 40	AT. NO. 41
Rad. 1.43 Wt. 92.9	Rad. 1.36 Wt. 95.9
Nb	Mo
BCC M.P. 2415	BCC M.P. 2622
$4p^6\,4d^4\,5s$	$4p^6\,4d^5\,5s$
AT. NO. 73	AT. NO. 74
Rad. 1.43 Wt. 180.9	Rad. 1.37 Wt. 183.9
Ta	W
BCC M.P. 2996	BCC M.P. 3395
$5d^3\,6s^2$	$5d^4\,6s^2$

Nb ⇄ CLEAVAGE ⇄ Mo

FLOW — CLEAVAGE — FLOW

Ta ⇄ CLEAVAGE ⇄ W

MECHANICAL BEHAVIOR NEAR I·I COMPOSITIONS

MUB-4438

Fig. 1.

order to determine if the observed physical behavior was produced by any one or a combination of the following:

    a. Interstitial impurity effects which immobilize dislocations.

    b. Presence of brittle intermediate phases which form planes of weakness.

    c. Long-range or short-range order.

    d. Demixing such as presence of miscibility gaps.

    e. Large increases in the Peierls-Nabarro friction of dislocations.

Of the four binary bcc solid solution alloys of interest which show the cleavage behavior, Nb-W, Nb-Mo, Ta-W and Ta-Mo, the binary alloy system Ta-Mo was selected for detailed investigation. This alloy system was chosen because of the large difference in x-ray and electron scattering factor and the closeness of the melting points of the two constituents. Three crystals of Nb-W were grown, but the number of electron beam zone passes necessary to achieve the desired purity level was more than the number required for Ta-Mo. Since many crystals were required for the investigations, an appreciable saving in crystal preparation time was obtained by using the Ta-Mo alloy system.

II. EXPERIMENTAL PROCEDURE AND RESULTS

In this investigation several series of experiments were carried out. Therefore, the particular experimental procedure and the results obtained therefrom are presented together in this section in order to show exactly how the data was taken.

II-A. Preparation of the Alloy Single Crystals

In investigations of body-centered-cubic metallic crystals special consideration must be given to the preparation of the alloys with regard to interstitial impurities. It is common knowledge that interstitial impurities such as oxygen, carbon, nitrogen and hydrogen exert a marked influence on the electrical transport and mechanical properties of bcc metals and alloys. Due to their high affinity, it is difficult to obtain pure materials. In investigations involving the refractory metals, e.g. those metals having melting points greater than 1800°C, there exists the additional difficulty in achieving the temperature and conditions necessary for growing single crystals.

II-A-1. Description of Electron Beam Zone Refiner

In 1956 Calverley[4] applied electron beam heating to the principle of floating zone refining and since that time the technique has been improved to the present state. Refractory metal and alloy single crystals can be prepared in a very pure state using this technique.

An electron beam zone refiner was designed and constructed in order to prepare the alloy single crystals used in this investigation and in subsequent investigations of bcc refractory metals and alloys.

An electron beam zone refiner can be described in terms of three general features; the electronic power supply and regulation, the
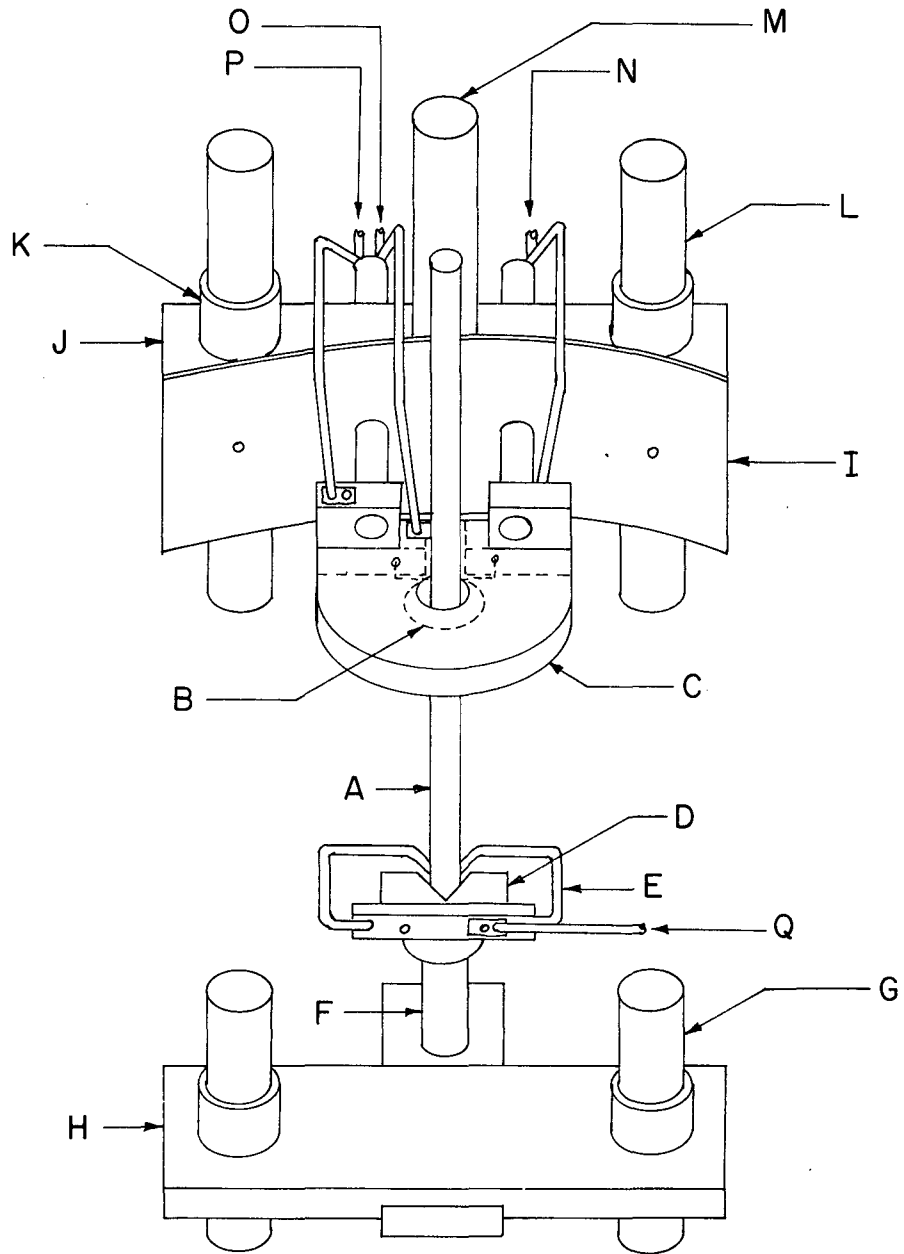
Fig. 2.

MUB-4439

mechanical design and vacuum system. The main features of the mechanical

design are shown in Fig. 2. The specimen to be zone refined (A) is

mounted in Ta "V" blocks (D) by a Ta clip (E). Only the lower specimen

chuck is shown in the figure, since the upper specimen chuck is identical

in design. The electron gun assembly, composed of the electron emitter (B)

contained within a Ta electrostatic deflection can (C) is mounted on a

translation carriage (J), by two ceramic rods. The emitter heating

current passes through the Cu rod (P) and over the translation carriage (J)

to a Ta block to which one side of the emitter is fastened by means of a

set screw. The continuity of the emitter heating current path is through

a Cu rod (N). The Cu rod (O) maintains the electrostatic deflection plate

at the same potential as the emitter, i.e. at a high negative potential

with the specimen maintained at zero potential. However, since the

specimen is insulated from the unit through ceramic rod (F) and the specimen

heating (the electron beam current) flows through Cu rod (Q), the specimen

can be held at a high negative potential. The translation carriage (J)

rides on honed stainless steel guide rods (L) through ball-bearing bush-

ings (K). Translation of the carriage is produced by the honed stainless

steel rod (M) which passes through the vacuum chamber by means of a

quad-ring vacuum seal. A gear rack and pinion are attached to rod (M) exterior

to the vacuum system. A Bodine electric motor and a Zeromax transmission

are used to move the rod (M) up or down at any speed between 0 and 1

inch/min. The position of the carriage can be set manually by moving

the speed selection lever of the Zeromax. The upper specimen chuck can

be manually moved from outside the vacuum, this being a necessary feature

since the specimen is mounted in the chucks in two sections in order to

achieve correct alignment. The upper and lower specimen chucks ride on

guide rods (G) in the same way as the translation carriage described above. The entire zone refiner mechanism is suspended from a thirteen-inch diameter stainless steel flange by the guide rods. The supporting flange rests upon a twelve-inch diameter pyrex cylinder. The vacuum seal between flange and pyrex cylinder is made through an "L" section gasket.

The vacuum system employed was sufficient to maintain the pressure within the chamber at less than 10^{-5} torr during the first fusion pass. After the first pass the pressure remained near 10^{-6} torr. The vacuum ion gauge was mounted in the chamber, and even though it is recognized that the pressure in the region of the emitter can be greater than the gauge reading, the pumping speed of the vacuum system is sufficient to make this difference a minimum. Backstreaming from the diffusion pump into the chamber was maintained at a minimum by a refrigerated chevron baffle trap.

The success or failure of an electron beam zone refiner is determined by the ability to maintain the energy supplied to the molten zone within narrow limits ($\pm 1\%$). This is a consequence of the fact that the molten zone is supported by surface tension forces. The ability to regulate the energy supplied to the specimen as one approaches the melting point is as important as maintaining the energy within narrow limits after the specimen has melted. The modes of operation of an electron beam zone refiner have been analyzed and are lucidly discussed by Sell and Grimes.[5] They advocate regulation of the beam energy on the dc side of the electronic system. The energy regulation system used in this zone refiner was constructed with due consideration given to the recommendations in their paper. The performance of the system has met all expectations.

Since the high voltage and electron beam current employed in zoning

a given specimen depend on the material and specimen geometry, no particular

values will be given. However, the maximum output of the power supply is

10 kV dc at 1.5 amp. The maximum power used up to the present time was

6 kV at 0.5 amp. which was used for zoning a 0.250 in. diameter tungsten

rod.

Purification by an electron beam zone refiner results from the high

energy of the electron beam which is capable of decomposing the most stable

compounds in the presence of a high vacuum. It is believed that the com-

pounds decompose yielding gaseous products. These gas products are re-

moved from the region of the melt by the vacuum system. Therefore the

ultimate level of purity is dependent upon the quality of the vacuum in

the region of the melt and the ability to superheat the melt. However,

there is the problem of large losses of metal through evaporation if the

pressure of the system decreases far below the equilibrium vapor pressure

of the melt and the pumping speed is high.

The efficiency of this zone refiner was demonstrated by two examples.

A 90% TaC (MP $\approx$ 4000°C)-10% NbC rod was given one molten zone pass. The

result of this pass was to produce a ductile metal rod. This demonstrates

that even the most stable compounds can be decomposed and then removed by

the vacuum from the system. The second example is the attainment of large

values of the resistivity ratio, e.g. $\rho_{273°K}/\rho_{4.2°K}$, in Ta crystals. A

value of 10,000 was measured on a Ta crystal which corresponds to a

residual level of interstitials equal to 3 impurity atoms in 10^9 matrix

atoms. See Appendix II for this calculation.

II-A-2. Growth of Ta-Mo Single Crystals

Several different diameter Ta and Mo rods of commerical purity were

obtained. The number of Ta or Mo atoms in unit length of a rod of given diameter can be computed in a straightforward manner. From the results of such computation a combination of rod diameters is selected to give the desired alloy composition. In this investigation 10-at% increments were desired, however, this was not always achieved because of the limited choice of rod diameters. Since the alloy compositions attainable from the choice of available rod diameters was considered to be a sufficient representation of the binary diagram, the effort necessary in machining the rods to a particular diameter to achieve exact 10 at.% increments was unjustified.

The selected combination of 6 in. long Ta and Mo rods were bound together near the rod ends with 0.020 in. diameter Ta wire. This combination was then clipped into the specimen chucks of the refiner and given three passes (1 in./min.) at a temperature of about 200°C below the melting point of the lower melting constituent in order to remove as much residual gases as is possible without melting. Next, a fusion pass is made at 1 in./4 min. to consolidate the rod combination. During this pass a considerable amount of impurities are removed by the vacuum system as evidenced by an increase in pressure to about $3-4 \times 10^{-5}$ torr. The second zone melting pass is initiated at the lower end of the rod. The molten zone is held stationary in order to allow one crystal, in contact with the melt, to dominate all others. Following this incubation period the molten zone is moved along the rod at a speed of 3 in./hour. The rod is zoned in both directions in order to alleviate any tendency to concentrate either alloy constituent at one end of the rod. Since that portion of the crystal immediately adjacent to the molten zone is about 50°C below the melting point, the atoms in this region are very mobile and thus seek

their equilibrium positions in a crystal in a time that is short compared to the time for the melt interface to move an incremental distance. Also, there exists a moving temperature gradient along the length of the rod behind and in front of the molten zone. This moving temperature gradient ensures that the crystal is in a state compatible with slow cooling. The molten zone is observed to be in a continually agitated state. This is a beneficial phenomenon, since it promotes complete mixing of the alloy constituents and assures a homogeneous crystal.

II-A-3. Proof of Single Crystallinity

There are several ways to judge whether one has been successful in growing a single crystal. These tests were always made, and now will be discussed. Thermal etching of crystal boundaries has been observed on polycrystalline specimens of this alloy series. Polycrystalline specimens are easily obtained by moving the molten zone at excessive speeds. Therefore, the first check for single crystallinity is a visual inspection of the crystal surface under a microscope at 30X magnification. If the crystal passes this inspection, it is then placed in an electropolishing bath with the current set at a value which produces severe etching of crystal boundaries. If the crystal passes the second test, then regions of the crystal are examined by taking back reflection Laue patterns using a large pinhole (0.050 in.). The large pinhole is used to sample a larger area of the crystal. The latter test furnished information concerning small angle boundaries, since these boundaries split the Laue diffraction spots.

A shift in the alloy composition by preferential evaporation of one alloy constituent has been considered and is estimated to be negligible, i.e., less than 1 at.% either way. However, this effect could become

Water coolant

Crystal

Chuck

Cup center

0.50 rpm

1650 rpm

Brass wheel

240-grit
emery cloth

Mechanical Polish Fixture

0.115 in.

0.090 – 0.085 in.

Crystal as
cut

├─1.0 in.─┤
(after mechanical
polish)

├─1.0 in.─┤
(after
electropolish)

Specimen Geometry
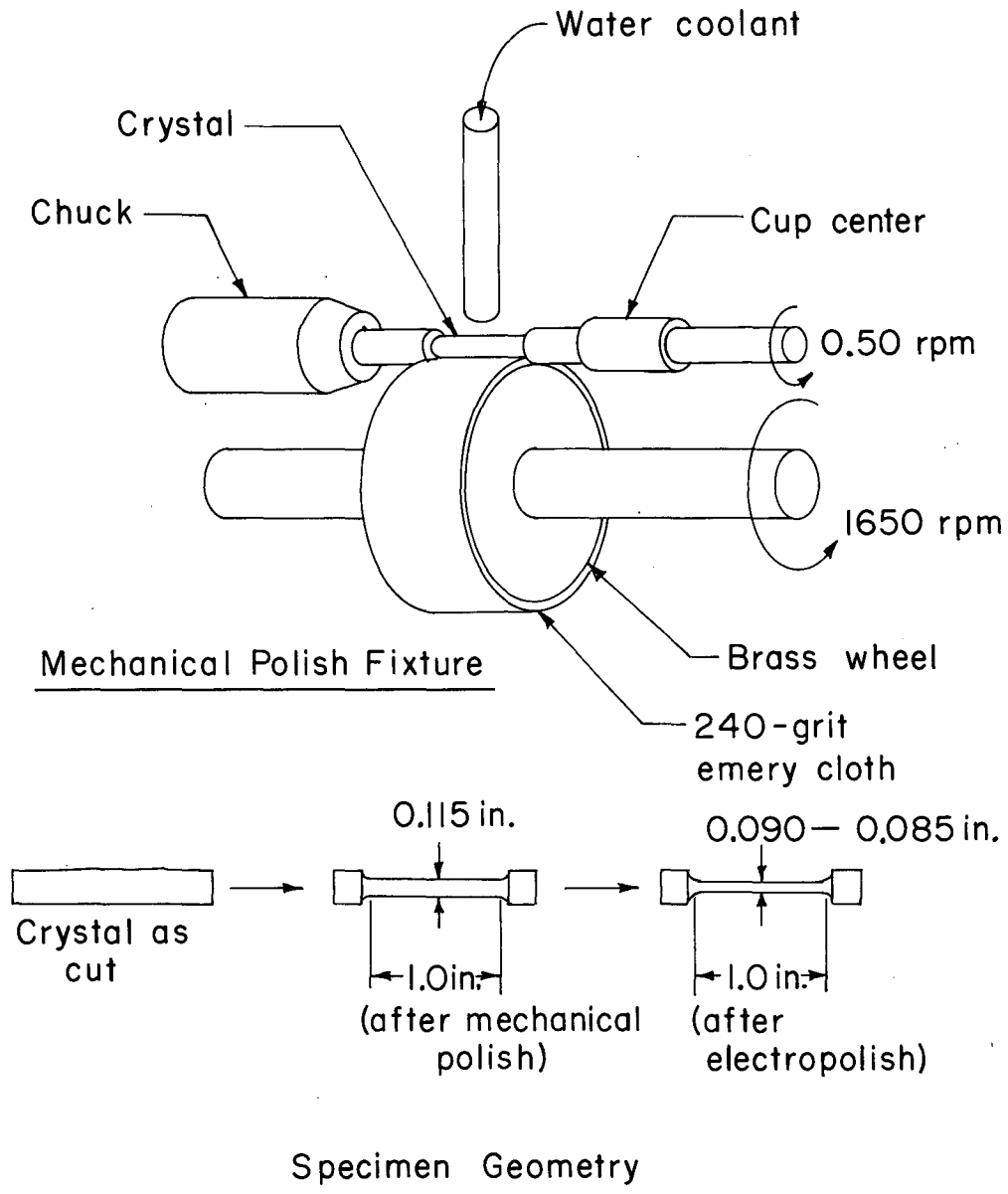
MUB-4440

Fig. 3.

appreciable in alloys containing high vapor pressure constituents such as chromium and vanadium.

II-B. Procedure for Obtaining a Uniform Single Crystal Cross-Section

It is necessary to have a uniform cross section over a considerable length of crystal in order to make specific resistivity and critical resolved shear stress measurements. Since the as grown crystals were not uniform in section to the degree desired, the procedure discussed below was developed.

II-B-1. Cutting of Single Crystal Sections

Since the total length of zone refined crystal was in excess of four inches, a method for cutting shorter sections was needed. Sections of about one and five-eighths in. were cut by two methods. The zone refined crystal was rigidly cemented to a wooden block. Crystal sections of the end members of the binary alloy series as well as the ductile alloys were cut with a jeweler's saw having 60 teeth to the inch. Crystal sections of the brittle members of the alloy series were cut with a diamond saw using a flowing stream of kerosene as coolant.

II-B-2. Mechanical Polishing the Crystals

The mechanical polishing fixture which was used for all the crystals in this investigation is sketched in Fig. 3. The cup center shown in the figure is spring loaded in order to prevent bending moments arising from binding of the crystal. The force the crystal exerts upon the polishing wheel is adjustable from zero to about five pounds by means of a counterweight and a lead screw. By adjusting the lead screw the diameter of the crystal can be decreased at a

rate of about 0.001 in./min. A steady stream of water applied to the crystal surface prevents heating of the crystal and promotes a smooth surface. The crystal section is reduced to the dimensions given in the figure by mechanical polishing. Any damage incurred to the surface of the crystal during mechanical polishing is removed by electropolishing as described in the following paragraph.

II-B-3. Electropolishing the Reduced Crystal Section

From 0.025 to 0.030 in. was removed from the diameter of each crystal by electropolishing. The Mo crystal was electropolished in a 60% conc. H_2SO_4-40% H_2O polishing solution at a current density of 1.9 amps/in^2. The remaining crystals were electropolished in an 80% conc. H_2SO_4-20% conc. HF polishing solution at the same current density. It was observed that the concentration of HF in this solution was not critical and equally good polishes were obtained with HF concentrations in the range 10% to 40%. The dissolution rates of Mo, Mo-7Ta and Ta were observed to be anisotropic as was evidenced by dissolution figures whose patterns showed the point symmetry of the crystal and by deviations in the diameter of the crystal cross section of about ±0.002 in. The geometric arrangement of the diameter deviations had four-fold symmetry.

The back reflection Laue diffraction spots of the crystals after electropolishing showed no asterisim, thus indicating that any surface damage incurred during mechanical polishing had been removed.

II-C. Resistivity Measurements

Electrical resistivity measurements of an alloy series is a

traditional method of metallurgical investigation. A graph of the specific electrical resistivity versus alloy composition will indicate the presence of second phases, intermediate compounds, and $\ldots$ ordering through the appearance of inflection points or $\ldots$ plateaus in the graph. The specific resistivities of the alloys under investigation were determined at 273°K, 77°K and 4.2°K.

II-C-1. Instruments for Resistivity Measurements

The specific resistivity of each crystal was measured at 273°K, 77°K and 4.2°K using the d.c. method and applying Ohm's Law.

Ohm's Law can be written

$$\rho = \frac{E}{I} \frac{A}{L}$$

where ρ is the specific resistivity of the crystal,

A is the cross section area normal to the current I flowing through the crystal and

E is the potential developed between two points parallel to the direction of I and separated by a distance L.

The dc current was supplied by a 30 amp. Regatron solid-state power supply operated in the constant current mode. An external resistor is required to operate the power supply in the constant current mode. A Leeds and Northrup 0.01 ohm, 100 amp. resistor was employed for this purpose. This resistor served a dual purpose, the

first as external resistor for the constant current power supply, and the second as a guage for measuring the current flowing through the crystal by measuring the potential developed across it. This resistor can be considered to be an isothermal resistor since it is thermally massive. A leeds and Northrup millivolt potentiometer having a sensitivity of ± 0.1 millivolt was used to measure the potential developed across the 0.01 ohm external resistor described above. After the thirty minute "warm up" time the current was observed to remain constant to one part in one thousand.

The potential developed along the length of the crystal was measured with a Rubicon six dial thermo-free potentiometer. This potentiometer demonstrated the ability to detect changes in potential of ten nanovolts.

An Astrodata Model 121RZ nanovoltmeter was used to determine the null point. This instrument has a sensitivity of two nanovolts per millimeter. However, even though OFHC copper leads were used with low thermal emf solder at connections between crystal and potentiometer and gold leads between potentiometer and null detector, the noise level indicated on the null detector was ± five nanovolts. This was the noise level remaining after warm up. By passing currents of from 0.900 to 9.000 amps through the crystal, the potential developed along the crystal was greater than one hundred nanovolts in all measurements therefore the noise level was negligible compared to the signal.

For resistivity measurements at 273°K, an ice and distilled water bath was used. A liquid nitrogen bath was used for the 77°K measurement and a Hofman ten leter liquid He dewar was used for the 4.2°K

measurement. In all measurements the dewar probe with attached

potential probe fixture remained in the temperature environment for a

period of not less than twenty minutes prior to making the measurement.

This procedure ensured that the crystal was at the same temperature as

the enclosing media.

II-C-2. Potential Probe and Current Lead Fixture

The potential probe and current lead fixture designed and con-

structed for the series of resistivity measurements is shown in Fig. 4.

This fixture was used for resistivity measurements at 273°K, 77°K and

4.2°K.

In the figure, the dewar probe (A) is constructed from a one

and three-eighths diameter stainless steel tube. The carriages and

ways of the potential probe fixture are constructed of polyvinylchloride.

The two carriages (B) serve the dual purpose of current lead connections

and to hold the crystal in the "V" groove of the way when measurements

are made on long (six inches) crystals. The crystals of this investiga-

tion were no longer than one and five-eighths inches, therefore the

carriage with current lead screws (C) and potential probes (D) was

more efficient. The current is carried to the crystal through thirty

strands of number thirty Formvar copper wire. These current leads

terminate in clips which are fastened to the brass screws (C). The

bundle of current leads which attach to the lower end of the crystal

pass through the slot (E) in the way. The current leads are "fluffed"

in the interior of the dewar probe in order to take advantage of the

cooling effect of the evaporated helium emerging from the dewar. This

Potential Probe Fixture

Section of Potential Probe Carriage
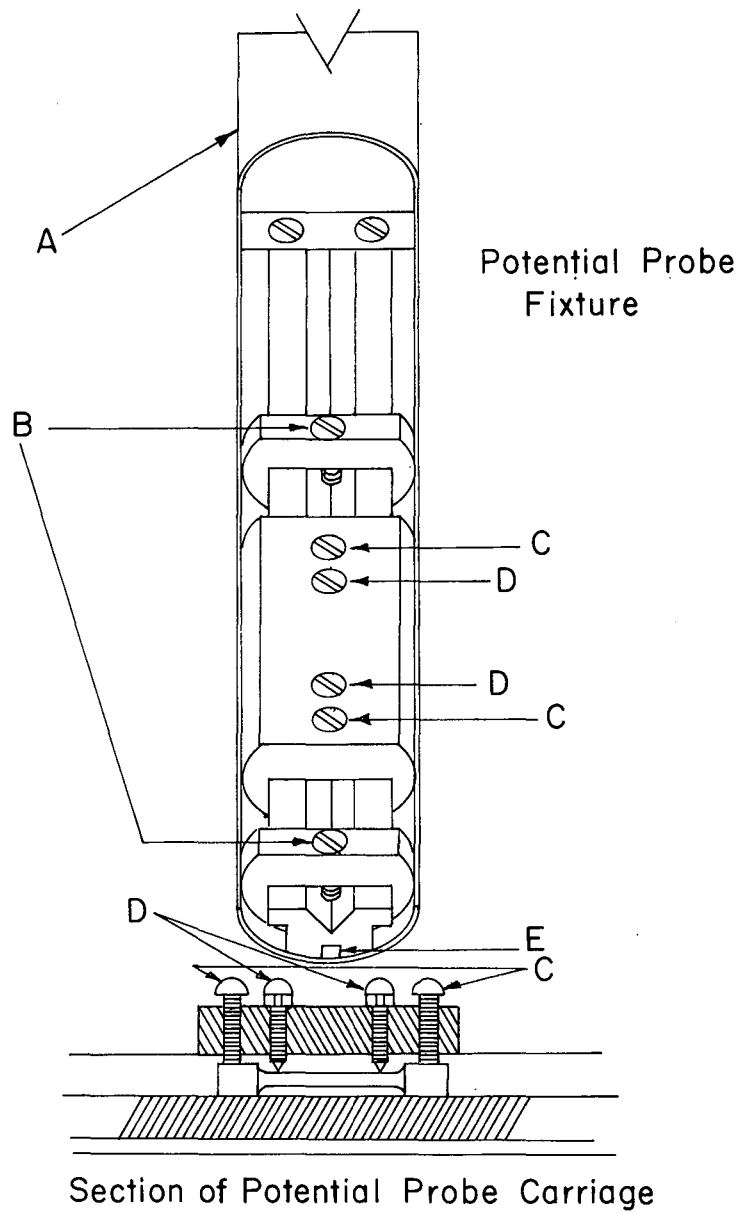
MUB-4441

Fig. 4.

procedure held the liquid helium consumption to about one liter per measurement. The resistivity measurement at 77°K also served to precool the fixture for the measurement at 4.2°K.

The potential signal was taken from the crystal through the press fit steel points inserted in the brass screws (D). The signal is carried up through the dewar probe by two number thirty Formvar wires. The surfaces of the two screw heads (D) and attached nuts are coated with low emf solder. The potential signal heads are also coated with low emf solder and are compressed between the screw heads (D) and attached nuts.

In order to measure the resistivity of the Ta crystal, it was necessary to increase the current to a value exceeding the superconducting critical current density. The superconducting transition temperature of Ta is 4.5°K and an increase from 5.510 to 8.920 amps, for this crystal cross section, was necessary to exceed the critical current density. When the current was increased to 9.582 amps. the crystal "decoupled" from the liquid helium as was indicated by an unsteady null.

II-C-3. <u>Determination of Crystal Cross Section and Potential Probe</u>
<u>Separation</u>

The diameter of the reduced section of the crystals was measured in more than ten positions with a micrometer having a sensitivity of 0.0001 inch. The diameter used in the computation of the cross section area was the arithmetical average of these ten measurements.

The steel points of the potential probes placed permanent "pip" marks on the crystal surface. These pips give the exact points of

contact of the potential probe and the separation of these marks is the length of the crystal over which the potential is measured. This length was measured with a traveling microscope having a sensitivity of ±0.0001 in.

The contribution to the resistivity produced by thermal volumetric contraction over the temperature range of the measurements was calculated to be a negligible fraction of the total resistivity measured.

II-C-4. Specific Resistivities at 273°K, 77°K and 4.2°K

Upon giving due consideration to the sensitivity of the electronic measurement instruments and the sensitivity of the dimension measuring instruments, the maximum error in each resistivity value shown in Table I is estimated to be less than one-half of one per cent.

Figure 5 is a graph of the specific resistivities given in Table I versus alloy composition. It is immediately obvious from the figure that the specific resistivity at 273°K, i.e. $\rho_{273°K}$, approximates to a linear function of the atomic per cent Ta up to and including 50 atomic per cent Ta. The slope of this line is 0.394 ($\mu \Omega$ cm). In the Ta base alloys, $\rho 237°K$ nearly obeys the classical parabolic relation except for alloy Ta-12Mo. A detailed discussion of the features of this graph will be given in the Discussion of Results.

The increase in resistivity arising from an increase in temperature from 4.2°K to 273°K is due to an increase in the frequency and magnitude of electron wave scattering. Electron wave scattering events are proportional to the frequency and amplitude of atomic vibrations in the crystal. The amplitude of vibration of an atom in a crystal is directly related to the elastic constants of the crystal, i.e. the

Table I Specific Resistivities ($\mu\Omega$-centimeters)

Alloy	$\rho 273°K$	$\rho 77°K$	$\rho 4.2°K$
Mo	5.02	0.435	0.00588
Mo-7 Ta	7.43	3.22	2.61
Mo-19 Ta	11.8	7.76	7.16
Mo-28 Ta	17.3	12.8	11.9
Mo-40 Ta	21.2	15.9	14.9
Ta-50 Mo	25.7	19.4	18.0
Ta-42 Mo	25.5	19.1	17.7
Ta-30 Mo	23.0	15.7	13.7
Ta-21 Mo	20.5	11.6	9.35
Ta-12 Mo	19.9	10.1	7.54
Ta	12.2	2.34	0.00127

Fig. 5

MUB-4442

$\rho_{273°K} - \rho_{4.2°K}$
vs Alloy Composition

Maximum error is
enclosed by symbol

$\rho_{273°K} - \rho_{4.2°K}$
$(\mu\Omega\ cm)$

Atomic percent tantalum
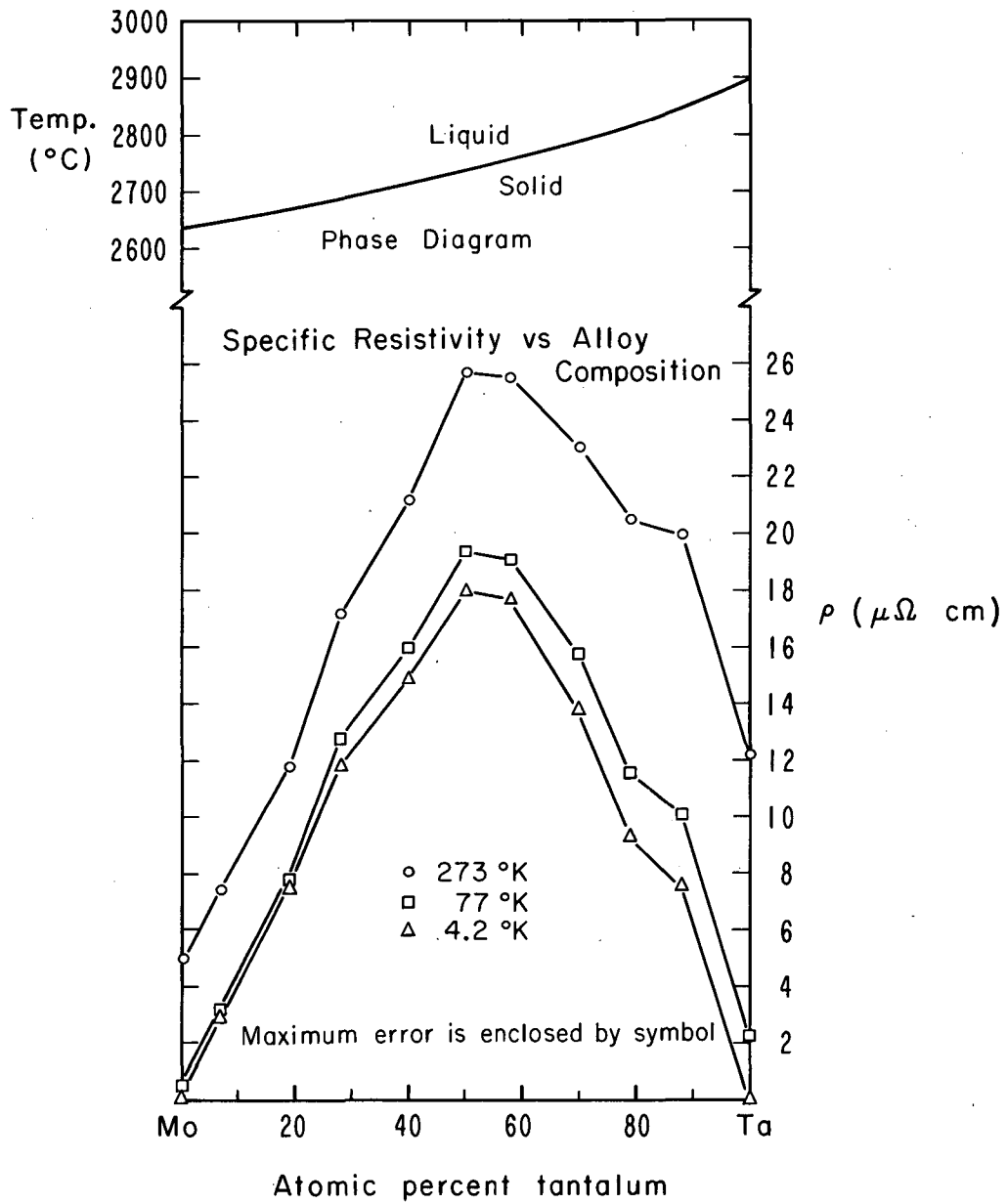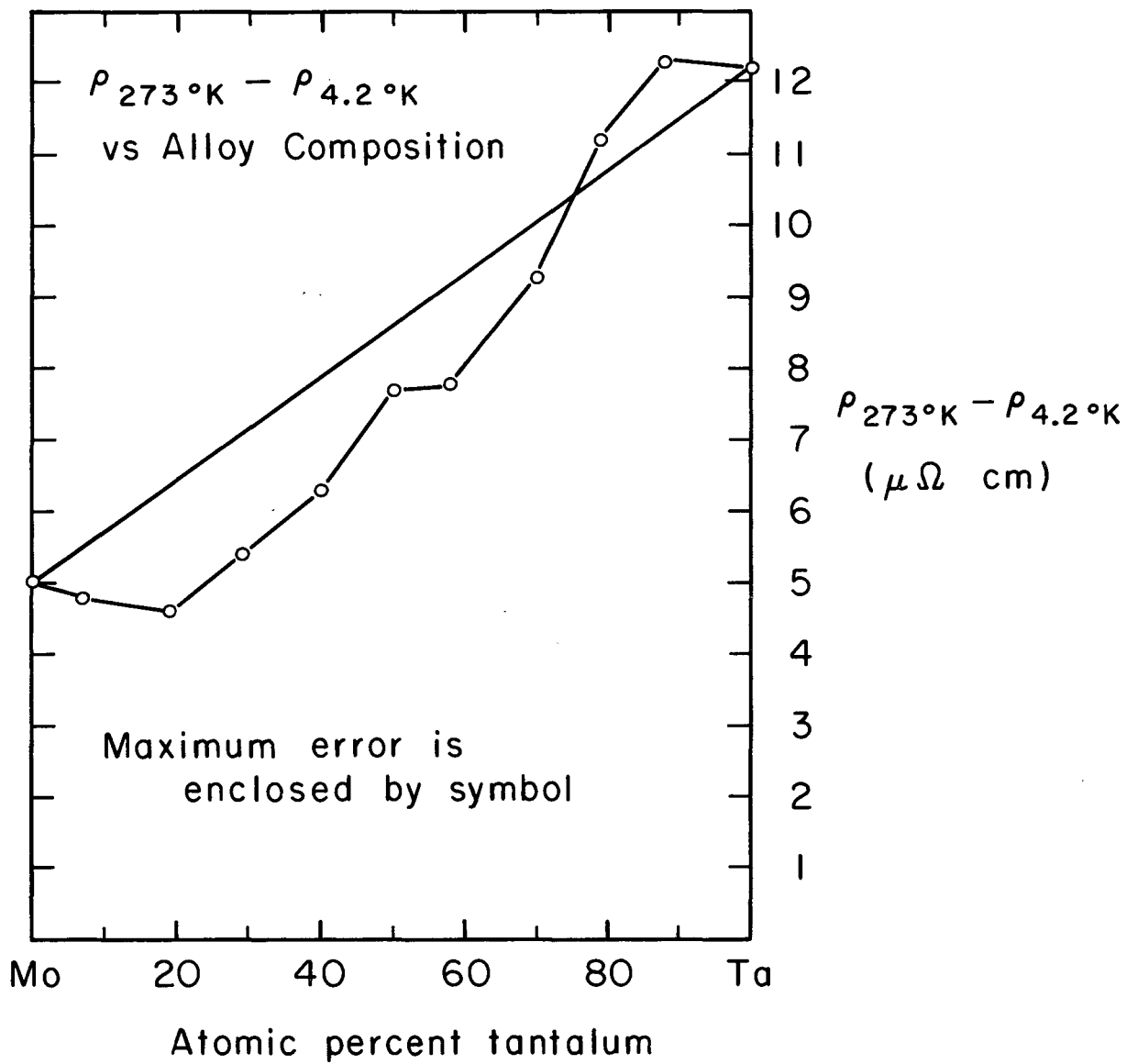
MUB-4443

Fig. 6

elastic compliances and their inverse the elastic stiffnesses. Therefore, a graph of $\rho_{273°K}$ minus $\rho_{4.2°K}$ gives a qualitative indication of the way the elastic constants vary with the alloy composition. A graph of $\rho_{273°K}$ minus $\rho_{4.2°K}$ versus alloy composition is shown in Fig. 6. There appears to be a large change in slope in this curve in the region between Ta-50 Mo and Ta-42 Mo, and at Ta-12 Mo and Mo-19 Ta. The features of this graph will be fully discussed in the Discussion of Results.

II-D. Resolved Shear Stress Measurements

Tensile tests were made at 273°K in order to determine within which regions of the binary alloy diagram what mode of crystal behavior under a tensile load predominates. Three possible modes of behavior of a crystal upon application of a tensile force are plastic flow, cleavage and mechanical twinning or a combination of any or all of these.

II-D-1. Determination of Tensile Axis Orientation

To determine the components of applied stress on a given crystallographic plane and in a direction contained in that plane or normal to it, the tensile axis must be known prior to application of the tensile load.

The tensile axis orientation fixture shown in Fig. 7 was used to make X-Ray Laue back reflection photographs of the crystal. As can be seen from the figure, the center of the Laue photograph corresponds to the intersection of a line normal to the tensile axis. The Laue patterns were solved by the method of zones described by Cullity.[6] In this geometric arrangement of crystal and Laue photograph, the

Tensile Axis Orientation Fixture

Crystal fixture

Crystal

Camera track

Laue flim frame

X-ray beam

Pinhole

Film frame fixture
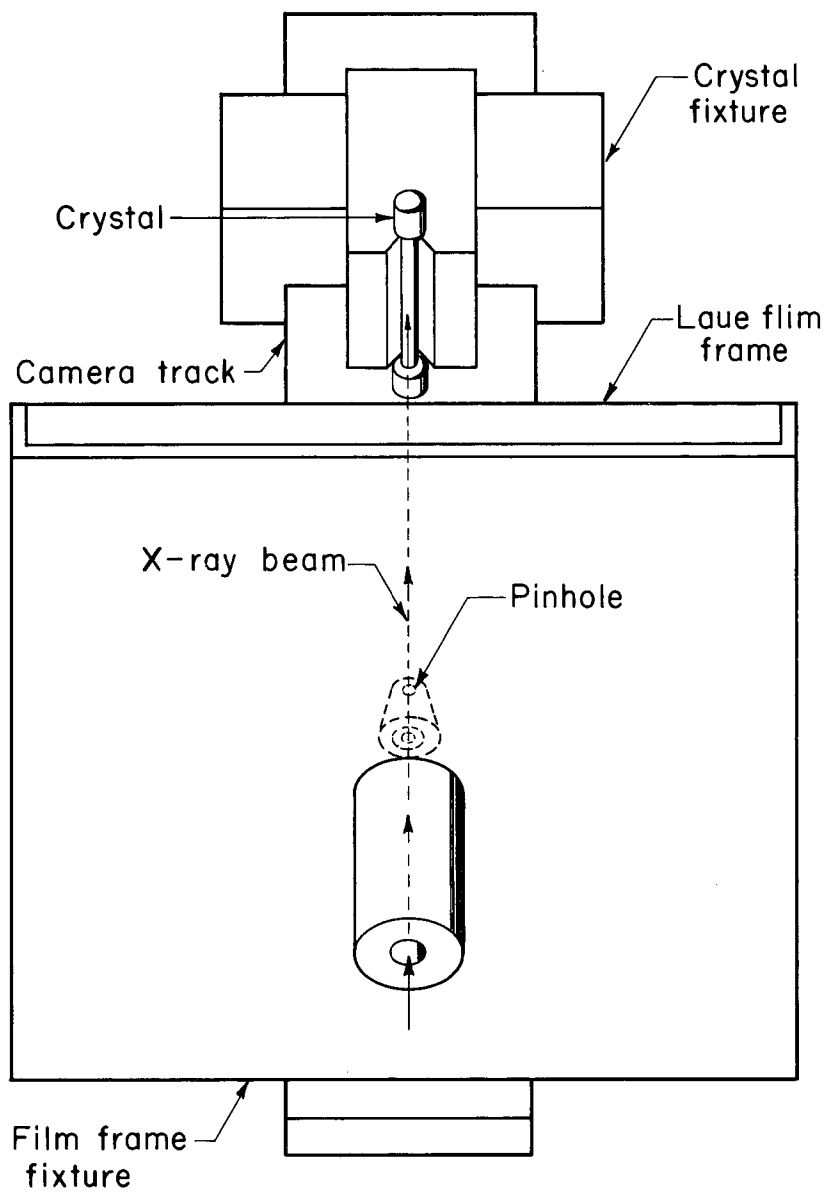
MUB-4444

Fig. 7.

tensile axis coincides with the north pole of the stereographic projection obtained from the solution of the pattern by the method of zones.

The tensile axis of all the crystals investigated prior to the tensile test are plotted in the stereographic triangle of Fig. 8. The maximum deviation of each point is estimated to be less than or equal to two degrees.

A set of tensile grips were constructed for this series of tensile tests as shown in Fig. 9. The reduced section of the crystal has an all around clearance of 0.004 in. from the grip. The grip makes contact with the shoulders of the crystal as shown in the figure. The assembled grips and crystal were connected to a floor model Instron tensile testing machine through a system of linkages, pins and universal joints. The grips and crystal were completely immersed in a dewar of ice and distilled water. A period of twenty minutes was allowed to elapse prior to testing to allow the system to come to the temperature of the bath (273°K). The strain rate for all tensile tests was 3.33×10^{-4}, per sec.

The tensile curve of a crystal which deforms by plastic flow is shown in Fig. 10. No significance can be attached to the per cent elongation, since the crystal "necks" and thus the strain is heterogeneous. Fig. 11 shows the tensile curve of a crystal which deforms predominantly by cleavage. All of the crystals that failed by cleavage showed some slip lines on their surfaces at a 30X magnification. An analysis of these slip lines could not be made since the crystals are cylinders and circular in cross section. The very slight serrations
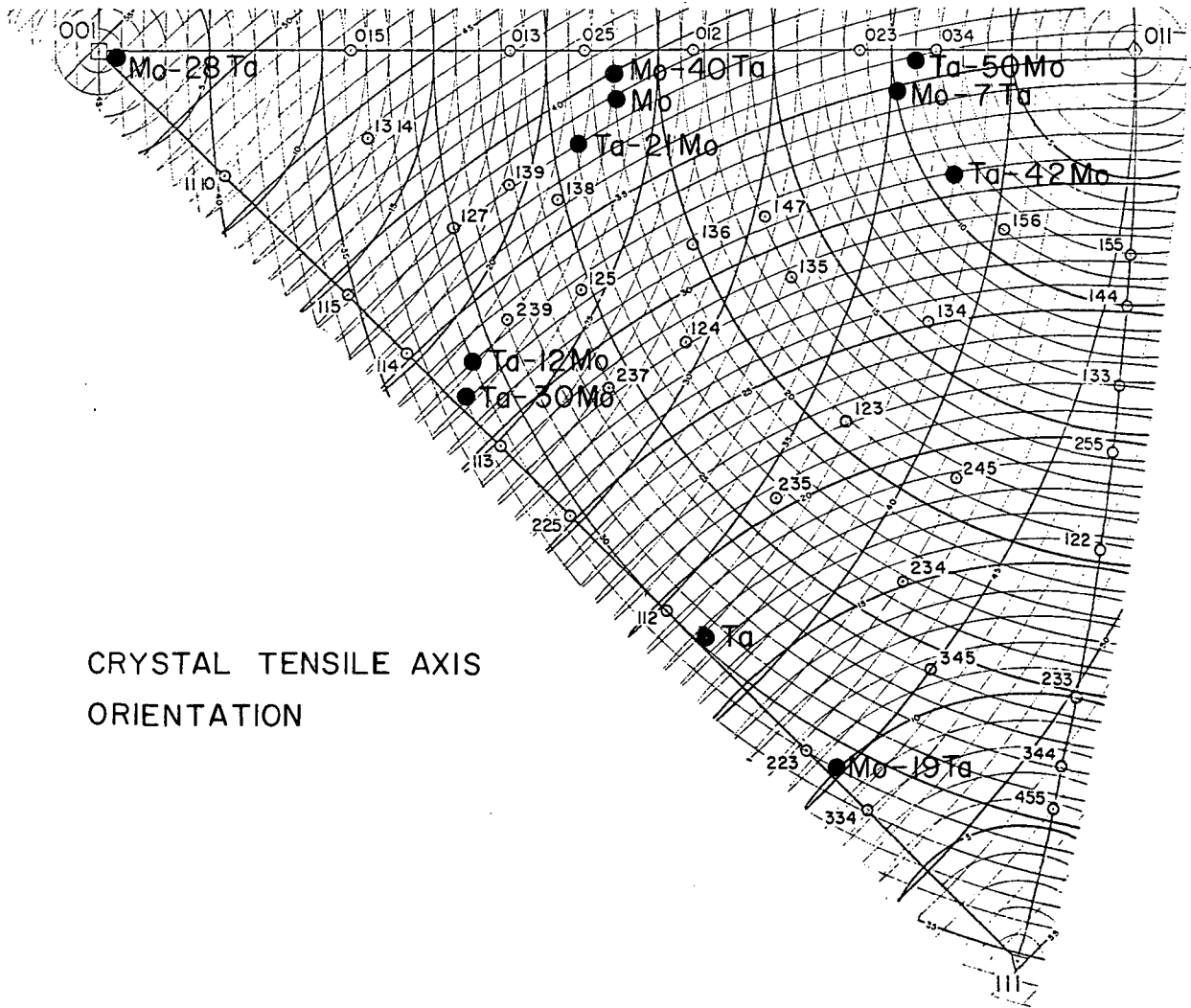
CRYSTAL TENSILE AXIS
ORIENTATION

MUB-4432

Fig. 8.

Tensile Grip Assembly

Half of upper grip

Half of lower grip

Tensile grip assembled

Tensile grips open showing crystal in place
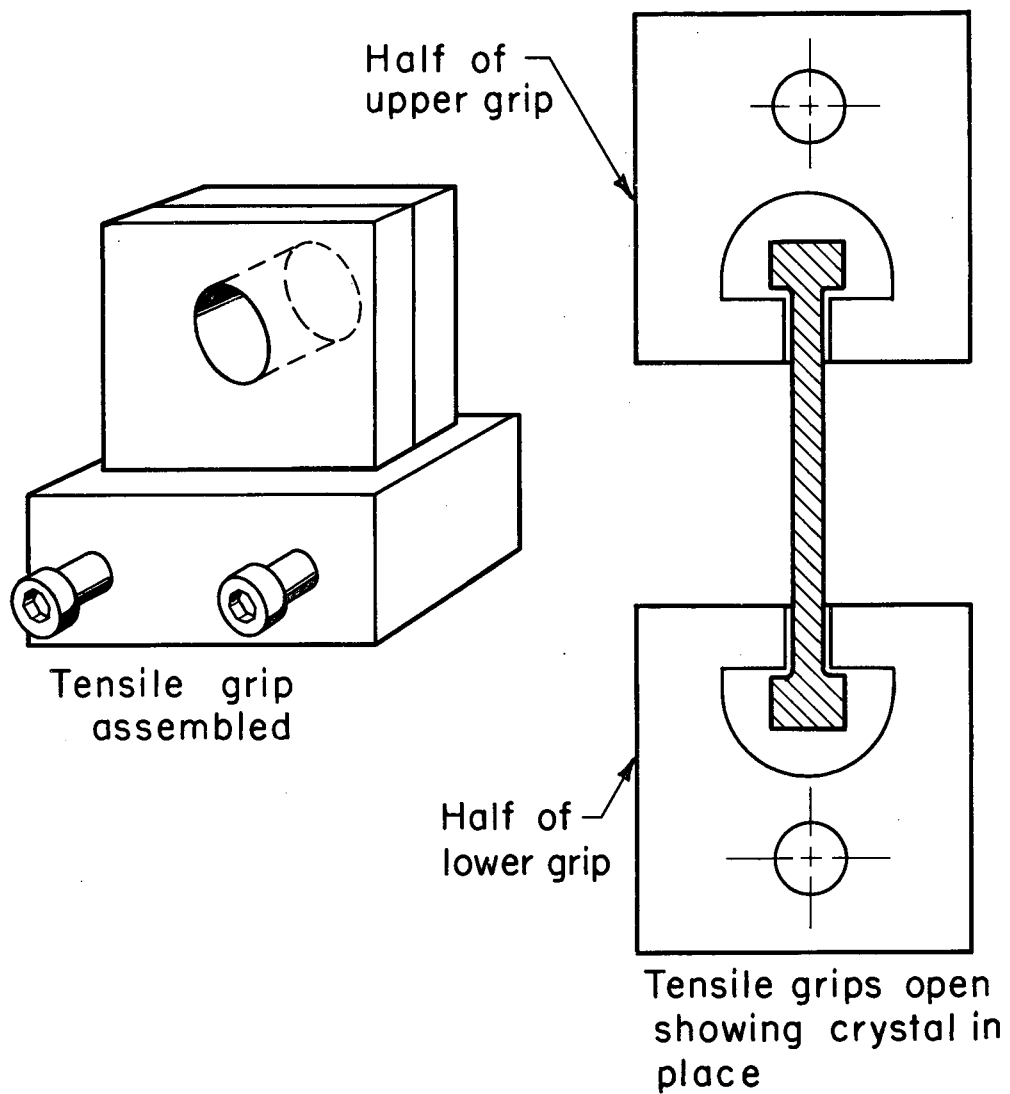
MUB-4445

Fig. 9.
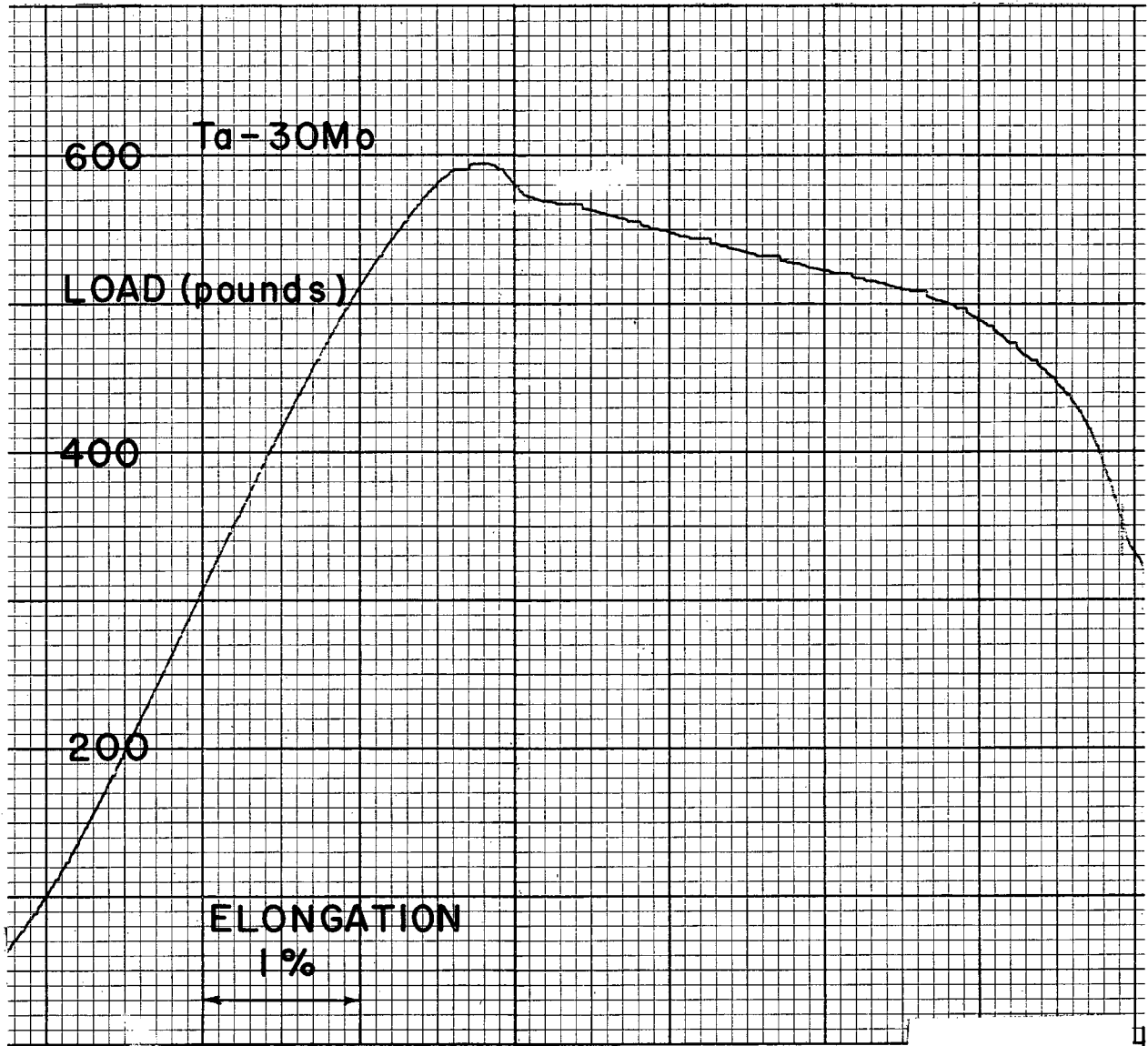
Fig. 10.
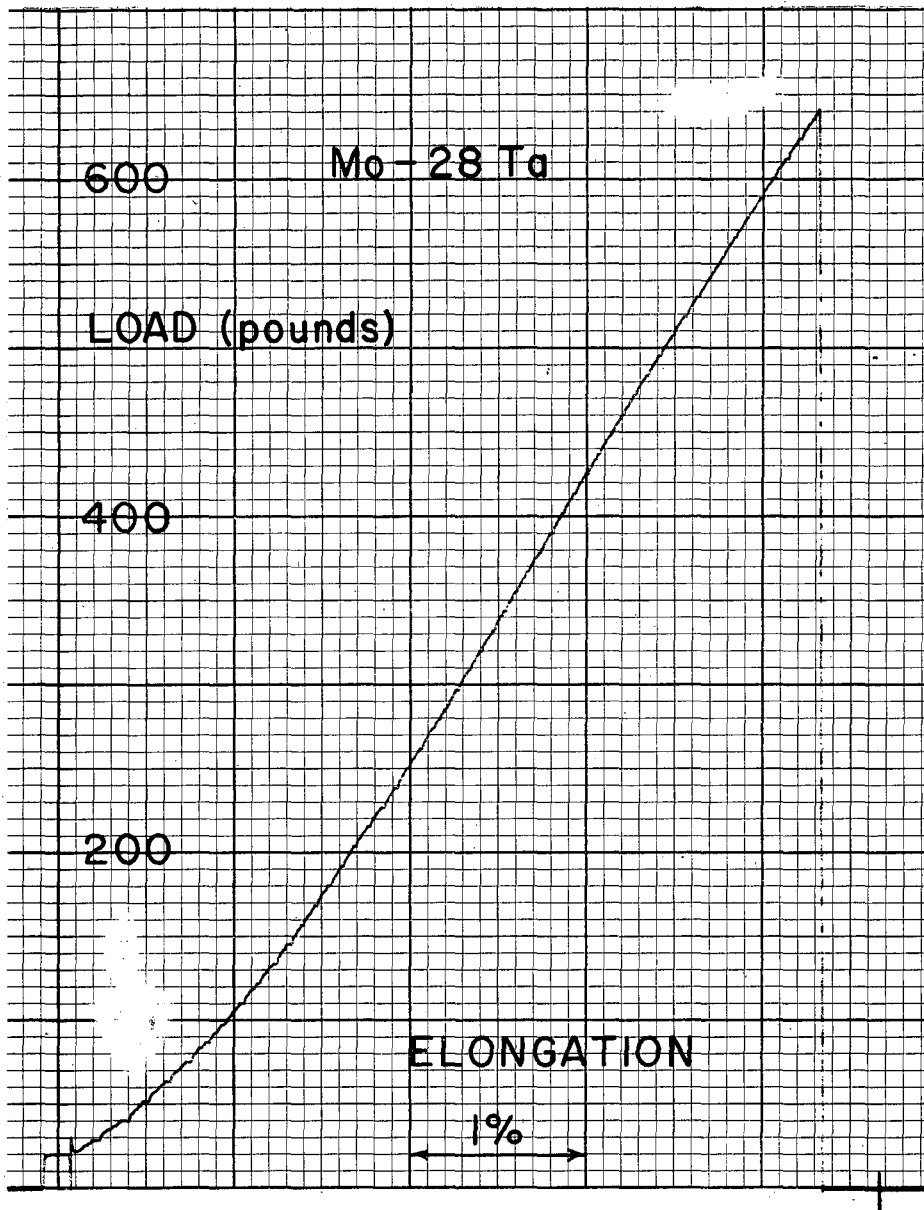
MUB-4431

MUB-4434

Fig. 11.

in the tensile curve of Fig. 11 are attributed to the occurrence of slip which produces the observed slip lines.

The load versus elongation for those alloys which flow plastically together with the orientation of the tensile axis are shown in Fig. 12. The load versus elongation is plotted rather than the true stress-true strain because the deformation along the gauge length was heterogeneous. The expressions used to calculate the true stress-true strain assumes that the area normal to the load along the gauge length and the gauge length itself change uniformly during plastic flow. This was clearly not the case for these crystals. Therefore the tensile curves plotted in the figure were taken directly from the Instron tensile machine.

With the exception of Mo-7 Ta the crystals necked down rapidly and the cross section of the necked region was non-circular, indicating that at least two slip systems were operating after the initial plastic flow. However, only the Mo crystal shows a marked degree of work hardening.

II-D-2. Determination of the Cleavage Plane

A Laue back reflection technique was devised to determine the cleavage plane. A sketch of the arrangement is shown in Fig. 13. A pin hole fixture was constructed so that there were two pinholes 0.025 in. in diameter separated by the length of the pinhole fixture. By inserting a straight 0.020 in tungsten rod into both pinholes the direction of the incident X-ray beam is closely approximated. With the tungsten rod inserted in the pinholes, the crystal is visually adjusted to the position where the rod has normal incidence to the cleavage plane. The crystal was held in position by Plasticene. In
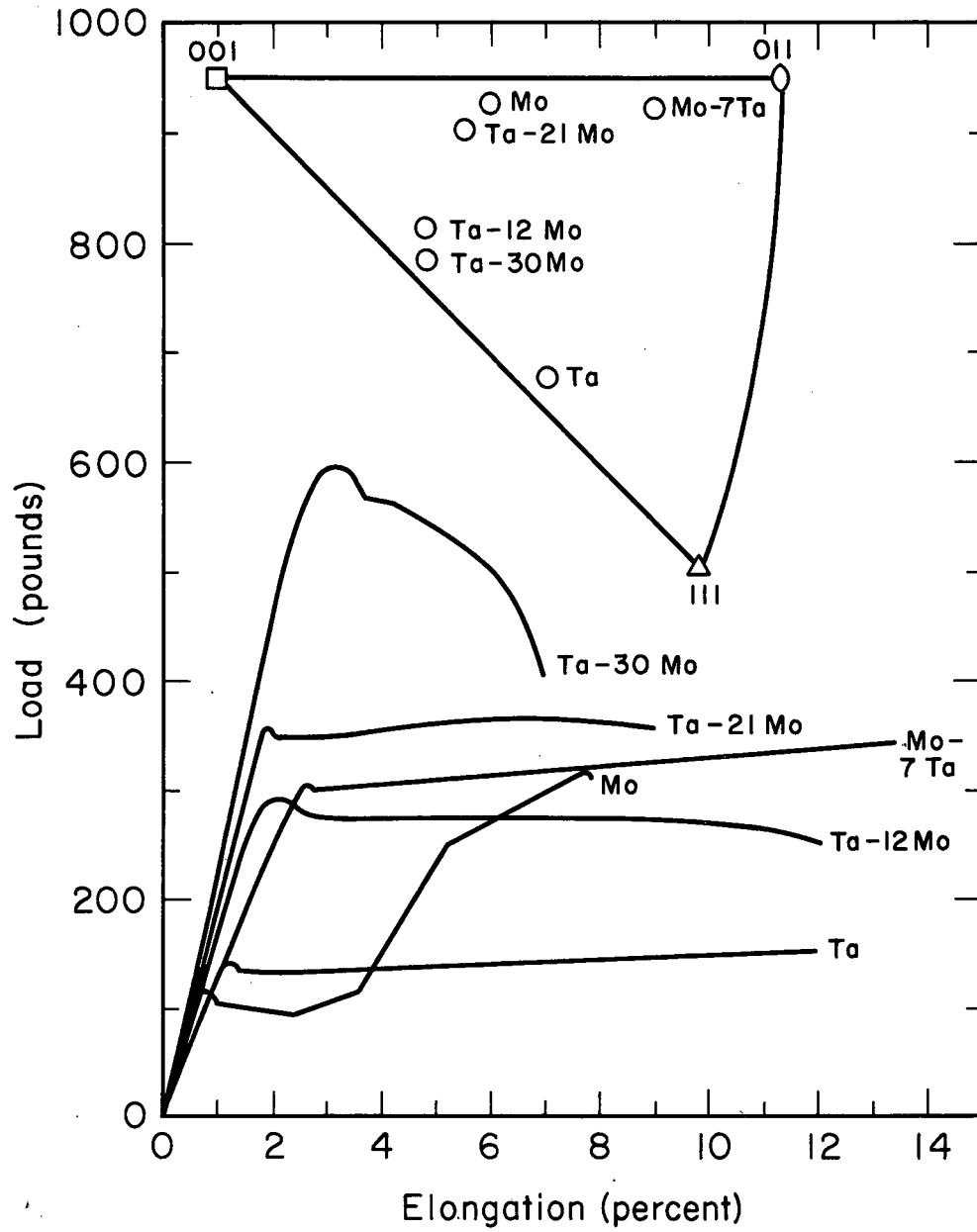
Fig. 12.

MUB-4455

Laue Arrangement for Determination of Cleavage Plane

Laue film frame

Film frame
fixture

0.020 in tungsten rod

Cleavage plane set normal to tungsten rod

X-ray beam

Crystal

Double pin
hole

3 cm

Camera track
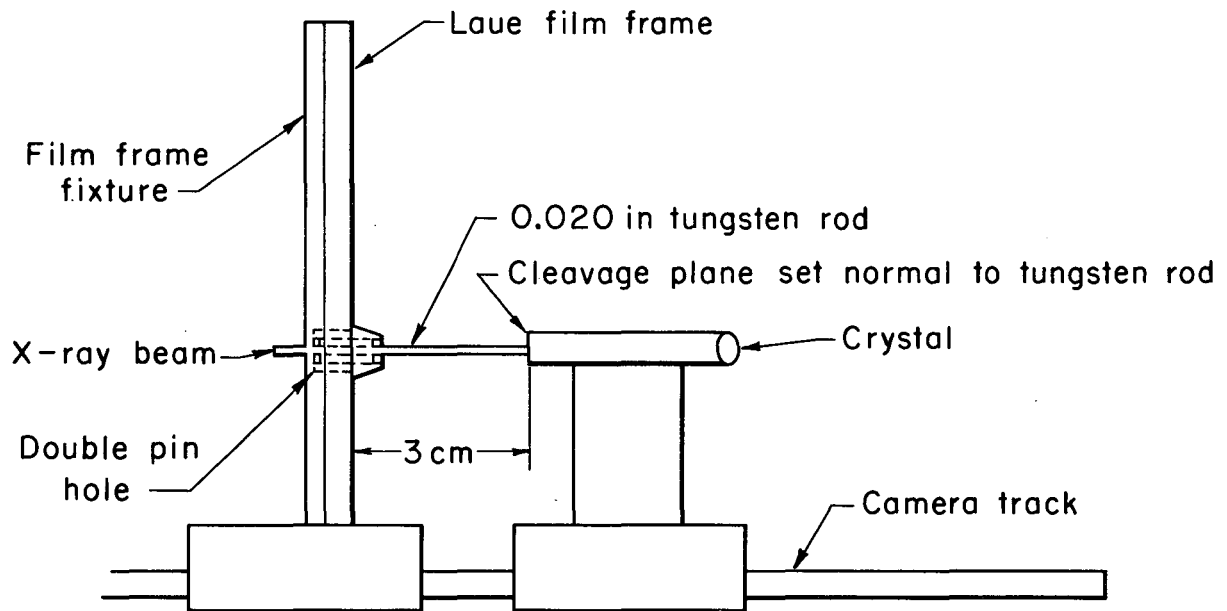
MUB-4446

Fig. 13.

every case a {100} pole was within ten degrees of the center of the
Laue pattern. Therefore, the cleavage plane was considered to be {100}.

II-D-3. Resolution of the Shear Stress

For those crystals that flow plastically the tensile stress was
computed from the load at the lower yield point. For those crystals
which cleave the tensile stress was computed from the maximum load
attained.

The active slip systems at 273°K in Ta and Mo are known to be
{110} <111>. Therefore, the active slip systems in the alloys that
flowed plastically were also assumed to be {110} <111>. This is a
plausible assumption since all the alloys which flow are bcc and are
nonionic solids. The computation of the critical resolved shear
stress for slip was carried out using the formula derived by Barrett.[7]
In this context, critical resolved shear stress is taken to correspond
to the shear stress on the most favorably oriented, with respect to
the tensile axis, (110) plane in a [111] direction contained in that
plane which produces appreciable plastic flow at the given setting of
tensile machine parameters. The most favorably oriented slip system
was determined by angular measurements from the tensile axis which was
plotted on a stereographic projection.

In the classical treatments of cleavage of crystals, the stress
normal to the cleavage plane is considered to be the important stress
parameter. However, these treatments have their shortcomings when
applied to iron and tungsten.[8] In this investigation both the stress
normal to the cleavage plane and the maximum shear stress on the
cleavage plane were computed. No correlations could be made with the

stress normal to the cleavage plane.

II-D-4. Shear Stress

The critical shear stress for flow or cleavage versus alloy composition is shown in Fig. 14. As shown by the figure, Ta alloys containing up to 30 atomic per cent Mo flow plastically at 273°K and Mo alloys containing up to 7 atomic per cent Ta also behave in a similar manner at this temperature. Furthermore, alloys of intermediate composition fail by cleavage. The features of this graph will be treated in detail in the Discussion of Results.

II-E. Lattice Parameter Measurements

The lattice parameters of all the alloys of this investigation were measured for two main reasons, the first being to verify whether Ta-Mo alloy series is complete bcc solid solution from indexing the X-ray spectra and secondly to determine any crystallographic changes which would be suggested by inflections or plateaus in a graph of lattice parameter versus alloy composition.

An x-ray diffractometer was employed to measure the lattice parameter for the following reason. The alloy powders were prepared by filing with a OO file, and thus the powders were in a cold worked condition. Both the elements Ta and Mo have a large affinity for oxygen, nitrogen and hydrogen. Therefore, if the powders were encapsulated in quartz and annealed, the powders would become contaminated by these gases which are absorbed on the surface of the powders and the quartz. Since the surface to volume ratio of a particle increases as the size of the particle decreases it was estimated that as much as two

Table II Shear Stress for Flow or Cleavage

Alloy	Slip on {011}⟨111⟩, Kg/mm^2	
Mo	3.63	
Mo-7 Ta	5.44	
Ta	5.10	
Ta-12 Mo	13.3	
Ta-21 Mo	14.2	
Ta-30 Mo	26.8	
	Cleavage on {100}, Kg/mm^2	τ on {011}⟨111⟩
Mo-19 Ta	11.0	7.70
Mo-28 Ta	5.06	27.1
Mo-40 Ta	7.76	6.60
Ta-50 Mo	8.90	2.60
Ta-42 Mo	11.4	3.58
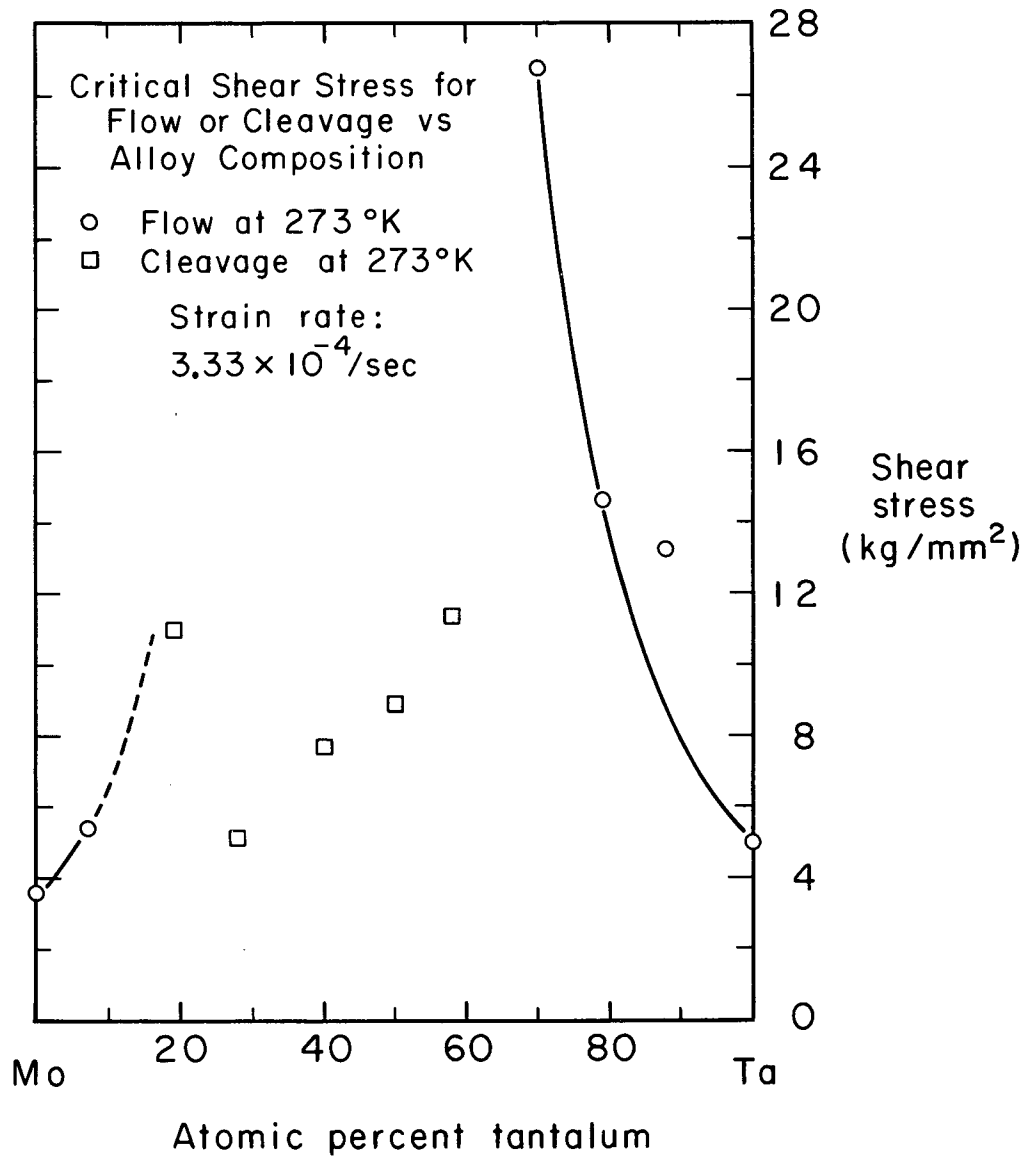
Fig. 14.

MUB-4447

atomic percent interstitials could be dissolved by the powders. The

dissolution of interstitials to this extent would have a measurable

effect on the lattice parameters of the alloys. Therefore, the lattice

parameters were measured from alloy powders in the as filed condition.

An x-ray diffractometer was employed to measure the lattice parameters

because the position of a broad diffraction spectral line can be

measured more accurately from diffractometer spectra than from films

obtained from the traditional powder cameras.

II-E-1. Powder Preparation

The powders were taken from the region of the crystal adjacent to

the cut made by the removal of a crystal section for the resistivity and

tensile measurements. The powder which passed a 200 mesh screen was

mounted by lacquer on a glass disc as shown in Fig. 15. This glass

disc was cemented to an aluminum disc which mounts on the specimen

spinner of the diffractometer. The specimen spinner is constructed in

such a way that the surface of the powder specimen is centered on and

tangent to the diffractometer axis. The glass disc prohibits a con-

tribution to the x-ray spectra from aluminum lines and the rotation of

the powder makes the powder particles appear more randomly oriented to

the incident x-ray beam.

II-E-2. Diffractometer Alignment

Prior to every lattice parameter measurement the diffractometer

was aligned and leveled. The scribed gauge blocks were inserted and

the diffractometer set to these, then the x-ray tube was replaced and

fine adjustments of the beam were made at two theta equal to 0.00 by

observation of the rate meter maximum reading. Diffractometer align-
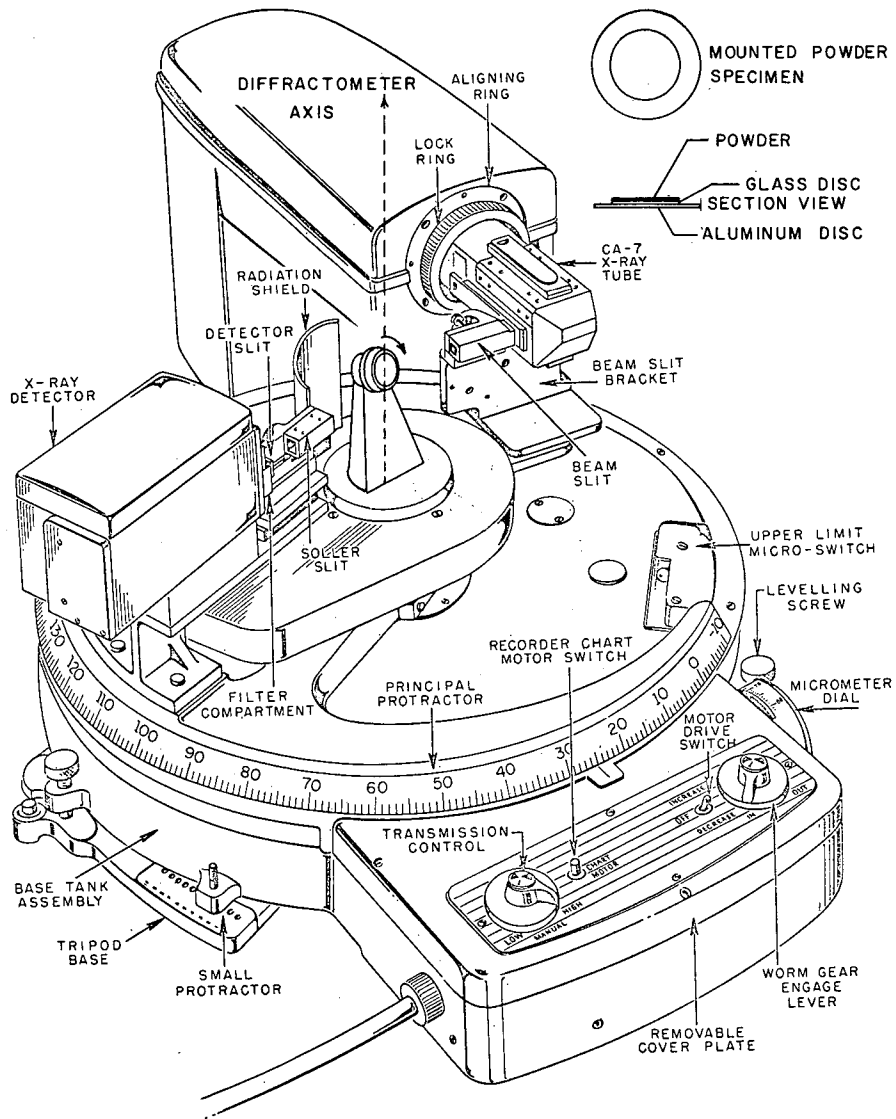
ARRANGEMENT FOR LATTICE PARAMETER
MEASUREMENTS

MUB-4436

Fig. 15.

ment is always requisite for precision lattice parameter measurements with this instrument.

The following pertinent diffractometer parameter settings were employed for taking the x-ray spectra for the purposes of indexing:

Copper tube operated at 34 KV-23 ma 1° beam slit X MR Soller slit X 1° Detector Slit and a nickel filter for K beta, counter time constant of two seconds, two theta scanning speed of two degrees per minute.

For the purpose of determining the position of the spectral lines the following changes in diffractometer parameters were made:

detector slit equal to 0.02°.

counter time constant equal to 0.5 sec.

two theta scanning speed of 0.2° per minute.

II-E-3. Lattice Parameter Results

The position of the x-ray diffracted line was determined as shown in Fig. 16. It is obvious from the figure that copper K alpha one and alpha two are unresolved, therefore the wavelength used in computation of the lattice parameters was the weighted average of these wavelengths, the weighted average being taken in the accepted manner.

The x-ray spectra of every alloy indexed as body centered cubic as previously reported.[1] No anomalous or superstructure diffraction effects were observed.

The lattice parameter computed from each spectral line measured for a given alloy was plotted against sin squared of theta. A line was drawn through these points giving progressively increased weight to the higher theta values and extrapolated to sin squared of theta equal to one.
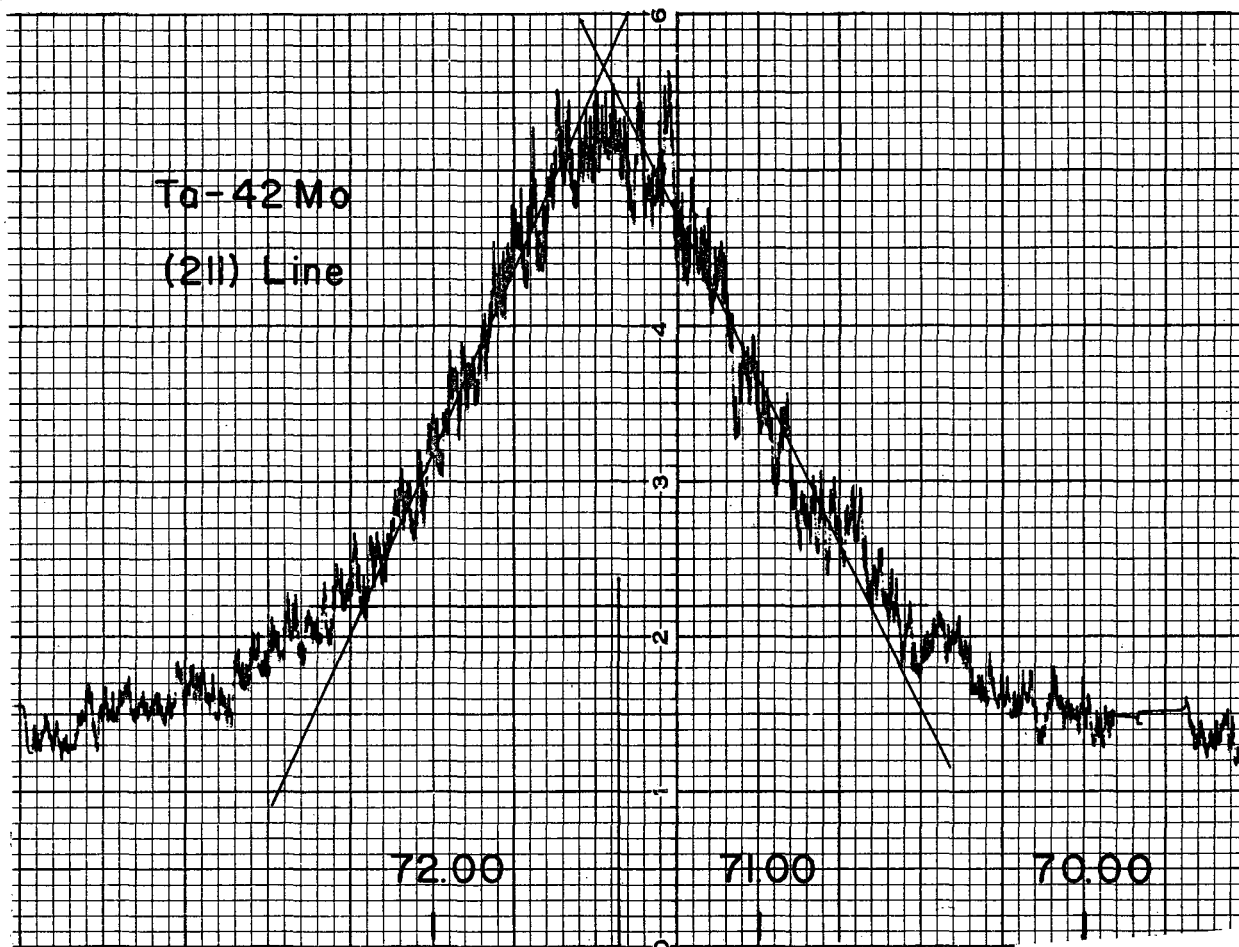
Fig. 16.

MUB-4433

A comparison between the lattice parameter of Mo measured in this investigation and the value reported in the A.S.T.M. x-ray Card Index showed that the value obtained in this investigation agrees within experimental error.

The measured lattice parameters are shown in Table III, and plotted versus the alloy composition in Fig. 17. The line connecting the end points of the binary alloy is the locus of all lattice parameters of an ideal random solid solution, i.e. Vegard's Law. It is evident from the figure that this alloy series shows a positive deviation from Vegard's Law with the sole exception of Mo-7 Ta. Such behavior suggests that the atomic "size" of one or both of the constituent elements changes upon the formation of the solid solution. Further details will be given in the Discussion of Results.

II-F. Transmission Electron Microscopy

The dynamics of dislocations plays a major role in the mechanical behavior of crystals. The interaction of dislocations with imperfections in crystals can be studied in detail by the employment of transmission electron microscopy methods of investigation. In addition, other crystallographic imperfections and features can be investigated in detail from their influence within the reciprocal lattice. Since the wave length of 100 KV electrons is very short and thus the radius of the Ewald reflecting sphere becomes large, plane sections of the reciprocal space of the crystal, to several orders of reflection, are imaged in the selected area electron diffraction pattern. Therefore, transmission electron microscopy has become a very useful tool for

Table III Lattice Parameters (Angstroms)

Alloy	a_o
Mo	3.1468
Mo-7 Ta	3.1540
Mo-19 Ta	3.1793
Mo-28 Ta	3.2065
Mo-40 Ta	3.2275
Ta-50 Mo	2.2355
Ta-42 Mo	3.2488
Ta-30 Mo	3.2710
Ta-21 Mo	3.2830
Ta-12 Mo	3.2952
Ta	3.3040
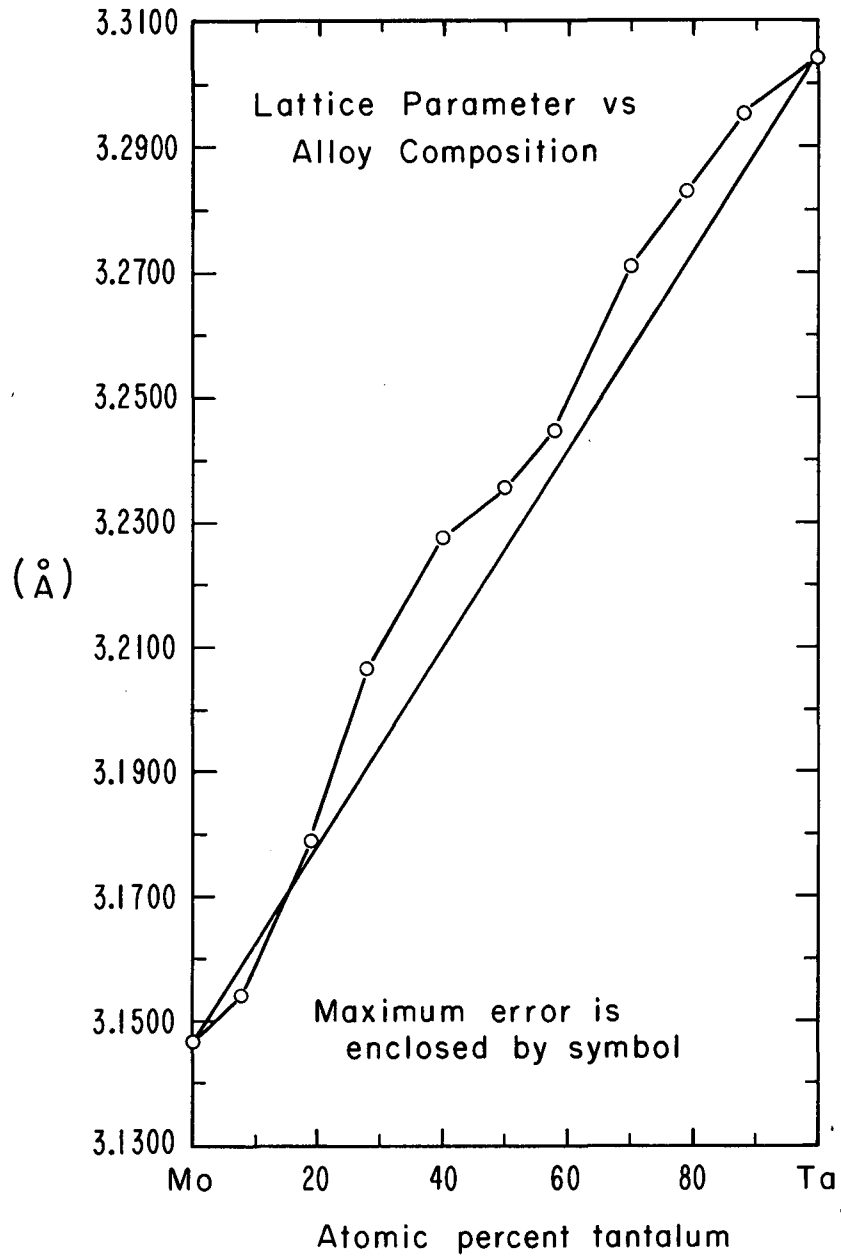
Fig. 17.

MUB-4448

investigation of crystal imperfections. Transmission specimens of the crystals which were measured in the resistivity and tensile series of experiments were prepared and thoroughly examined in the electron microscope.

II-F-1. Sectioning of the Single Crystal Specimens

A spark discharge machine using a moving 0.020 in. dia. copper wire as the cathode was used to cut circular discs from the reduced sections of the crystals. The energy of the spark discharge was maintained at a minimum in order to promote a smooth as possible surface at the cut. The diameter of the reduced section of the crystals was chosen to be the same as the diameter of a Siemens electron microscope grid because electron microscopy was planned to be an integral part of this investigation. The geometry of the discs as cut was about 0.060 in. thick and 0.090 in. in diameter. In order to have a liquid tight junction between the disc and the teflon micro-electropolish specimen holder, about 0.007 in. was removed from each face of the disc by hand sanding on number 400 SiC paper. The temperature of the specimen remained near room temperature.

II-F-2. Micro-Electropolishing

It was necessary to develop a method of electropolishing the discs described above to a thickness in the center of the disc of less than 2000 angstroms. This was accomplished through the use of the micro-electropolishing arrangement shown in Fig. 18. The disc of crystal is secured in the teflon holder such that the disc is concentric with the hole in the upper and lower halves and makes a liquid tight junction with both halves when the three bolts are tightened. A platinum conductor

Micro—Electropolish Arrangement

Binocular
30× microscope

Collimated light source

Bolt holes

Upper specimen holder

Specimen

Pt conductor strip

d.c. pos.

Teflon specimen holder

Lower specimen holder

Specimen

Stainless steel tube (0.100 in. I.D.)

Section of lower specimen holder

d.c. neg.

Lower electrolyte reservoir

Upper electrolyte reservoir
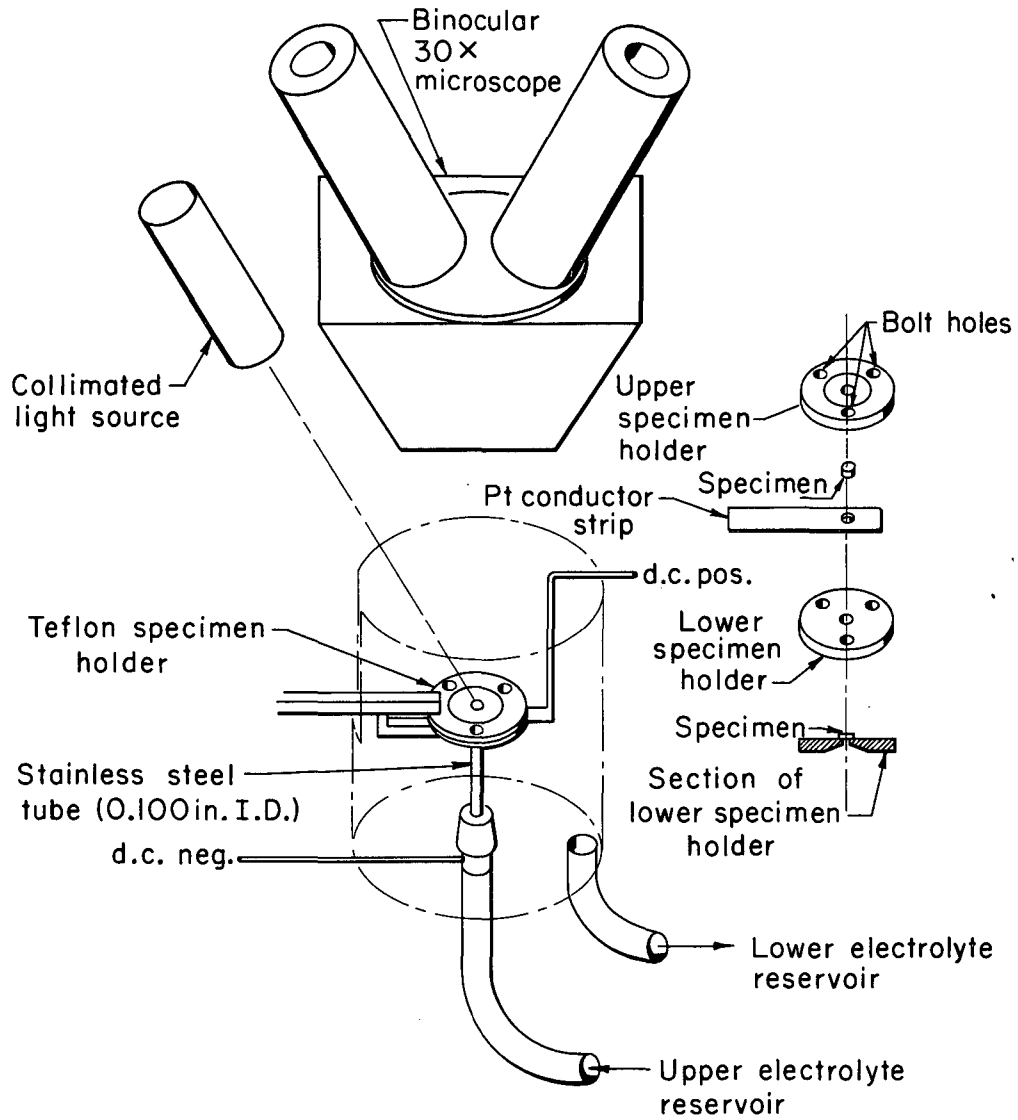
MUB-4449

Fig. 18.

strip containing a hole of diameter greater than the diameter of the

disc makes contact with the side of the disc and serves as the

electrical connection. The assembled holder is then concentrically

placed upon the stainless steel tube and electrical connections are

made as shown in the figure. The electrolyte used for this alloy series

is composed of 90% conc. sulfuric acid plus 10% conc. hydrofluoric acid.

The hydrofluoric acid concentration is not critical and can vary between

5% to 20% without deleterious effects. The electrolyte flows through a

flexible tube from a reservoir at a position of 18 in. above the

specimen holder. A pinch valve on the incoming electrolyte tube is

adjusted so that the electrolyte flows freely through the stainless

steel tube and wets the adjacent surface of the disc. Electrolyte flow

in excess of this amount is unnecessary and should be avoided. The disc

is then electropolished to a depth of about half the disc thickness at

a current density of approximately 60 amps/in^2. This current density

may seem alarmingly high; however, it is to be recognized that the

freely flowing electrolyte serves a dual purpose in that it is also a

coolant for the specimen. As the crystal is electropolished a "dish-

shaped" depression is developed in the disc. The specimen holder is

then invented and electropolished at the same current density on the

opposite side for the same period of time (about three minutes). The

current density is then lowered to 2 amps/in^2 and the upper surface of

the disc is observed through the 30X binocular microscope. The first

indication of electrolyte appearing on the surface of the specimen is

the signal to break the electrical path and thus stop polishing. This

occurs in about 20 minutes.

If one waits until a hole is visible, most of the thin regions, i.e. the region transparent to 100 KV electrons, in the center of the disc has been polished away. The specimen and holder is then removed from the container and flushed with methyl alcohol. The specimen is removed from the teflon holder and is ready for observation in the electron microscope. Since the disc is the same diameter as the Siemens grid and the disc is thin only in the center, no cooling ring or grid is necessary.

The electropolishing of specimens suitable for transmission electron microscopy is more art than science. Therefore, some comments will be made which may be useful to someone contemplating the application of this technique. The surfaces of the specimens prepared with freshly made electrolyte were contaminated with a residue of dissolution products. Several solutions were used in attempts to remove this residue, e.g. 3% chromic adic, 5% potassium permangate, 10% potassium dichromate, dilute nitric-hydrofluoric solutions, 5% sodium hydroxide, 5% magnesium perchlorate and 10% ammonium hydroxide. The dilute nitric hydrofluoric solutions were partially successful but tended to dissolve the thin regions. Some fair results were obtained with the 10% ammonium hydroxide for the Mo base alloys. Fortunately, after the solution had been used for two days the contaminating residue diminished and finally vanished. This indicates that the presence of metal ions in the electrolyte is necessary.

Because the electrolyte contains hydrofluoric acid precautions must be taken to protect the lenses of the optical microscope. The attachment of a sacrificial square of clear glass to the bottom of the

pod of the microscope, with plastic tape sealing the junction, is recommended. The customary Saran Wrap covering is unsatisfactory since it is dissolved by the sulfuric hydrofluoric acid combination. A final comment would be to have patience and perseverance.

II-F-3. Transmission Electron Microscopy Results

The electron micrographs shown in Fig. 19 (a), (b), and (c) were taken on a Siemens Elmiskop 1b electron microscope operated at 100 KV.

During the hand sanding of the discs described in section II-F-1 a bevel on the discs of about 15° was unavoidable. However, this bevel proved to be beneficial for obtaining different specimen attitutes to tilt about in the specimen holder. By taking advantage of the bevel on the specimen, the equivalence of double tilting was accomplished.

The electron micrographs and associated indexed selected area diffraction patterns of the alloys of this investigation are shown in Figs. 19 (a), (b), and (c). The substructure of Mo is the same as that of Ta, so Mo is not shown in the figure. The micrographs and diffraction patterns shown are representative of the alloys of this investigation. There were no anomalous diffraction effects or other indications of crystallographic structural defects observed during all the tilting experiments. In those alloys that flow plastically, discs were cut from regions near the flowed regions of the crystals in order to observe the dislocation arrangements after slip. These results have an exclusive character in that attempts to explain the physical behavior of this alloy system in terms of:

a. intermediate phases

Ta   Ta-12Mo   Ta-21Mo   Ta-30Mo

ZN-4597

Fig. -19a-

Ta-42Mo   Ta-50Mo   Mo-40Ta   Mo-28Ta

Fig. -19b-

ZN-4598

Mo-19Ta   Mo-7Ta

1�“1̄2̄   12̄1̄   2μ   0̇0̇2̄

0̇1̄1̄   0̇0̇0   0̇0̇0
          0̇11   0̇0̇2   12̄1̄
1̄3̇0
   1̄21   1̄12   12̇1̄
          [311]   [210]
                            24̄2
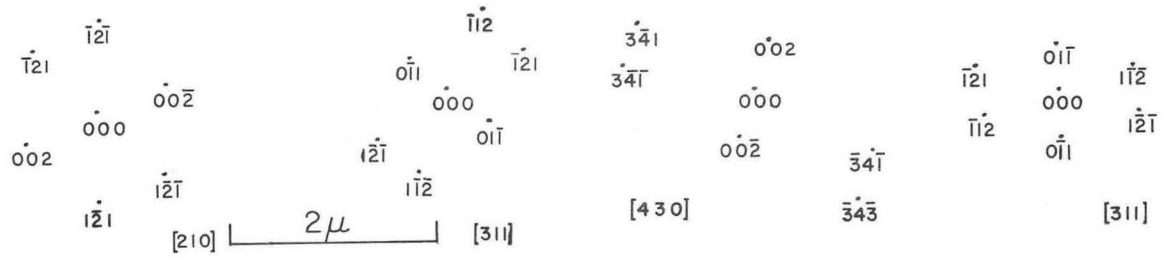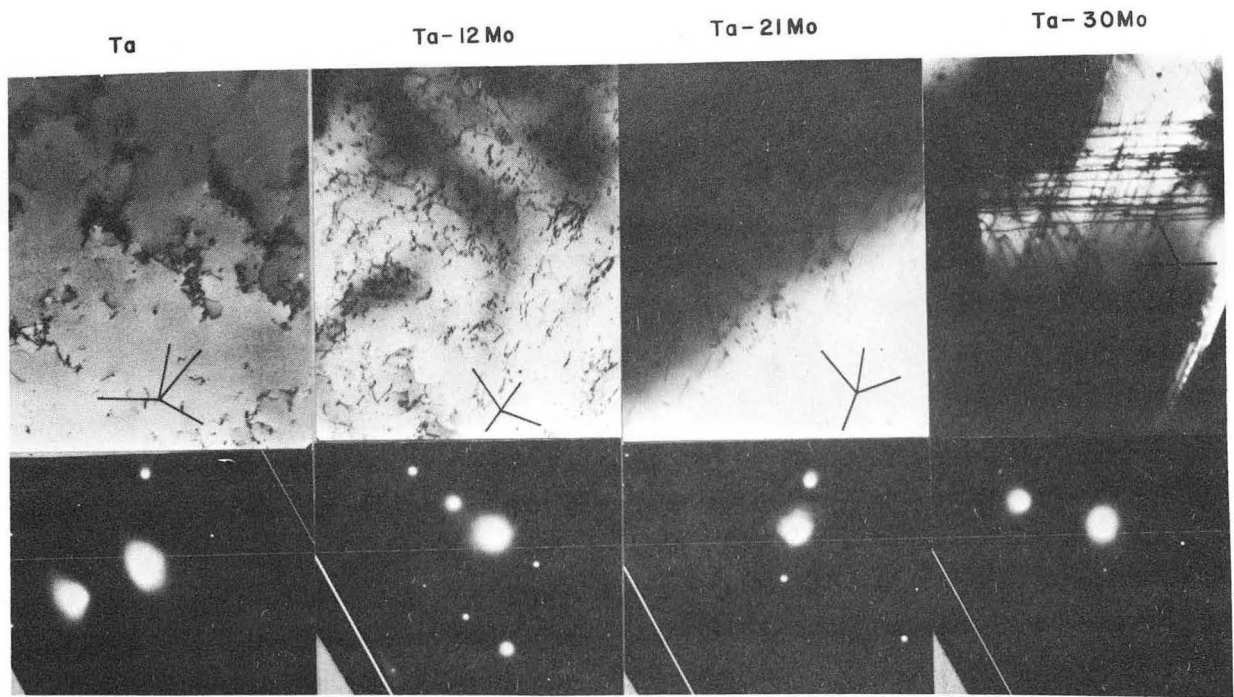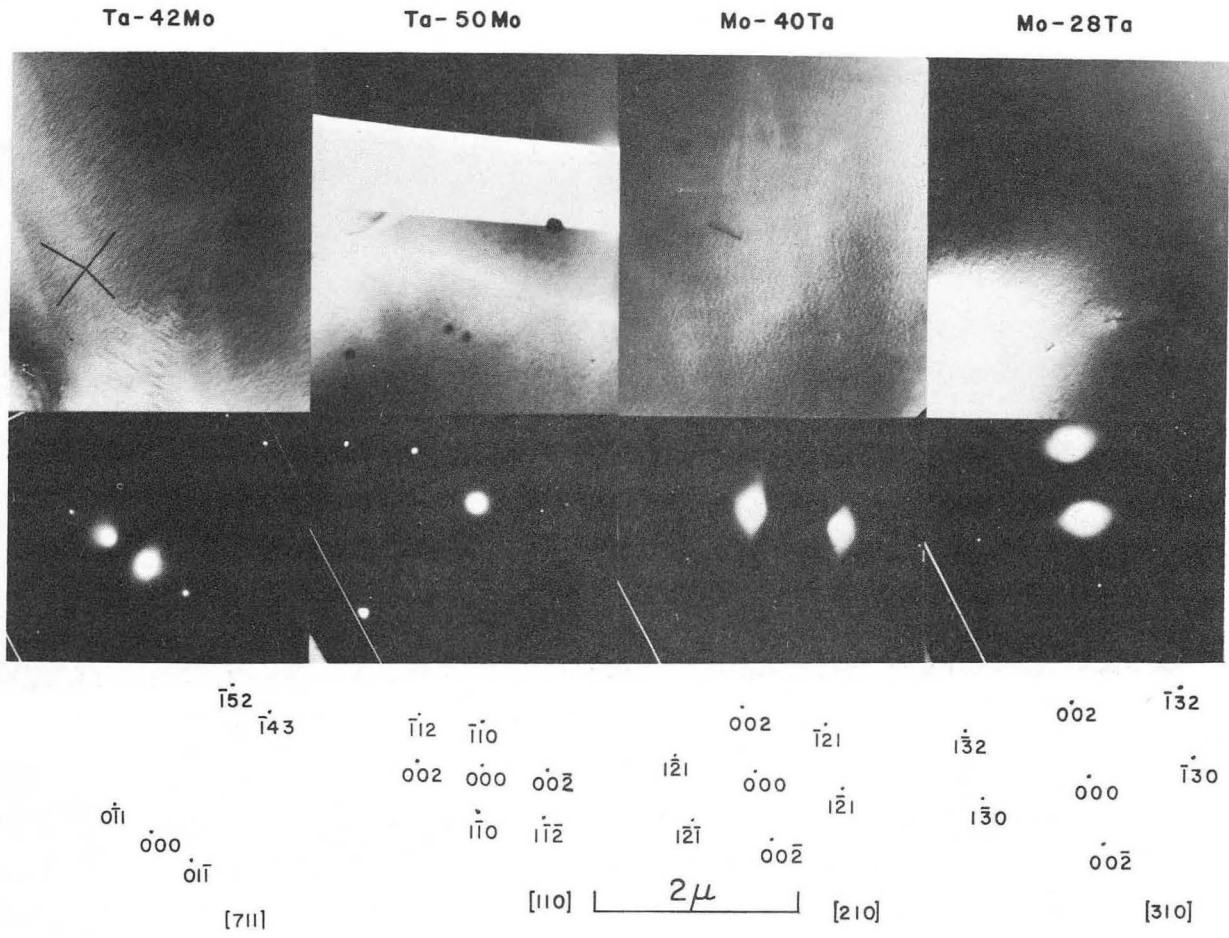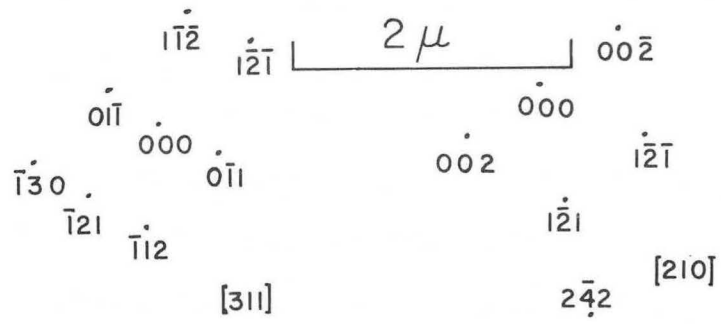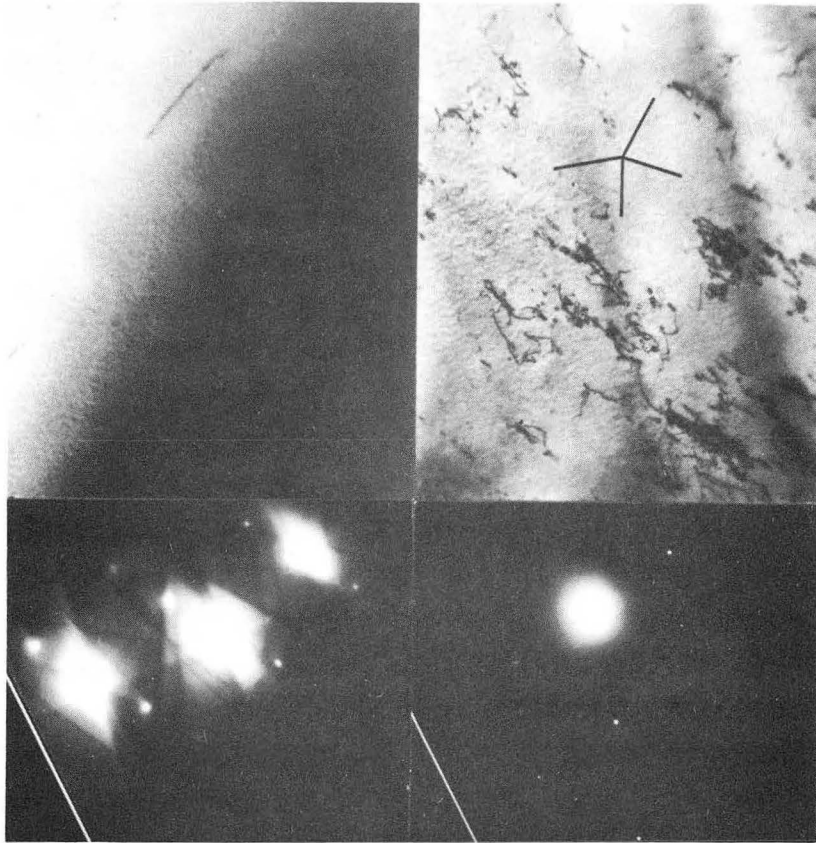
Fig. -19c-

ZN-4599

b. ordering, long range, or short range ordered regions
>300Å, e.g. if the dimension of the short range ordered
region is about three dislocation image widths, i.e.
≈ 300Å, then the dislocations will appear in pairs. This
possibility was investigated and unobserved in all of
these alloys.

c. small scale interstitial precipitates with dimensions >60Å.
are no longer feasible since neither direct nor indirect evidence for
their existence was observed.

In Figs. 19 (a), (b), and (c) the lines drawn on the micrographs
are the projection of the slip vectors $a_o/2 \langle 111 \rangle$ for the given orienta-
tion of the micrograph. Ta, Ta-12 Mo, Ta-21 Mo and Mo-7 Ta show
numerous dipole loops produced by dislocation interactions. The dis-
location debris appears to consist mainly of dipole loops and isolated
dislocation segments of strong screw character as indicated by comparison
to the projections of the slip vectors. The tendency for the disloca-
tions to lie in straight lines becomes prominant in Ta-21 Mo and Ta-30 Mo.
In fact all the dislocations in Ta-30 Mo are straight and are nearly
completely of screw character. This tendency suggests an increase in
the Peierls-Nabarro friction with alloying. The micrographs of those
crystals which flow plastically show that two or more slip systems are
operative sometime after initial flow. Further details will be
presented in the Discussion of Results.

II-G. X-Ray Diffracted Intensity Measurements

During the course of making the lattice parameter measurements it

was observed that the intensity of the (200) line was anomalously large compared to the (110) line in some alloys even after making allowance for the crystal plane multiplicity factor. One possible cause of this behavior would be in a deviation in composition from random solid solution on certain crystallographic planes of the alloy. Such deviations are plausible since the elastic compliances in and normal to cubic crystal planes are anisotropic and the integrated intensity can be affected since the scattering factor of Ta is about twice that of Mo. In order to investigate this possibility a series of definitive x-ray diffraction intensity experiments were planned and executed.

II-G-1. Preparation of Spherical Single Crystals

A spherical single crystal is the most suitable geometric form when quantitative measurements are to be made from two or more sets of atom planes of the crystal.

The method used to obtain nearly spherical single crystals of the alloys of this investigation is shown schematically in Fig. 20. A section of single crystal, taken from the position adjacent to the single crystal section used in the series of measurements already described, is grooved as shown in the figure on a 100 grit wheel. In order to prohibit this mechanically worked region from acting as a source of new crystal nuclei, more than 0.020 in. was removed from the surface by electropolishing. The crystal was then mounted in the lower chuck of the electron beam zone refiner. The energy of the electron beam is gradually increased until the cylindrical region above the groove melts. Surface tension forces require the melt to assume a

Preparation of Single Crystal Spheres

Single crystal →

Grind groove → Electropolish →

Electron beam emitter →

Melt

Cut → Mechanical polish → Electropolish
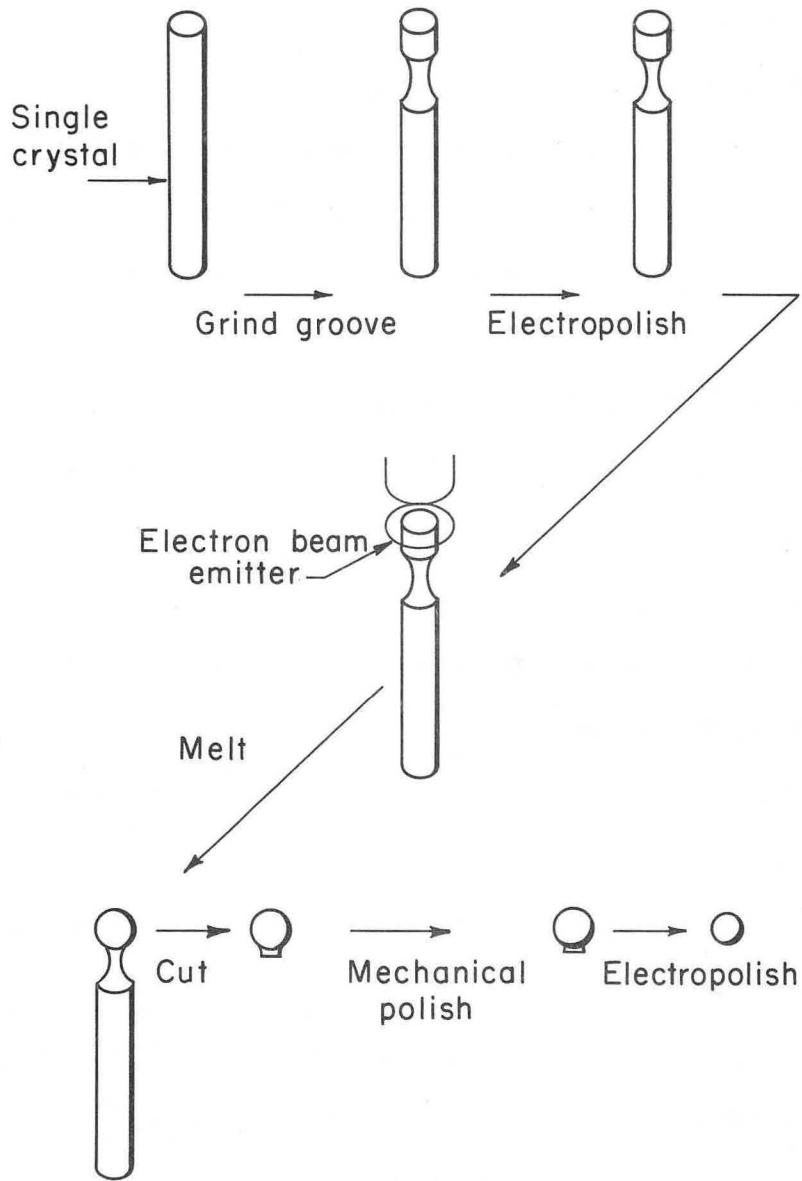
MUB-4450

Fig. 20

spherical shape. The force of gravity distorts this sphere slightly with the final resulting form being an oblate spheroid. As is easily realized this operation requires electron beam power regulation within very narrow limits since the slightest excursion to excess beam power will markedly decrease the surface tension and the molten sphere will then flow down the crystal. The sphere is held molten for about three minutes and then the beam power is gradually decreased until the sphere has solidified. The beam power is slowly decreased to zero to assure that the sphere is in an equilibrium state. The reduced section of the groove is, of course, the single crystal which seeded the molten sphere. The sphere is cut from the single crystal stock with a thin (0.040 in.) 00 file. The "stump" on the sphere is reduced by hand sanding and the damage incurred by this operation is removed by electropolishing.

II-G-2. Setting the Crystal

It was desired to set the crystal such that the [001] is coincident with the diffractometer axis. In this setting the two sets of planes (100), (010) and the two sets (110), ($1\bar{1}0$) and their conjugates can diffract into the detector slit of the counter. In order to make a quantitative comparison between the diffracted intensity of one set of planes with another, the pole [001] must be set to within one half a degree to the diffractometer axis. This requires a complete analysis and correction of all sources of alignment errors.

The details of setting the crystal will now be given. The crystal is placed into a cup machined into a 0.100 in. nylon rod. The nylon rod and crystal are mounted on a three circle goniometer. The three circle goniometer is an integral part of a precision machined single

crystal rotation camera. In the x-ray laboratory the x-ray beams are aligned to be centered with respect to the camera tracks and exactly 4.000 in. above the track. The crystal and the three circle goniometer which is inserted into the rotation camera base is mounted on the camera track. On the same camera track the alignment telescope is then mounted and the center of the spherical single crystal is adjusted to the 4.000 in. height after the goniometers have been set to their zero readings. The rotation camera base with attached crystal and the goniometer is removed from the camera track and then mounted on a camera track that has been constructed to be centered and at ninety degrees to a horizontal camera track. The vertical camera track with attached goniometer and crystal is then mounted on the same horizontal camera track as the alignment telescope. The goniometer is then rotated and the motion of the spherical crystal with respect to the telescope crosshairs is observed. Since the intersection of the telescope crosshairs corresponds to the incident x-ray beam, this intersection must remain on the spherical crystal upon rotation of the goniometer. The crystal is now in a position to intersect an aligned x-ray beam at any setting of the goniometer.

All of the procedure of the above paragraph is to no avail, if the incident x-ray beam is not exactly aligned when the Laue film frame, when film and pinhole are in position for recording the back reflection x-ray photograph. The x-ray beam was aligned previously to the setting of every alloy spherical crystal of this investigation. A Laue film frame, pinhole and film frame fixture were selected, from those available, which were in exact alignment, as determined by the telescope, when

assembled with a film and mounted on the camera track. In order to align the x-ray beam a fluorescent screen which has inscribed cross-hairs and mounts on the camera track is used. The x-ray beam is aligned with this fluorescent screen when the Laue film frame, film, pinhole and film frame fixture are in position to record the back reflection photo-graph. The fluorescent screen fixture is removed and the vertical camera track with attached goniometer and crystal are mounted in position (three centimeters is the film to crystal distance) to record the back reflection photograph. A sketch of the crystal in position to record the Laue back reflection photograph is shown in Fig. 21.

A tungsten target operated at 50 KV. and 20 ma was used as a source of polychromatic x-radiation. A ten minute exposure time was sufficient to resolve many spots on the film.

In the case of the three crystals showing dissolution figures after electropolishing, namely Ta, Mo and Mo-7 Ta, a {001} pole could be set visually to within a thirty degree circle whose center is the incident x-ray beam. For all other crystals the first Laue pattern had to be solved and plotted on a stereographic net in order to determine the angular position of the nearest {001} pole. The shadow of the pinhole fixture on the film was the reference from which the angular position of the zones were measured with a Greninger chart for the stereographic plot.

Because the shadow of the pinhole fixture was used as a reference on the film, it was necessary to verify that the pinhole is located at the center of the pinhole fixture. A traveling microscope was used to measure the centricity of the pinhole with respect to the pinhole fixture.

Arrangement for Setting a Spherical Crystal
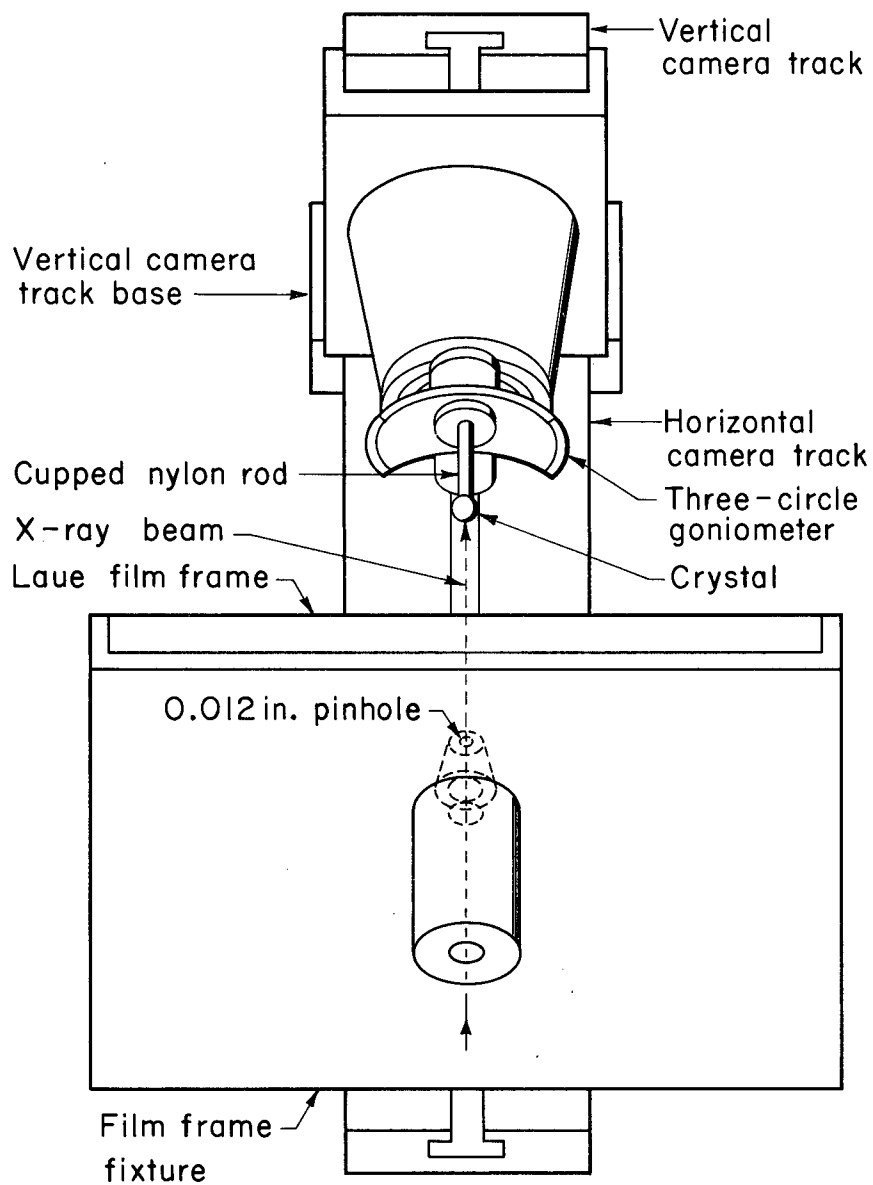
Fig. 21

The diameter of the pinhole (0.012 in.) was found to include the center of the pinhole fixture (diameter 0.565 in.). Therefore, the incident x-ray beam is concentric with the shadow of the pinhole fixture and could be used as a reference.

The stereographic solution of the first Laue photograph determined where the nearest {001} pole was located with respect to the incident beam. If the {001} pole was more than fifteen degrees from the coincidence with the incident beam, the crystal was rotated in the cup of the nylon rod to fulfill this requirement. The settings of the goniometer are adjusted to make the {001} diffraction pattern on the film concentric with the shadow of the pinhole fixture as shown in Fig. 22 (a). This requires the taking of about three more Laue patterns, since the final adjustment of the goniometer requires interpolation between the degree marks.

A {001} pole has now been made coincident with the incident x-ray beam. However, there could exist undiscovered errors in the fixtures and alignments. The maximum error is determined by rotating the goniometer and attached crystal through 180 degrees and taking the Laue pattern of the crystal in this position. The sum of all errors will then show as a deviation of the diffraction pattern from concentricity with the shadow of the pinhole fixture on the film. Figure 22 (b) is the same diffraction pattern as Fig. 22 (a), but the crystal has been rotated by 180 degrees. A distance of one and a half millimeter on the film in the region of the shadow of the pinhole fixture corresponds to one degree. It can be seen that a {001} pole is coincident within
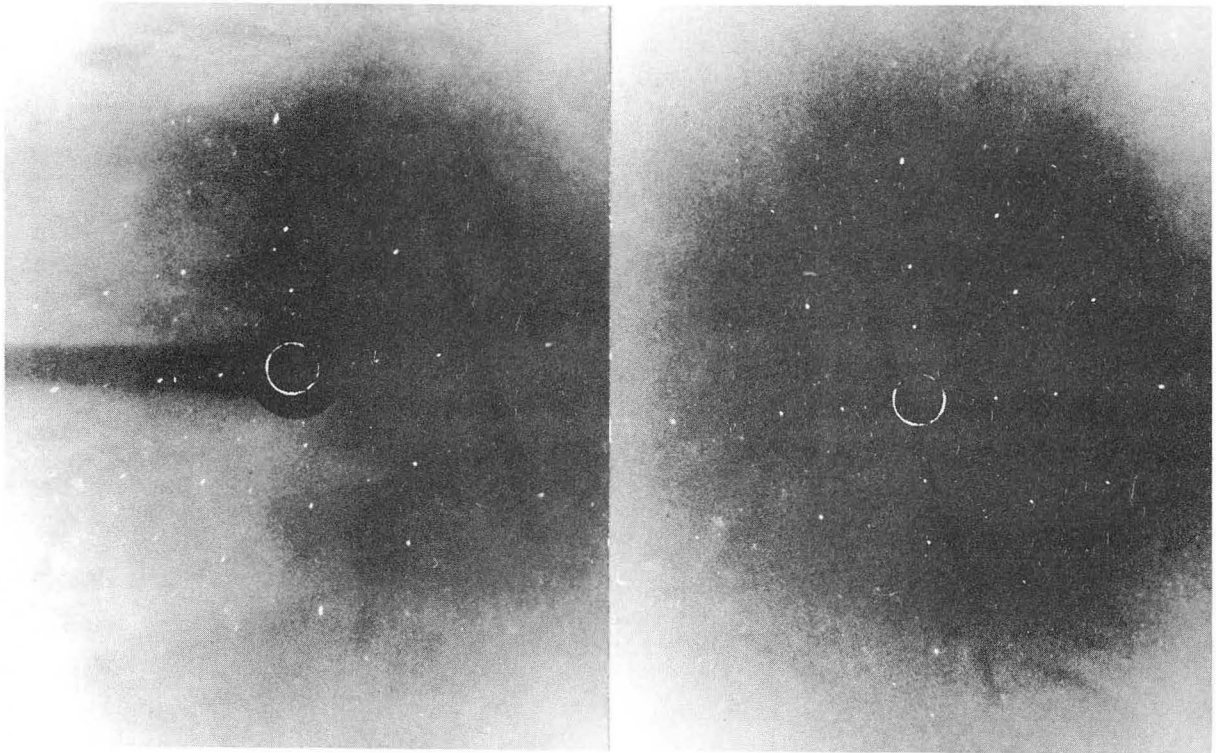
(a)   (b)

ZN-4600

Fig. 22

one-half of a degree to the incident x-ray beam and is thus centered
and normal to the vertical camera track.

II-G-3. Crystal Alignment in the Diffractometer

The goniometer with the crystal set with an {001} pole vertical
is removed from the rotation camera base and inserted in the diffracto-
meter goniometer mount shown in Fig. 23. If the centerline of the
diffractometer goniometer mount is not coincident with the diffractometer
axis, then quite obviously the {001} pole of the set crystal deviates
by the same amount. Therefore, such errors must be detected and
corrected. The detecting of this deviation requires the setting of the
crystal in the exact diffracting position, since the latter is a delicate
operation the method of accomplishing this will now be given in detail.

The procedure for placing the crystal in the exact diffracting
position is as follows. The two theta angular position of the diffrac-
tion line of interest is obtained from the powder data for the given
alloy. If powder data is not available, the line can be found by
searching. The counter is set at this position and the largest detector
slit is inserted. The crystal is then rotated slowly by means of a
wheel which is an integral part of the diffractometer goniometer mount.
This wheel has a groove which accommodates an "O" ring, thus increasing
friction between the operators finger and wheel. The crystal is rotated
until a rate meter deflection is observed. The beam current is decreased
and the angular position of the counter is adjusted for maximum rate
meter deflection. The crystal is then very slowly rotated one way and
then the other seeking the crystal position of maximum rate meter
deflection. Progressively smaller detection slits are inserted at each
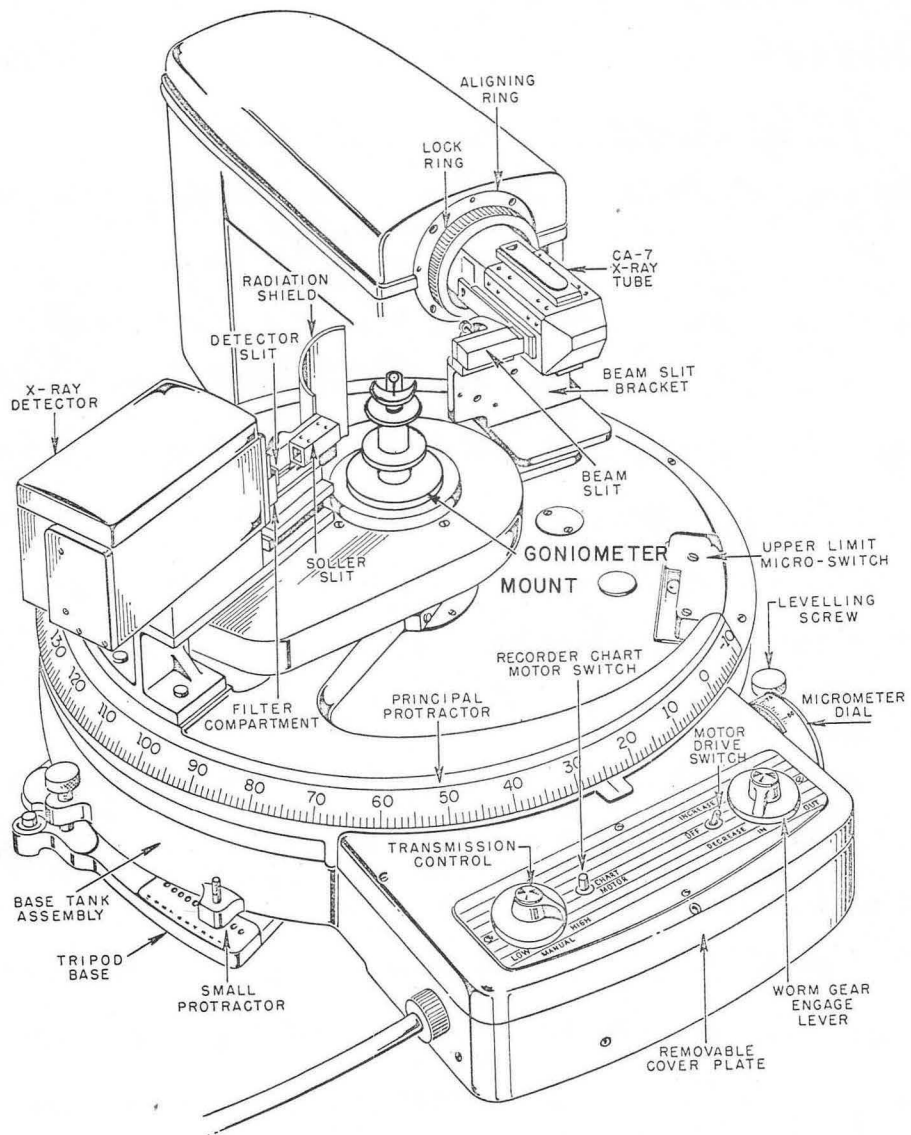
ARRANGEMENT FOR SINGLE CRYSTAL INTENSITY
MEASUREMENTS

MUB-4437

Fig. 23

adjustment of the angular position of the counter and crystal. This
is a procedure of successive approximations. Between two major
parameters, namely the angular position of the counter and angular
position of the crystal with respect to the incident beam. An operator
acquires skill at this procedure quite rapidly and can set the crystal
in exact diffracting position in about ten minutes.

A study was made to determine how reproducibley the author could
set the crystal in diffracting position. The maximum deviation in the
peak intensity of copper K alpha one for the same set of crystal planes
was one percent in ten attempts. This was considered to be satisfactory.

If the [001] of the crystal is coincident with the diffractometer
axis, then the intensity measured for (200, (020), ($\bar{2}$00), and (0$\bar{2}$0)
should be the same and similarly for (220), ($\bar{2}$20), ($\bar{2}\bar{2}$0), and (2$\bar{2}$0).
The previous statement assumes that the crystal is free from low angle
boundaries or if these are present their attitudes are such that they
compensate. In the initial diffractometer goniometer mount constructed,
deviations in the diffracted intensities from the above mentioned groups
of planes were in excess of fifty percent. This alignment error was
corrected in the second mount and maximum deviations of two percent
were measured.

The existence of small angle boundaries presented a problem in rare
instances. When this occurred, the following procedure was carried out.
A (200) and a (020) giving the same (within 2%) intensity are found, i.e.,
sets of {100} 90 degrees from each other. The (220) intensity is measured
and if this value is within two percent of (2$\bar{2}$0), then the intensity from
(220) and (200) were considered acceptable. If the above conditions are

not fulfilled, then another {001} axis must be set on the crystal until the above condition can be fulfilled in the new setting.

II-G-4. <u>Diffractometer Parameter Settings</u>

The following diffractometer parameters were used for the intensity measurements of the (200) and (220) lines:

Copper target operated at 34 KV and 9 ma,

3° beam slit in order to completely bathe the crystal with x-radiation,

MR soller slit and 0.02° detector slit,

Nickel filter for K beta,

Counter scanning speed of 0.02° per 100 sec.,

proportional counter with pulse height selector in with 10 volt window and 5 volt base line,

scale equal to 10,000 c/s,

time constant equal to 0.5 sec.,

the intensity values were automatically printed by a digital printer with 10 sec. intervals between prints, during this interval the counter moved 0.002°.

II-G-5. <u>X-Ray Diffracted Intensity Results</u>

The intensities of the (220) and (200) lines of the alloys of this investigation were integrated from peak two theta minus 0.06° to peak two theta plus 0.06°. This angular range included about 80% of the area under the intensity versus two theta curve. The purpose of these measurements was to compare the diffracted intensities of (200) and (220) from the same crystal, therefore the ratio of the integrated intensity of (200) to the integrated intensity of (220) was computed.

These ratios are given in Table IV and plotted versus alloy composition in Fig. 24. Figure 24 (a) shows the (200) and (220) lines of Mo-40 Ta. The line connecting the end points of a binary system corresponds to the intensity ratios that would be observed in a random solid solution. The figure indicates that in the cleavage range of this alloy series there are large deviations from an ideal random solid solution value of (I_{200}/I_{220}). The interpretation of these results is given in section III.

Table IV Ratio of Integrated X-Ray Diffracted Intensities

Alloy	(I_{200}/I_{220})
Mo	2.06
Mo-7 Ta	1.92
Mo-19 Ta	2.63
Mo-28 Ta	3.02
Mo-40 Ta	3.52
Ta-50 Mo	4.43
Ta-42 Mo	1.59
Ta-30 Mo	2.00
Ta-21 Mo	2.05
Ta-12 Mo	2.33
Ta	2.07

Fig. 24

MUB-4452

(200) LINE
Mo-40Ta

(220) LINE
Mo-40Ta

24 (a)
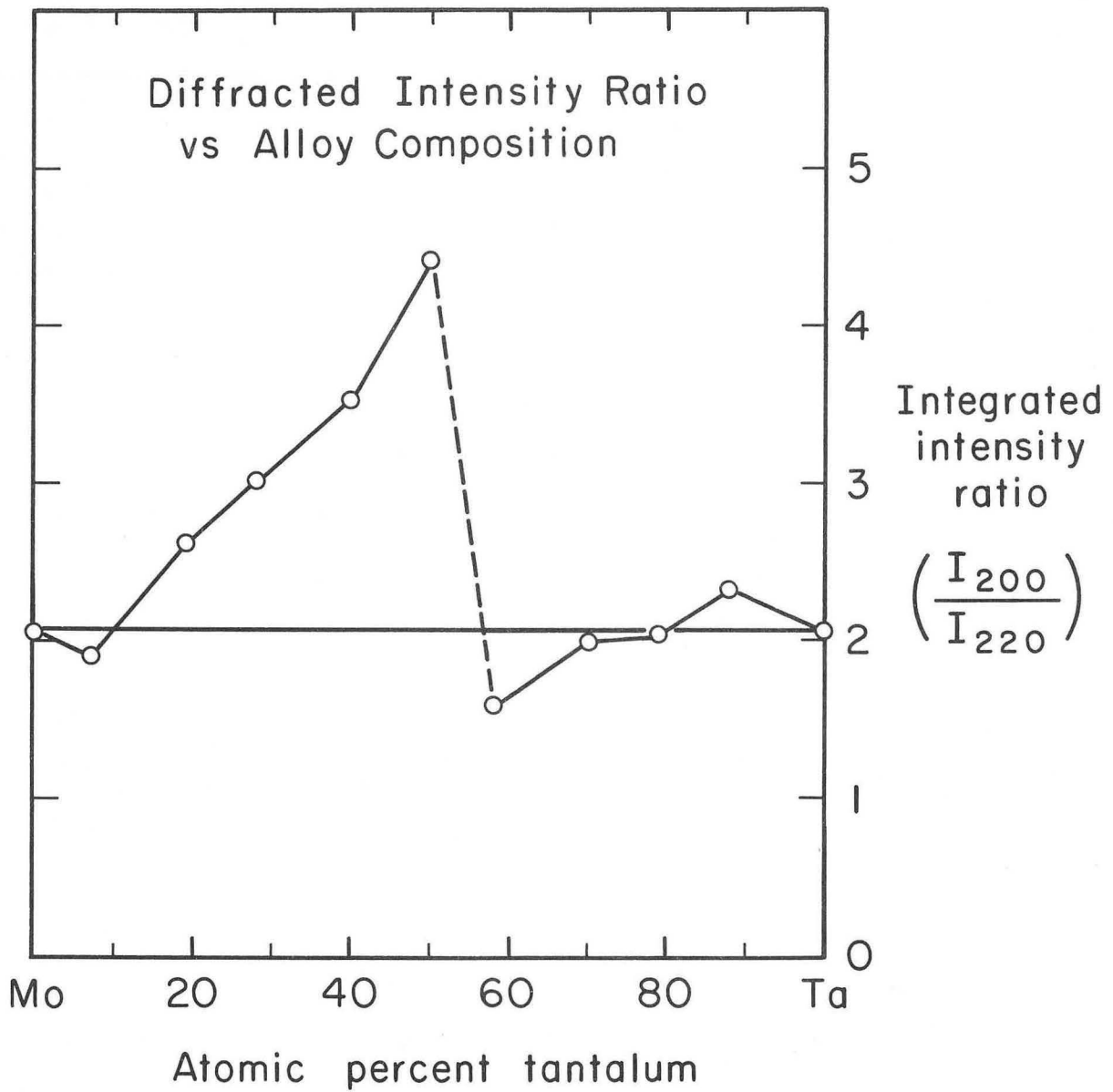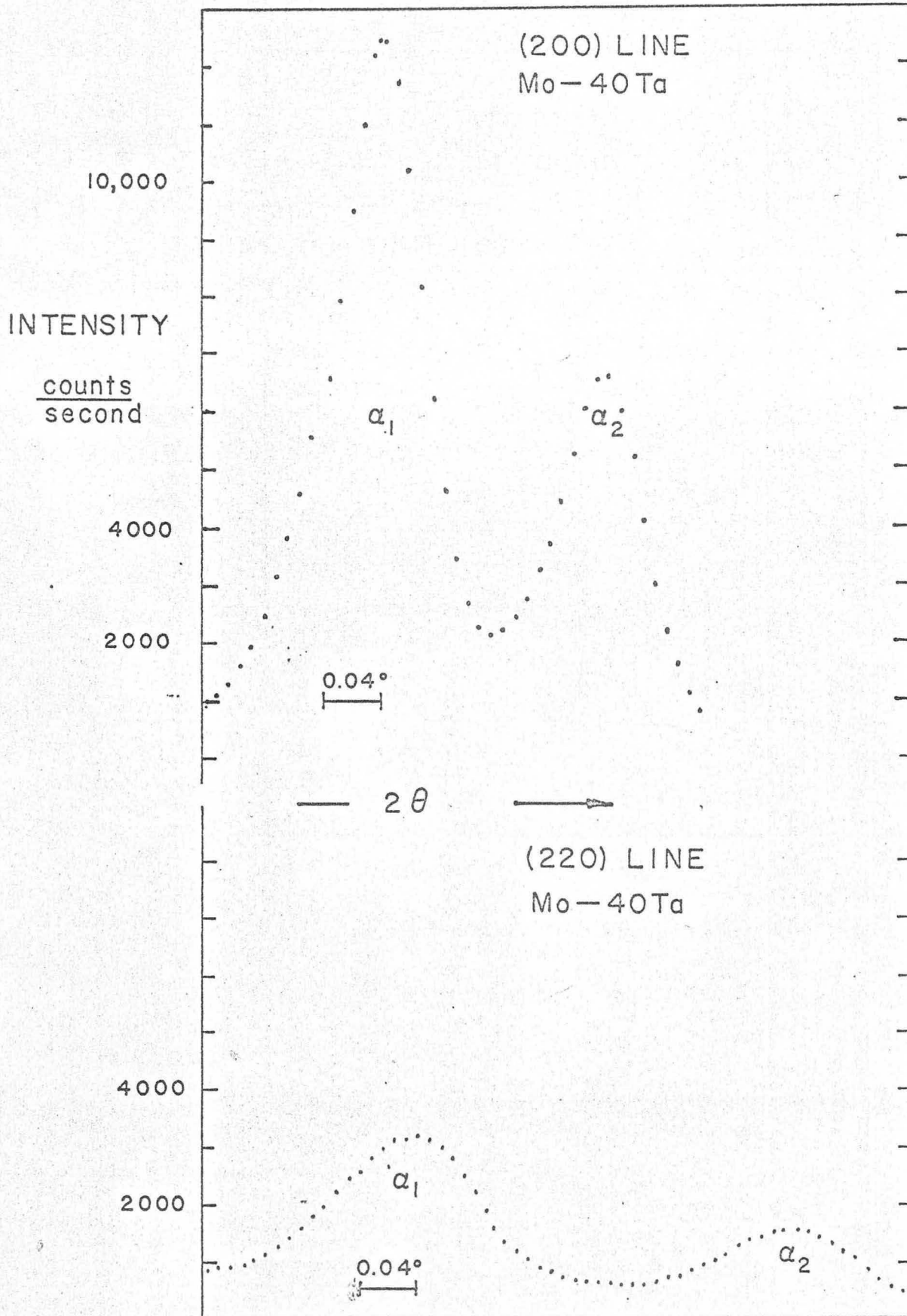
III. DISCUSSION OF RESULTS

The interpretation and significance of the X-ray diffracted intensity results will be discussed first. Then these results will be correlated with the observed transport properties, mechanical properties, lattice parameters and electron microscope observations of the alloys investigated. The reasons for the appearance of cleavage in this alloy system will then be discussed.

III-A. Interpretation of X-Ray Diffracted Intensities

A type of demixing from solid solution distribution of atoms which exhibits a crystallographic habit is believed to exist in the Ta-Mo alloy series. This demixing produces a deviation from the random solid solution distribution of atoms on the {100} planes in some of the alloys and on {110} in others. To gain a further familiarity with the physical disposition of atoms in the crystal, which has deviations on the {100}, consider a region of a Ta-50 Mo alloy crystal where the deviation from random solid solution composition occurs on (100). As one samples the distribution of atoms on (100) proceeding in the [100] direction, one encounters planes where the ratio of Ta atoms to Mo atoms is greater than one to one, say nine to one. In a random solid solution the ratio would be one to one. Since the overall composition of the alloy is Ta-50 Mo it is required that as one proceeds in the [100] direction one encounters (100) planes where the ratio of Ta to Mo is one to nine. Thus one finds (100) planes which are rich in Ta and neighboring (100) planes which are rich in Mo. A schematic illustration of these composition deviations as one proceeds in the [100] direction is given in Fig. 25. It is to be noted that the deviations do not have to be periodic, nor

ATOM RATIO Ta/Mo

distance along —— [100] ——

25
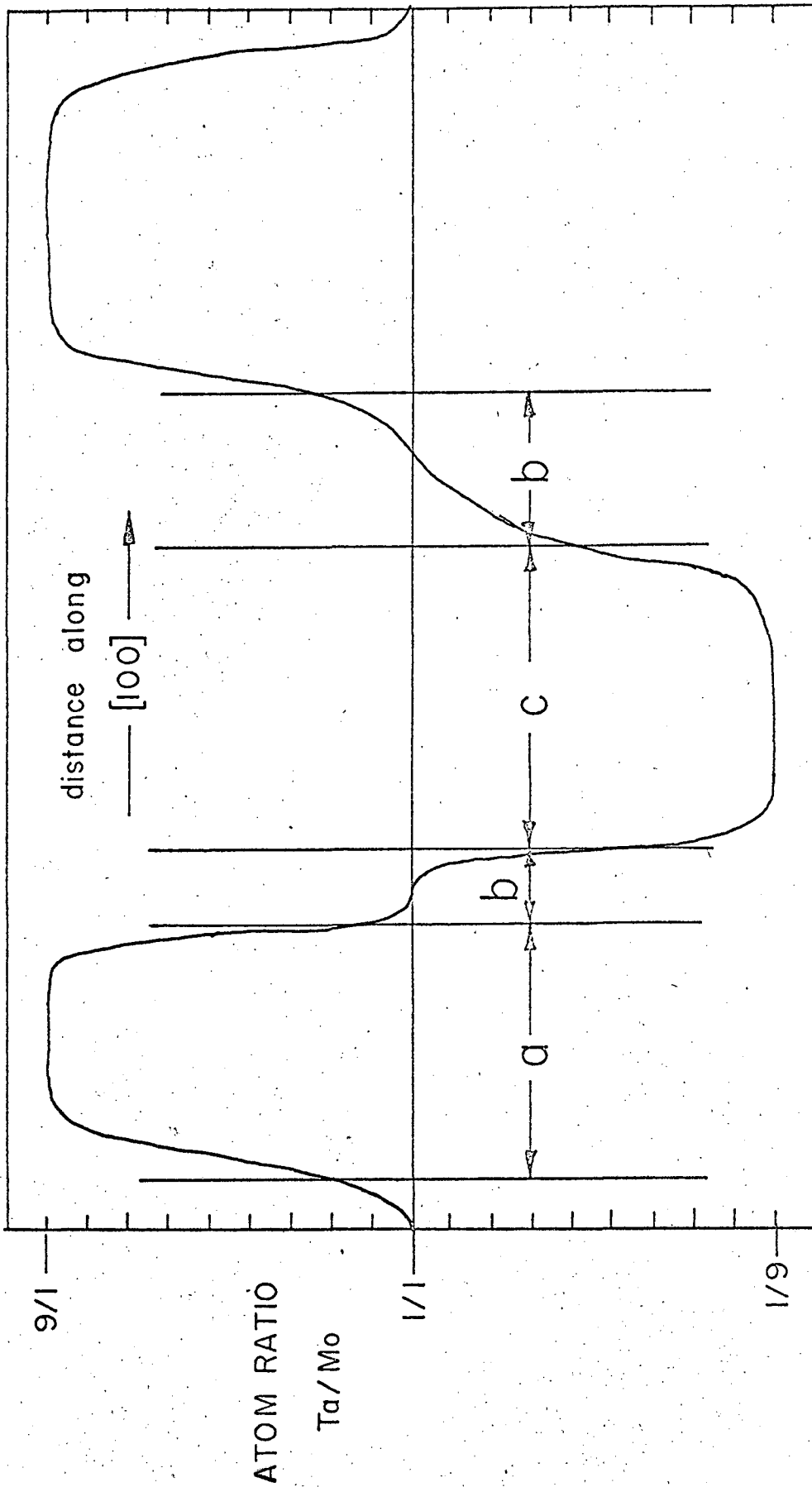
the amplitude of the deviations be a constant. Furthermore <u>no</u> ordering, e.g. identity distance is required. The region "a" is rich in tantalum, region "b" is a transition region between "a" and the molybdenum rich region "c". Because a (100) plane is equivalent to a (010) or (001), when deviations exist in a crystal they must generate quasi cubic domains. One domain will have composition deviations on (100), the adjacent on (010) and the third adjacent domain on (001). When there are composition deviations on {110} then the crystal is divided into six types of domains corresponding to the six equivalent {110} planes. The type of demixing that is thought to occur in this alloy system is to be distinguished from the classical "miscibility gap" reaction in that the deviations in distribution of atoms have a crystallographic habit which is not considered in those systems showing the classical miscibility gap.

Because a tantalum atom is about twice as effective in scattering x-rays as molybdenum, regions rich in Ta and rich in Mo will interact with x-radiation to different degrees. The crystallographic habit of these deviations in atomic distribution is expected to influence the integrated diffracted intensity of the (200) and (220) lines. The following paragraphs are devoted to an analysis of the influence of composition deviations on {100} and {110} on the integrated diffracted intensity of the (200) and (220) lines.

When the smallest dimension of a region rich in Ta or Mo is about a thousand unit cells it becomes necessary to consider these regions as having discrete scattering character for x-rays. This requires the writing of a structure factor for a Ta rich, Mo rich and one to one solid solution region. The expression for the structure factor, F, is:

$$F = \sum_j f_j \ell^{2\Pi i (h\mu_j + k\nu_j + \ell\omega_j)}$$

where f_j is the scattering factor for the jth atom at the coordinates μ, ν, and ω with respect to the origin of the unit cell. h, k and ℓ are the Miller indices for a plane in the crystal structure. The x-ray diffracted intensity is proportional to $|F|^2$, therefore $|F|^2$ is computed for two cases of interest here.

Consider a Ta-50 Mo alloy crystal with the Ta atoms at the origin of the unit cell, i.e. $\mu = 0$, $\nu = 0$, $\omega = 0$, and the Mo atoms at the body centered position, $\mu = \frac{1}{2}$, $\nu = \frac{1}{2}$, and $\omega = \frac{1}{2}$. The powder patterns all indexed as being bcc, therefore the crystal structure of the alloy series is bcc. When Ta is always at the origin of the unit cell and Mo at the body centered position, the crystal is completely ordered. The structure factor is:

$$F_{hk\ell} = f_{Ta} \ell^{2\Pi i(0)} + f_{Mo} \ell^{2\Pi i(\frac{h}{2} + \frac{k}{2} + \frac{\ell}{2})}$$

$$F_{hk\ell} = f_{Ta} + f_{Mo} \ell^{\Pi i(h+k+\ell)}$$

when (h+k+ℓ) is an even integer

$$F_{hk\ell} = f_{Ta} + f_{Mo}$$

and

$$|F_{hk\ell}|^2 = (f_{Ta} + f_{Mo})^2 = f_{Ta}^2 + 2f_{Ta} f_{Mo} + f_{Mo}^2$$

Now when (h+k+ℓ) is an odd integer, $F_{hk\ell}$ becomes

$$F_{hk\ell} = f_{Ta} - f_{Mo}$$

and

$$|F_{hk\ell}|^2 = f_{Ta}^2 - 2f_{Ta}f_{Mo} + f_{Mo}^2 .$$

The above case where Ta and Mo have fixed positions in the crystal shows that diffraction intensity is allowed for all values of h, k and ℓ.

Now consider the case of a Ta-50 Mo alloy crystal which is a random solid solution. In this case neither the Ta nor the Mo atoms occupy fixed positions in the crystal. Either Ta or Mo atoms can be at the position $\mu = 0$, $\nu = 0$, $\omega = 0$ or $\mu = \frac{1}{2}$, $\nu = \frac{1}{2}$, $\omega = \frac{1}{2}$, for any one of the ten thousand or more cells sampled by x-rays. One can allow for this indeterminacy of position of Ta and Mo atoms by considering that the atom at both these positions has an effective scattering factor given by

$$f_x = (x_A f_{Ta} + (1-x_A)f_{Mo})$$

where x_A is the atom fraction of Ta in the alloy or in a region of sufficient dimension which is rich in Ta or Mo. For a random solid solution the value of the structure factor is

$$F_{hk\ell} = f_x \ell^{2\pi i(0)} + f_x \ell^{2\pi i(\frac{h}{2} + \frac{k}{2} + \frac{\ell}{2})}$$

$$= f_x + f_x \ell^{\pi i(h+k+\ell)} .$$

When $(h+k+\ell)$ is an odd integer $F_{hk\ell} = f_x - f_x = 0$. When $(h+k+\ell)$ is an even integer,

$$F_{hk\ell} = 2f_x \qquad \text{and}$$

$|F_{hk\ell}|^2 = 4f_x^2$. Hence, for any random solid solution of Ta-Mo alloys the value of $|F_{hk\ell}|^2$ is $4f_x^2$ and the selection rules for indices are $(h+k+\ell)$ equal to an even integer. However, when the smallest dimension of a Ta rich or Mo rich region is about a thousand lattice constants, the structure

factor must be written for that particular region and the value of x_A for that region must be used in the expression for the effective atom scattering factor.

The integrated diffracted intensity of a nearly perfect crystal is greatly influenced by what is termed primary extinction. Primary extinction results from phase shifts in the x-ray beam produced by scattering from the atoms of the crystal. Each scattering event produces a phase shift of $\Pi/2$, thus two such events shift the wave by Π and produce destructive interference of the x-ray beam. A detailed analysis[9] of this effect shows that the integrated intensity, I, diffracted from a crystal as a function of the number of planes, P, from the surface of the crystal is given by:

$$I = I_o \frac{\tanh(pq)}{pq}$$

where I_o is the incident x-ray intensity, q is the amplitude diffracted from a single plane of atoms when a plane wave of unit amplitude is incident upon it. The value of q is given by:

$$|q| = N \, a \, \lambda \, |F_{hk\ell}| \left(\frac{\ell^2}{mc^2}\right) \, \text{cosec} \, \Theta_{hk\ell}$$

where   N is the number of unit cells with structure factor $|F_{hk\ell}|$ per unit volume of crystal,

     a is the spacing between planes,

     λ is the x-ray wave length,

     ℓ is the electron charge,

     m is the electron mass,

     c is the velocity of light,

     $\Theta_{hk\ell}$ is the diffraction angle.

From the expression for $|q|$ it is seen that $|q|$ depends on the indices of the diffraction line through the values of $|F_{hk\ell}|$ and $\Theta_{hk\ell}$.

When measuring diffracted intensities of crystals composed of atoms of relatively large atomic number using copper K alpha x-ray wavelengths the effect of radiation absorption must be considered. The expression for the value of the intensity after passing through, x, distance of material with linear absorption factor, μ, is given by:

$$I = I_o \exp - \mu x.$$

The geometry of incident and diffracted x-ray beam gives a value of:

$$x = 2d \cot \Theta_{hk\ell}$$

where d is the depth taken normal to the crystal surface. The value of μ for a solid solution of Ta and Mo atoms is given by:

$$\mu = x_A \mu_{Ta} + (1-x_A) \mu_{Mo}.$$

Upon combination of the above expressions, I is given by:

$$I = I_o \exp - \beta d$$

where $\beta = (x_A \mu_{Ta} + (1-x_A)\mu_{Mo})2 \cot \Theta_{hk\ell}$. One notes that the attenuation factor is a function of the atom fraction of Ta and Mo as well as the indices of the diffraction line.

The effect of primary extinction and absorption will limit the depth to which atoms in the crystal can contribute to the diffracted intensity. A knowledge of this extinction depth is essential to the interpretation of the x-ray diffracted intensity ratios of the Ta-Mo alloy series. The values I/I_o as a function of distance from the crystal surface resulting from primary extinction and absorption for three alloy compositions

are shown in Figs. 26 and 27. The composition Mo-10Ta represents a Mo
rich region in a Ta-50 Mo alloy, Ta-10 Mo in a Ta rich region and Ta-50 Mo
represents the solid solution. The extinction distances selected from the
curves were based on the presumption that atoms at a distance below the
crystal surface such that the value of I/I_o is less than $1/\ell$ contribute a
negligible amount to the diffracted intensity. The curves give the
following extinction distances:

(200) line
$\begin{cases} \text{Ta-10 Mo about 2400 Å} \\ \text{Ta-50 Mo about 3100 Å} \\ \text{Mo-10 Ta about 4200 Å} \end{cases}$

(220) line
$\begin{cases} \text{Ta-10 Mo about 4200 Å} \\ \text{Ta-50 Mo about 5600 Å} \\ \text{Mo-10 Ta about 7200 Å} \end{cases}$

An expression for the total integrated diffracted intensity of an $(hk\ell)$
line has been derived in Ref. 9. The total integrated intensity is:

$$I_x \propto N^2 |F|^2 \lambda^3 \left(\frac{\ell^2}{mc^2} \right) \left(\frac{1+\cos^2 2\Theta hk\ell}{2 \sin 2\Theta hk\ell} \right)$$

Note that I_x varies as $|F|^2$ which in turn varies with the alloy composition,
also I_x depends on the indices of the line through $\Theta_{hk\ell}$. The values used
to compute I_x and those used for determining the curves in Figs. 26 and 27
are entered in Table V.

The purpose of the foregoing development is to examine in detail
the integrated intensity ratio $(I_{200}/I_{220})_o$ measured on a complete
random solid solution crystal and on a crystal with composition deviations

distance (Å)

THE EFFECT OF PRIMARY EXTINCTION AND ABSORPTION ON THE (200)
LINE AT THE P'th PLANE FROM THE CRYSTAL SURFACE

A, A' — Mo – 10 Ta
B, B' — Ta – 50 Mo
C, C' — Ta – 10 Mo

$$\frac{I}{I_0} = \frac{TANH(pq)}{pq}$$

$$\frac{I}{I_0} = \frac{TANH(pq)}{pq} \exp{-\beta d}$$

$\frac{I}{I_0}$

$\frac{1}{e}$

A
B
A'
C
B'
C'

26   p (number of planes)

THE EFFECT OF PRIMARY EXTINCTION AND ABSORPTION ON THE (220)
LINE AT THE P'th PLANE FROM THE CRYSTAL SURFACE

A, A' – Mo – 10 Ta
B, B' – Ta – 50 Mo
C, C' – Ta – 10 Mo

$$\frac{I}{I_0} = \frac{TANH\,(pq)}{pq}$$

$$\frac{I}{I_0} = \frac{TANH\,(pq)}{pq}\,exp - \beta\,d$$

distance (Å)

p (number of planes)

27
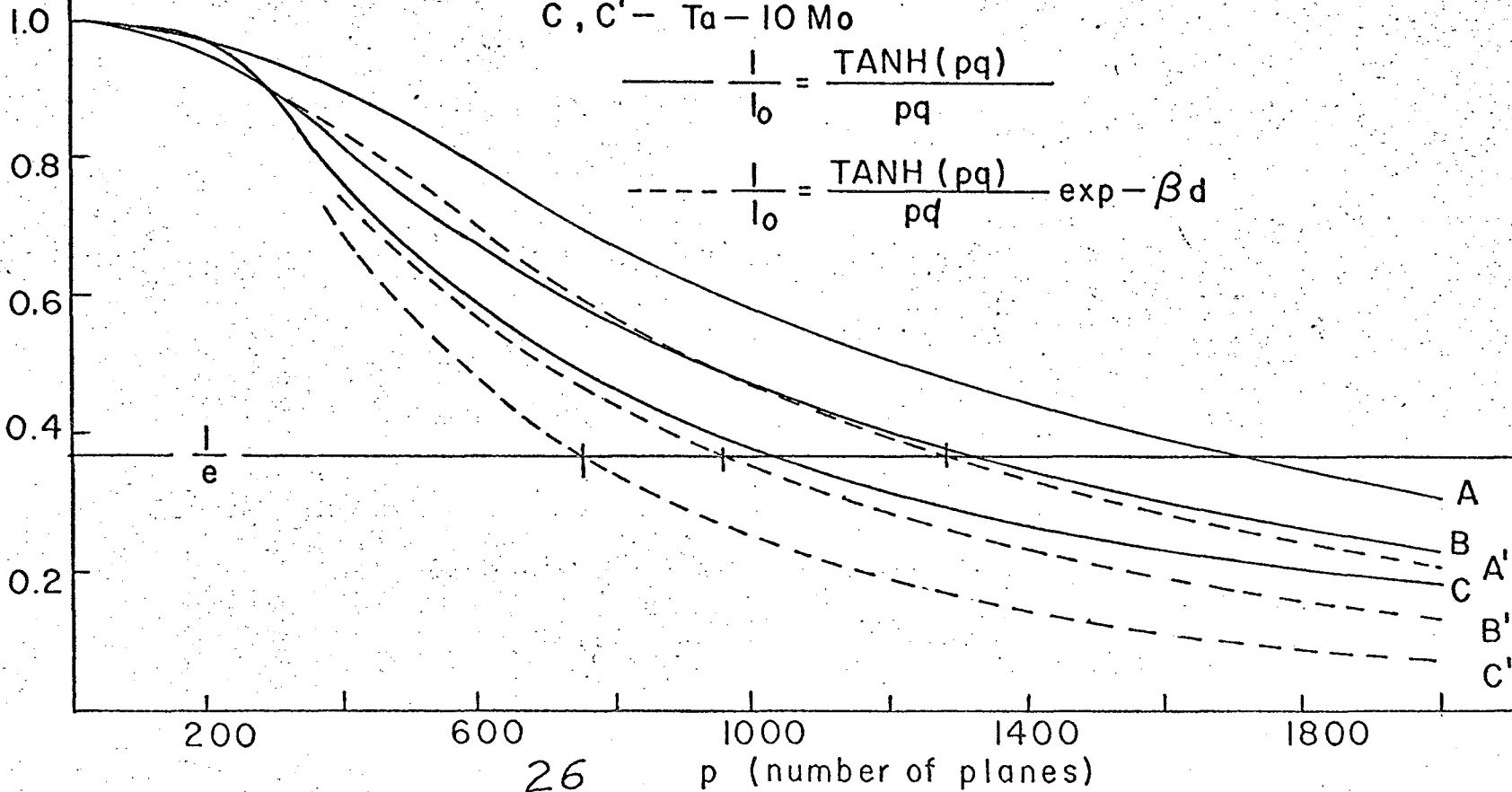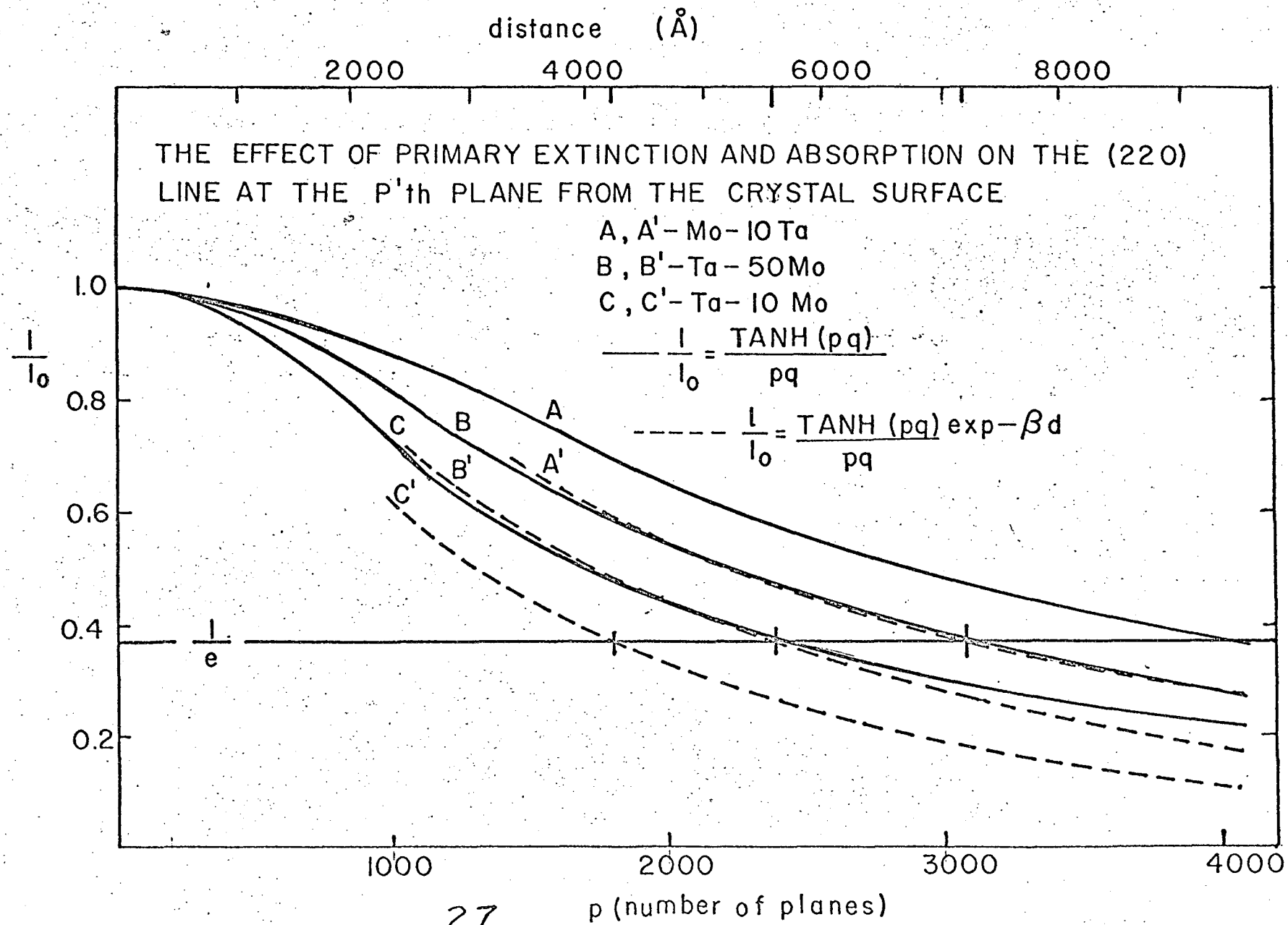
TABLE V. Values of Parameters for X-Ray Intensity Analysis

$N = 8.94 \times 10^{22}$

$\lambda = 1.54 \times 10^{-8}$ cm

$\dfrac{\ell^2}{mc^2} = 2.70 \times 10^{-13}$

$2\theta_{200} = 57.1°$

$2\theta_{220} = 84.9$

$a_{100} = 3.235 \times 10^{-8}$ cm

$a_{110} = 2.29 \times 10^{-8}$ cm

$(200) \begin{cases} \text{Ta-10 Mo, } q_1 = 2.57 \times 10^{-3} \\ \text{Mo-10 Ta, } q_2 = 1.55 \times 10^{-3} \\ \text{Ta-50 Mo, } q_3 = 2.06 \times 10^{-3} \end{cases}$

$(220) \begin{cases} \text{Ta-10 Mo, } q_4 = 1.09 \times 10^{-3} \\ \text{Mo-10 Ta, } q_5 = 6.45 \times 10^{-4} \\ \text{Ta-50 Mo, } q_6 = 8.59 \times 10^{-4} \end{cases}$

$(200) \begin{cases} \text{Ta-10 Mo } |F| = 102 \\ \text{Mo-10 Ta } |F| = 62 \\ \text{Ta-50 Mo } |F| = 81.8 \end{cases}$

$(220) \begin{cases} \text{Ta-10 Mo } |F| = 86.5 \\ \text{Mo-10 Ta } |F| = 51.9 \\ \text{Ta-50 Mo } |F| = 68.1 \end{cases}$

$(200) \begin{cases} \text{Ta-10 Mo, } \beta = 10 \times 10^3 \\ \text{Mo-10 Ta, } \beta = 6.5 \times 10^3 \\ \text{Ta-50 Mo, } \beta = 8.1 \times 10^3 \end{cases}$

$(220) \begin{cases} \text{Ta-10 Mo, } \beta = 5.9 \times 10^3 \\ \text{Mo-10 Ta, } \beta = 3.86 \times 10^3 \\ \text{Ta-50 Mo, } \beta = 4.79 \times 10^3 \end{cases}$

$(200) \begin{cases} \text{Ta-10 Mo, } I_1 = 19.6 \\ \text{Mo-10 Ta, } I_2 = 7.25 \\ \text{Ta-50 Mo, } I_3 = 12.6 \end{cases}$

$(220) \begin{cases} \text{Ta-10 Mo, } I_4 = 9.21 \\ \text{Mo-10 Ta, } I_5 = 3.29 \\ \text{Ta-50 Mo, } I_6 = 5.84 \end{cases}$

with a ratio $\left(\dfrac{I_{200}}{I_{220}}\right)$. The calculated extinction distances given by the curves in Figs. 26 and 27 fix the depth of crystal which contributes to the diffracted intensity. The calculated values of I are necessary for the evaluation of the diffracted intensity contributed by a Ta rich, Mo rich and solid solution region. The values of $|F_{hk\ell}|^2$ have already been shown to be directly related to the alloy composition in a given region of composition deviation. The disposition of the domains of composition deviation with respect to the incident and diffracted beams must now be examined in detail since the path of the beams can lie entirely in a Ta rich or Mo rich region, or it may travel alternately through one region and then the other. The contribution of I to the total intensity will thus depend on the disposition of the domains with respect to incident and diffracted beam paths. There are four cases to consider, namely: composition deviations on {100} as seen by incident and diffracted beams at the diffracting angle θ_{200}, deviations on {100} as seen by the incident and diffracting beams at angle θ_{220}, composition deviations on {110} as seen by incident and diffracted beams at angle θ_{200}, and deviations on {110} as seen by incident and diffracted beams at angle θ_{220}. The above four cases are illustrated by Figs. 28 through 31. Each case is discussed in the following paragraphs.

Case 1: Figure 28(a) is a view along [100] of the three domains generated by composition deviations on {100}. A perspective showing the spatial disposition of the Ta rich and Mo rich regions for each of the three domains is shown in Fig. 28(b). The smallest dimension of a Ta rich or Mo rich region is taken as about 2500 Å. The other two dimensions could be several microns. Consider the (001) domain as seen by incident and diffracted beams. In this case the entire path of the rays of the

VIEW ALONG [100] OF COMPOSITION DEVIATIONS ON {100}
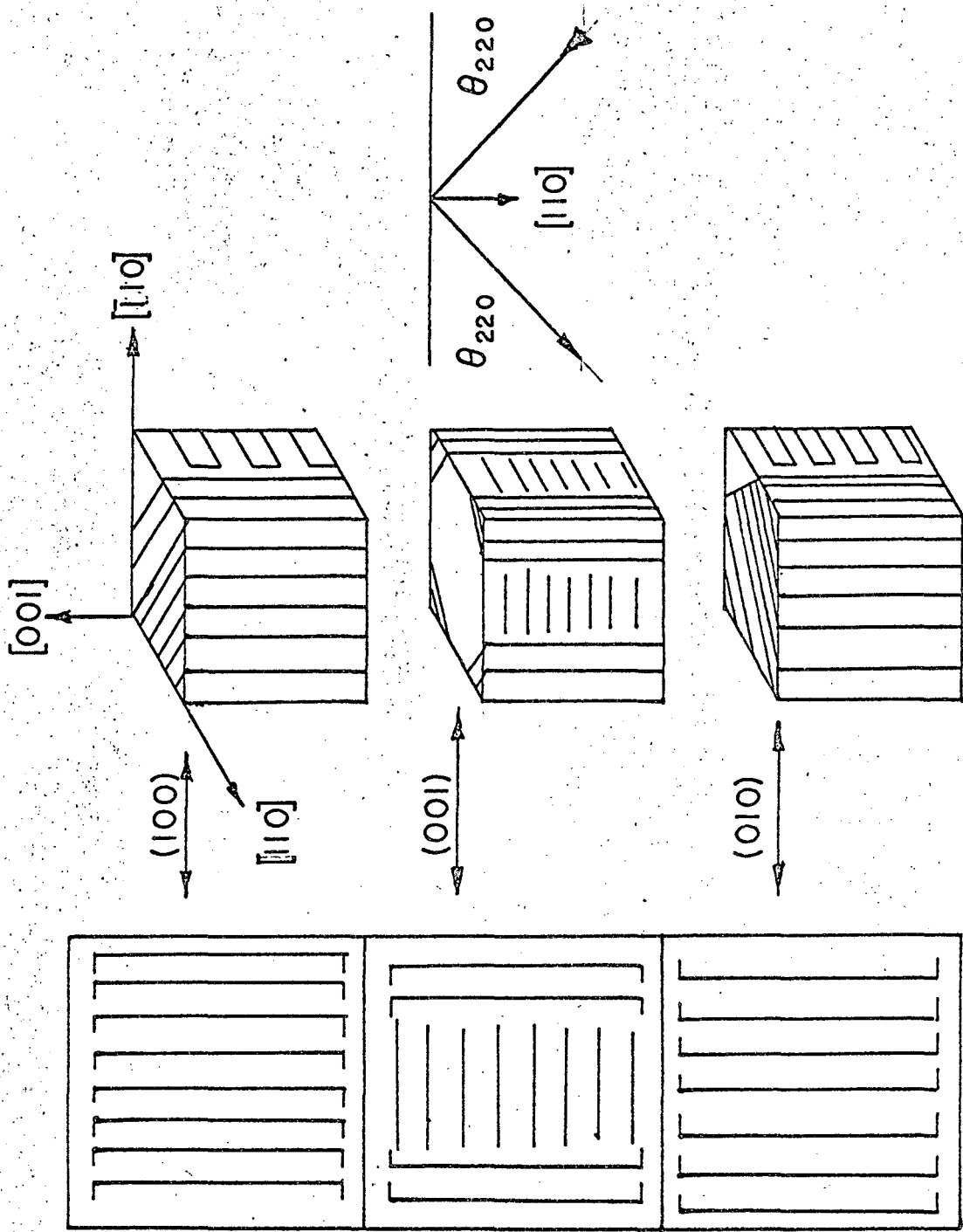
(a) MOTIF

(b)
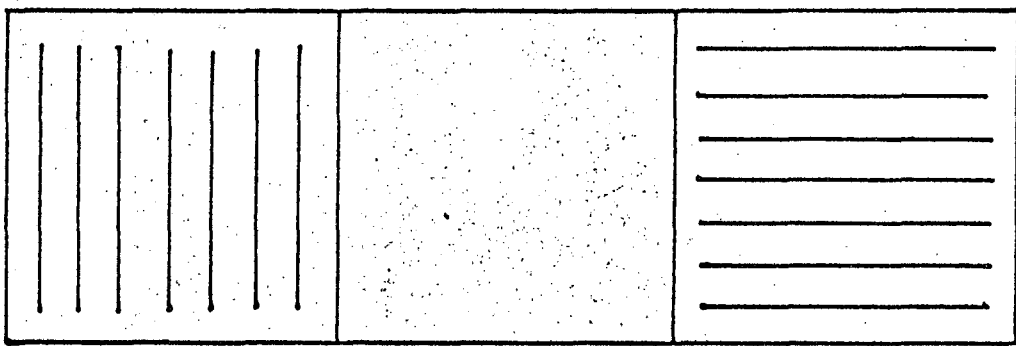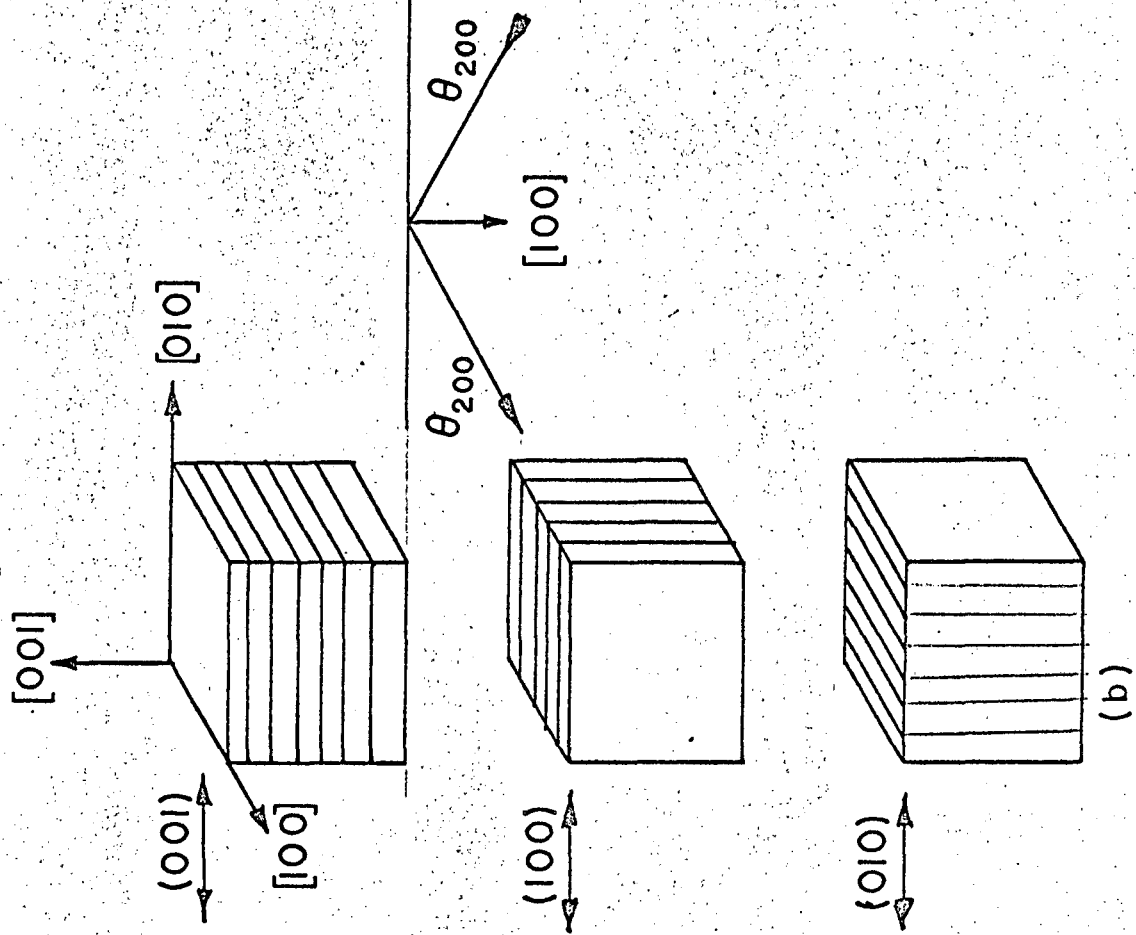
28

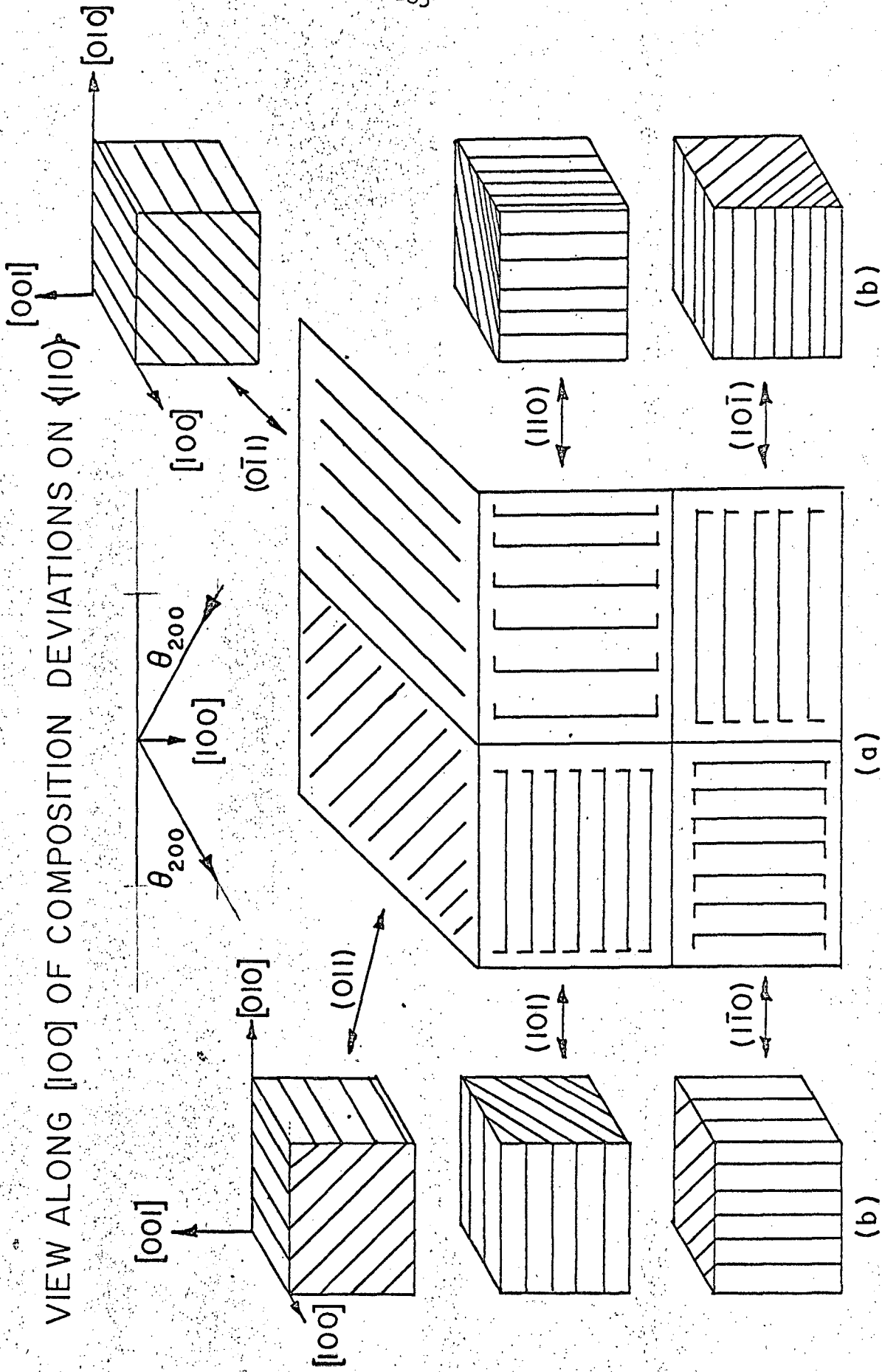VIEW ALONG [110] OF COMPOSITION DEVIATIONS ON {100}

(a)
MOTIF

(b)

29

VIEW ALONG [100] OF COMPOSITION DEVIATIONS ON {110}

MOTIF   30

VIEW ALONG [110] OF COMPOSITION DEVIATIONS ON {110}

MOTIF 31
(a)

(b)
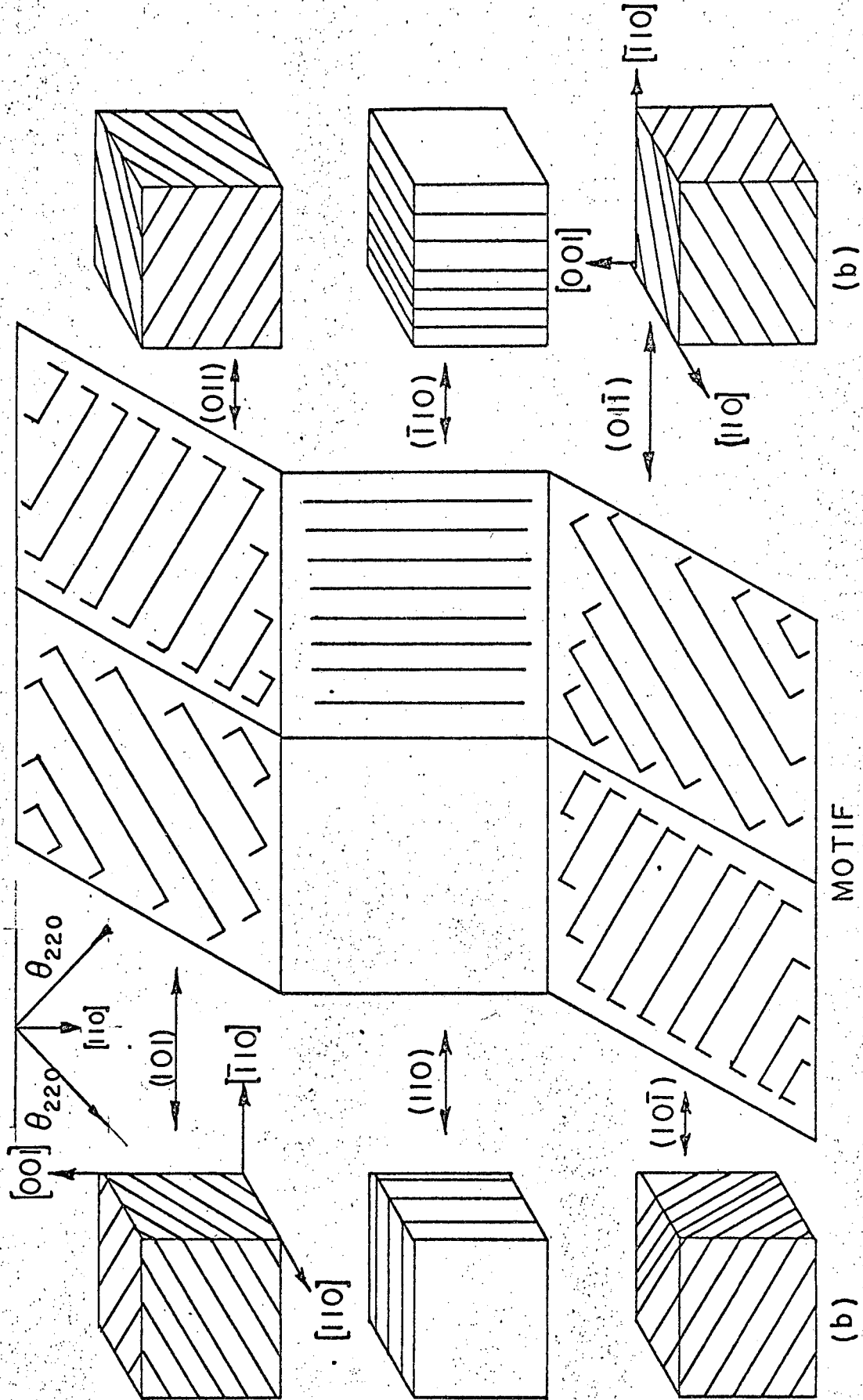
incident and diffracted beams lie either in Ta rich or Mo rich regions, if one neglects the small fraction at the edge of the domain. Thus, (0.500)(0.333) of unit area will diffract according to the value of $|F|^2$ and the extinction length for the Ta rich and the same fraction for the Mo rich region of the (001) domain. Now consider the (010) domain. Due to the geometric disposition of this domain with respect to incident and diffracted beams, the path of the rays traverse both Ta rich and Mo rich regions. Thus, (0.333) of unit area should diffract about like a Ta-50 Mo solid solution. Now consider the (100) domain. One half of these domains will have a Ta rich region exposed at the surface, the other half will be Mo rich. The extinction distance for the (200) line in a Ta rich region (see Fig. 26) is such as to screen the Mo rich region below it from x-radiation. Thus (0.500)(0.333) of unit area diffracts according to the values for a Ta rich region. The extinction distance for the (200) line in a Mo rich region allows the Ta rich region below it to contribute to the diffracted intensity, i.e. I/I_o is about 0.80 at a depth of about 2500 $\overset{\circ}{A}$ of Mo rich region as shown by Fig. 26. Thus, the (100) domain contributes an extra increment of (0.80)(0.500)(0.333) to the total intensity. The fraction of contribution to the total intensity of each domain of the four cases under consideration are summarized in Table VI.

Case 2: Figure 29(a) is a view along [110] of composition deviations on {100}. Figure 29(b) is a perspective view showing the spatial distribution of the Ta rich and Mo rich regions. Note how the (001) domain is cut by a (110) planar section. This effect markedly reduces the fraction of material in which the incident and diffracted rays can travel entirely through a Ta rich or Mo rich region. Thus for the (001) domain only about (0.25)(0.333) diffracts as a Ta rich region and the same fraction

for a Mo rich region. The (100) and (010) domains are disposed so as to require the paths of incident and diffracted rays to lie alternately in Ta rich and Mo rich regions. Thus, the (100) and (010) domains diffract the (200) line about like a Ta-50 Mo solid solution.

Case 3. Figure 30(a) is a view along [100] of composition deviations on {110}. Six domains are generated by this type of deviation since there are six equivalent {110} planes. Figure 30(b) is a perspective view showing the spatial distribution of the Ta rich and Mo rich regions as seen by the incident and diffracted beams for the angle θ_{200}. As can be seen from the figure, the rays of the incident and diffracted beams are required to travel through alternate Ta rich and Mo rich regions in all six domains. Thus the contribution to the total intensity for the (200) line in this case will closely approximate to that of a Ta-50 Mo solid solution.

Case 4. Figure 31(a) is a view along [110] of composition deviations on {110}. Figure 31(b) is a perspective view of the Ta rich and Mo rich regions as seen by incident and diffracted beams at angle θ_{220}. All the domains except (110) will contribute to the total intensity of the (220) line about like a Ta-50 Mo solid solution. Consider the (110) domain, where (0.500)(0.167) will be Ta rich region exposed at the surface and the same fraction of unit area will be Mo rich. Due to the extinction distance of the (220) line in a Ta rich region, the value of I/I_0 is about 0.55 after traveling through this region as shown by Fig. 27. Therefore, the Mo rich region below will contribute about (0.55)(0.500) (0.167) to the total intensity of (220) when a Ta rich region is exposed in a (110) domain. When a Mo rich region is exposed at the surface, the value of I/I_0 is about 0.80 after traveling through this region. Therefore,

TABLE VI. Domain Fractions Contributing to the Integrated Intensity of the (200) and (220) Lines

| | Domain | Composition Deviations on {100} | | |
		Ta-10 Mo	Mo-10 Ta	Ta-50 Mo
(200) line	(100)	(0.500)(0.333)+ (0.80)(0.500)(0.333)	(0.500)(0.333)	
	(010)			0.333
	(001)	(0.500)(0.333)	(0.500)(0.333)	
(220) line	(100)			0.333
	(010)			0.333
	(001)	(0.25)(0.333)	(0.25)(0.333)	(0.50)(0.333)

| | Domain | Composition Deviations on {110} | | |
		Ta-10 Mo	Mo-10 Ta	Ta-50 Mo
(200) line	(011)			0.167
	(101)			0.167
	(1$\bar{1}$0)			0.167
	(0$\bar{1}$1)			0.167
	(110)			0.167
	(10$\bar{1}$)			0.167
	(011)			0.167
	(101)			0.167
	(1$\bar{1}$0)			0.167
	(0$\bar{1}$1)			0.167
	(110)	(0.500)(0.167)+ (0.800)(0.500) (0.167)	(0.500)(0.167)+ (0.550)(0.500) (0.167)	
	(1$\bar{0}$1)			0.167

the Ta rich region below will contribute $(0.80)(0.50)(0.167)$ to the intensity of the (220) line.

The development is now sufficient to make a calculation of the intensity ratio (I_{200}/I_{220}) expected from a Ta-50 Mo random solid solution and compare it to the value calculated for a Ta-50 Mo alloy which contains composition deviations as discussed previously. For a Ta-50 Mo solid solution the value of (I_{200}/I_{220}) is just I_3 divided by I_6 of Table V. The result is $(I_{200}/I_{220})_o$ equal to 2.16 which is quite close to the measured value of 2.04. To calculate the intensity ratio for a crystal with composition deviations on {100}, one just multiplies the contribution from each domain from Table VI by the values of I_x in Table V and takes the sum for I_{200} and I_{220}. Performing the arithmetic one obtains for composition deviations on {100} the value 2.78 for (I_{200}/I_{220}). The value similarly obtained for composition deviations on {110} is 1.91. These values correlate with the observed intensity ratios of the Ta-Mo alloy series with regard to the direction of the change from the random solid solution value of $(I_{200}/I_{220})_o$. However, the observed magnitude of the change for deviations on {100} is somewhat larger than the calculated value. A possible reason for this discrepancy is the neglect of the scattering behavior of the transition region between Ta rich and Mo rich regions. It is likely that the transition region has a large β attenuation factor for rays traveling parallel to its long dimension. The imposition of a large β for this region would have maximum effect on the (220) line for composition deviations as {100} since this beam travels nearly parallel to the transition regions. Since the analysis performed in this discussion predicts the direction of the change in the ratio (I_{200}/I_{220}), it is suggested that composition deviations on {100} and on {110} do occur for the composition

ranges of the Ta-Mo alloy series as shown in Fig. 24. However, a more rigorous analysis of diffracted intensity from the proposed distribution of atoms in the crystal is required to prove the postulated crystal structure of the Ta-Mo alloys which exhibit values of (I_{200}/I_{220}) different from the values measured for Ta and Mo. (See page 89(a)).

The correctness of the interpretation of the intensity data can be substantiated at least for the low alloy composition from a consideration of the elastic compliances of Mo and Ta crystals. The essence of the argument is that in a binary solid solution of constituents which differ in atomic size there will be a tendency for atoms of a given size to distribute themselves within the crystal in a manner which maintains the strain energy of the crystal at a minimum. In the cubic system the elastic coefficients are anisotropic and therefore the compliances (and their inverses, the stiffnesses) vary from one crystallographic plane and direction to another.

Because the elastic compliances and the elastic stiffnesses of a crystal are fourth rank tensors, no single surface can represent completely the elastic behavior of a crystal.[10] However, a surface that is useful is one that shows the variation of Young's Modulus or the rigidity modulus with direction in the crystal. The variation of the reciprocal of Young's Modulus, $(\frac{1}{E})$, in the direction of the unit vector ℓ_i in the cubic system is given by:

$$\frac{1}{E} = S_{11} - 2(S_{11} - S_{12} - \frac{1}{2} S_{44})(\ell_1^2 \ell_2^2 + \ell_2^2 \ell_3^2 + \ell_1^2 \ell_3^2),$$

where S_{11}, S_{12} and S_{44} are the elastic compliances. As an example, if the value of $(\frac{1}{E})$ in the [110] is desired, the components of ℓ_i are

If the smallest dimension of the composition deviation, i.e. the thickness, is about 2000 Å, then the bright field image of an electron micrograph in suitable orientation should exhibit a quasi-banded appearance. This would be a direct result of the difference in linear absorption between a Ta rich and Mo rich region. Such dark bands which are believed to correspond to Ta rich regions are seen in the alloy Ta-12 Mo of Fig. 19(a). An analysis of a standard (311) stereographic projection shows that these dark bands correlate with the traces of the {100} planes. The (001) and the (010) make angles with the surface of about 73° and the (100) makes an angle of about 26°. Therefore, the projected width of the Ta rich region corresponding to (100) will be larger than the other two. This is shown by the figure. The angles between the traces of these bands also correlate with the traces of the {100} planes in this foil orientation. A measured estimate of the width of the region (001) and (010) which project the least difference from the true width gives a value of about 2000 Å. This observation is taken as further evidence for the correctness of the proposed distribution of atoms in alloys of the Ta-Mo series.

$$\ell_1 = \frac{1}{\sqrt{2}} \, , \; \ell_2 = \frac{1}{\sqrt{2}} \; \text{and} \; \ell_3 = \text{zero.}$$

An expression for the reciprocal of the rigidity modulus in the cubic system is given by:[11]

$$\frac{1}{G} = S_{44} + 4(S_{11} - S_{12} - \frac{1}{2} S_{44})(\ell_1^2 \ell_2^2 + \ell_2^2 \ell_3^2 + \ell_1^2 \ell_3^2)$$

where S_{11}, S_{12}, S_{44} and ℓ_i have the same meaning as given above. The values of $(\frac{1}{E})$ and $(\frac{1}{G})$ in some crystallographic directions of interest were computed using the experimentally determined compliances S_{11}, S_{12} and S_{44} for Mo[12] and Ta[13] and are shown in Table VII.

From a comparison of values in the table it is seen that a Ta crystal is most compliant, i.e. less stiff, in and normal to {100}. Therefore, one would expect deviations from random solid solution composition on {100} in the alloy Ta-12 Mo since Ta atoms are slightly larger than Mo atoms. The observed positive deviation of (I_{200}/I_{220}) from the random solid solution value is consistent with this argument. Furthermore, it is seen from Table VII that a Mo crystal is most compliant in and normal to {110}, thus in the alloy Mo-7 Ta deviations from random solid solution composition would be expected on {110}. The observed negative deviation of (I_{200}/I_{220}) from the random solid solution value fulfills this expectation. Hence, the interpretation of the X-ray diffracted intensity results is considered to be correct. Any conclusion based on an extrapolation of the values given in Table VII to higher alloy compositions is considered to be invalid because the intensity, resistivity and mechanical property data strongly suggest that the elastic coefficients do _not_ vary as a simple linear function of the alloy composition.

The region between the alloy compositions of Ta-50 Mo and Ta-42 Mo in Fig. 24 is of particular interest. In this region the elastic

TABLE VII

Elastic compliances under tension parallel to and
torsion about some crystallographic directions in
Ta and Mo crystals in units of $(\text{centimeters})^2/(\text{dyne})$
multiplied by 10^{13}.

ℓ_i		$(\frac{1}{E})$ tension in $[h\ k\ \ell]$	$(\frac{1}{G})$ torsion about $[h\ k\ \ell]$
[100]	Ta	6.78	12.0
	Mo	2.8	9.1
[110]	Ta	5.16	8.73
	Mo	3.3	10.1
[111]	Ta	4.67	7.63
	Mo	2.3	10.4
[112]	Ta	5.16	8.73
	Mo	3.3	10.1

coefficients would be expected to be changing rapidly with alloy composition. In this region the alloy crystal changes from a condition of maximum composition deviation on {100} to a maximum composition deviation on {110} with respect to a random solid solution. If the values at Ta-50 Mo and Ta-42 Mo are extremum values, then the composition deviation on {100} is shown by the dashed line in the figure. Following this line of thought one would predict that the alloy Ta-44 Mo would plot on the random solid solution line. This alloy would then be expected to flow and have the maximum critical resolved shear stress for slip of this alloy series. On the other hand, if the values for Ta-50 Mo and Ta-42 Mo are not the extremum values, then the observed curve will continue to diverge from the random solid solution line with the result that the line connecting the extremum values approaches the vertical, i.e., some alloy in the range between Ta-50 Mo and Ta-42 Mo corresponds to an inflection point on the graph. Following this latter line of thought leads to an interesting consequence in that the composition at the inflection point could correspond to an alloy crystal which is energetically unstable, because the compliances do not satisfy the restrictions;[14]

$$s_{44} > 0, \ s_{11} > |s_{12}|, \ s_{11} + 2s_{12} > 0$$

which is imposed by the fact that the strain energy of a crystal,

$$W = \frac{1}{2} C_{ij} \, \epsilon_i \epsilon_j$$

must be positive, i.e. greater than zero for all real values of ϵ_{ij} unless all ϵ_{ij} are zero. In the strain energy expression, C_{ij} are the stiffness coefficients and ϵ_{ij} are the strains. A systematic determination of the elastic coefficients of this alloy system would distinguish between

the two above possibilities. Because the purpose of this investigation is to determine the reason for the appearance of cleavage in this alloy system, the remainder of the discussion will be confined to that topic.

III-B Interpretation and Analysis of Mechanical Properties

The observed values of the critical resolved shear stress for slip on {110} <111> and for cleavage on {100} as a function of alloy composition are given in Fig. 14. It is apparent from the figure that those crystals having compositions in the range from Mo-19 Ta to Mo-58 Ta fail by the mode of cleavage. The crystals having compositions in the range Mo to Mo-7 Ta and Ta to Ta-30 Mo deform by plastic flow. For those alloys which flow plastically, the tensile tests were continued until there was visual evidence of striction i.e. necking of the crystal. All those crystals which flowed plastically necked with the sole exception of Mo-7 Ta. This crystal showed nearly uniform reduction in diameter along the entire gage length with a nearly uniform distribution of slip lines as indicated by 30x magnification. As was mentioned previously in the Procedure and Results no correlation could be obtained between the resolved normal stress on the cleavage plane as a function of alloy composition, e.g. changes in normal stress of 60 Kg/mm^2 in nine atomic per cent increments are considered to be unrealistic. The resolved shear stress on the observed cleavage plane at failure are the values plotted in Fig. 14. It is seen from the figure that the minimum observed cleavage shear stress occurs for Mo-28 Ta and the maximum observed cleavage shear stress occurs for Mo-19 Ta and Mo-58 Ta whose values are about the same. Because of the appearance of slip lines on those crystals that cleave some plastic flow also occurs in these alloys.

The probable mechanism responsible for the strengthening as the alloy composition increases for the crystals which fail by plastic flow will be discussed first. The proposed models[15] of solid solution strengthening predict a linear relationship between the critical resolved shear stress for slip and the concentration of solute atoms. In order to determine if there was a functional dependence of the critical resolved shear stress for slip and solute atom concentration in this alloy system the ln τ was plotted against ln c. Where τ is the critical resolved shear stress and c the atomic fraction of Mo. The plot was made for Ta base alloys from zero to 30 atomic percent Mo. A simple functional dependence of τ upon c over this range of composition was not observed, even when the point at Ta-12 Mo was omitted on the basis that this alloy shows deviations from random solid solution composition on {100}. It was therefore concluded that the models proposed for solid solution strengthening are not applicable to this alloy system.

The mechanisms involved in the strengthening of those alloy crystals which flow plastically and the transition to a cleavage mode of failure at high alloy compositions is the result of a complicated interaction and interdependence between the following:

a) The Peierls-Nabarro friction of dislocations, and its variation with alloy composition

b) Deviations from random solid solution composition on {100} in some alloys and on {110} in others

c) Changes in the elastic coefficients upon alloying

d) Changes in the elastic coefficients within regions of the crystal as a result of (b)

e) Violations of the strain energy restrictions upon the elastic coefficients due to (b), (c) and (d) above.

The Peierls-Nabarro friction of dislocations appears to be a physical phenomena to which is attributed much mechanical behavior but detailed knowledge about it is meager. The reason that P-N friction is not well understood is that a detailed knowledge of the directionality and magnitude of interatomic forces within the core of a dislocation is lacking. Although very little detailed knowledge of the P-N friction is available the derivation of the force necessary to move a dislocation, derived from assumptions inherent in the use of an elastic continuum, is considered to be qualitatively correct. The expression that is given for the shear stress necessary to move a dislocation on crystal planes spaced a distance "a" apart and "b" distance between atoms in the plane is,[16]

$$\sigma \simeq \frac{2\mu}{K} \exp \left[- \left(\frac{2\pi a}{Kb}\right)\right]$$

where μ is the shear modulus and K assumes the value 1 for the screw dislocations and 1 - Poisson's ratio for an edge. The essential feature of this expression is that the shear stress is exponentially dependent upon the atomic configuration at the core of the dislocation. In crystals where the magnitude and directionality of the interatomic forces are large the distortion produced by the core of the dislocation would be expected to be restricted to a narrow region and thus the shear stress required to move the dislocation would increase exponentially. Furthermore, such conditions would tend to make the dislocations in a crystal lie in straight lines which correspond to regions in the crystal of minimum core energy. The progressive tendency for dislocations to lie along straight lines is shown by the electron micrographs of Fig. 19 as the Mo content of Ta base alloys increases from zero to 30 atomic percent. Such observations strongly suggest that the P-N friction is increasing as the alloy

content increases. Therefore, the observed increase in critical resolved shear stress for slip is the result of a marked increase in the P-N friction of dislocations.

Deviations on {100} and {110} from random solid solution composition as well as changes in the elastic coefficients which are directly related to the magnitude and directionality of the interatomic forces will produce changes in the P-N friction. Changes in the elastic coefficients will result from both composition deviations and simple alloying.[2,17,18] The changes in the elastic coefficients which will have the greatest effect on the P-N friction are those changes in S_{44}, S_{11} and S_{12} which produce the greatest deviation in the isotropic condition for the compliances $S_{44} = 2(S_{11}-S_{12})$ or as written for the stiffnesses $C_{44} = \frac{C_{11}-C_{12}}{2}$. It was shown previously in the interpretation of the intensity data that the observed composition deviations for the lowest alloy composition crystals were directly related to the elastic coefficients of Ta and Mo. From an intuitive physical argument, composition deviations on {100} and {110} are interdependent with the elastic coefficients, e.g. from Fig. 24 the Ta {100} are the most compliant thus the alloy crystal Ta-12 Mo exhibits a composition deviation such that there are Ta rich and Mo rich regions on {100} which would not exist in a random solid solution. Because of this, the compliance in and normal to {100} in Ta-12 Mo will change. In order to verify the above concepts, the elastic coefficients as a function of alloy composition are required. These have not been determined at the present.

The models that have been proposed for the mechanisms of cleavage[19] invoke the stress normal to the cleavage plane as being the determining parameter. The normal stress shows no obvious significance in the

cleavage of the alloys of this investigation. However, as can be seen from Fig. 14 there is an increase in the shear stress on the cleavage plane as the alloy composition increases or decreases from Mo-28 Ta. One can reason that the minimum cleavage shear stress will occur when the elastic shear strain energy is at a maximum at some region in the crystal. In a Ta-Mo alloy crystal one would expect the maximum shear strain energy to be attained in regions which possess the largest internal strain energy. When there exists deviations from random solid solution composition on {100} the maximum shear strain energy will be attained in the Ta rich, Mo rich or transition regions which lie parallel to the cleavage plane. In the Ta-42 Mo crystal which exhibits deviations on {110}, the intersection of (110) and (1$\bar{1}$0) domains generate a transition region which lies parallel to the (010) plane. This is a likely region where changes in C_{ij} are occurring.

Because slip lines are observed on those crystals that cleave and that the cleavage appears to be dependent on shear stress, the detailed mechanism of cleavage in this alloy system must include the influence of dislocations. The fact that the presence of dislocations in a crystal can change the magnitude of the elastic coefficients in local regions of the crystal has been recognized and discussed.[20] The proposed mechanism for cleavage in the Ta-Mo alloy system is as follows: In the range of alloy compositions which exhibits cleavage the values of the elastic compliances are such that the restriction imposed on the compliances by a positive strain energy of a crystal are only marginally fulfilled. Recalling that these restrictions are:

$$a) \quad S_{44} > 0$$

b) $S_{11} > |S_{12}|$

c) $S_{11} + 2S_{12} > 0$

A substitution of the values for pure Ta, i.e. $S_{11} = 6.78 \times 10^{-13} cm^2/d$, $S_{12} = -2.47 \times 10^{-13} cm^2/d$ and $S_{44} = 11.93 \times 10^{-13} cm^2/d$, show that an increase in $|S_{12}|$ of 0.92 is sufficient to violate restriction (c). The same analysis using values for Mo show that an increase in the $|S_{12}|$ of only 0.62 is sufficient to violate restriction (c). Therefore, it is probable that under the influence of alloying and the associated composition deviations the restrictions on the compliances, which are the same as on the stiffnesses, are just marginally satisfied in those alloys which cleave. The role of dislocations in this mechanism is to alter the elastic compliances to values which no longer satisfy the above restrictions in regions of the crystal where the dislocation density has achieved some critical value. The crystal then becomes energetically unstable and parts along a crystallographic set of planes which releases a maximum amount of strain energy. Due to the lack of a detailed knowledge of the elastic coefficients of these alloy crystals, the exposition of the proposed mechanism cannot be made in a more pleasing quantitative manner.

The behavior of the lattice parameter as a function of alloy composition, Fig. 17, exhibits no marked anomalies. Beyond the composition MO-7 Ta a positive deviation from Vegard's Law is observed. The maximum deviation occurs near the alloy compositions Mo-33 Ta, (minimum cleavage shear stress) and the second largest deviation occurs near Ta-30 Mo (maximum shear stress for slip). The purpose of measuring the lattice parameters of the alloy series was to determine if there existed any changes in the lattice parameter at some particular alloy composition.

As can be seen from the figure, no marked changes are observed.

The following will be a summary of the electron microscope observations. The dislocation substructures of the alloys which flow plastically have a very similar appearance to each other and to other tensile deformed metals, e.g. Cu, Nb and Fe. The tendency for the dislocations to lie in straight lines which is most manifest in Ta-30 Mo, maximum alloy composition which flows, is apparent in the micrographs and is taken as evidence for an increase in the P-N friction with an increase in alloy composition. The fresh dislocations in the micrograph of Ta-42 Mo are seen to be unextended and straight which indicates that if short range order is present, the largest dimension of the ordered region is less than about 300 Å. Mo-40 Ta, Mo-28 Ta and Mo-19 Ta showed no particular features of interest. The dislocations shown in the micrographs are residual, i.e. grown in. The dislocation arrangement after tensile deformations in Mo-7 Ta is equivalent to that of Ta. There were no unusual diffraction effects observed during all the tilting experiments. A composition deviation from random solid solution would not be expected to show any observable effects either in the bright or dark field electron image or diffraction pattern unless there existed appreciable strain fields associated with the deviation or the constituent in excess assumed some periodic arrangement in the crystal. The above applies for diffraction contrast. However, when the deviations are normal to the foil surface, then dark and light bands will appear due to the difference in linear absorption. (See page 89(a).)

III-C Electrical Transport Properties

It is necessary to present a summary of the theory of electrical transport processes in the transition metals before any meaningful discussion of the observations can be presented. The following theory was

first proposed by Mott[21] and has been recently discussed by Ziman.[22] The brief exposition of the theory as given here parallels that of Ziman.

It is the consensus that in the transition metals the s-band and d-band have considerable overlap. The s-band contains nearly as many almost free electrons as in a "normal" monovalent metal. The d-bands are rather narrow and partially filled with electrons, the fermi velocity of the electrons in these bands being much lower than in the s-band. The d-band is composed of five sub-bands each of which can accommodate two electrons per atom.

From the elementary solution of the transport equation, when there is elastic scattering of electrons, the electron distribution function deviates from equilibrium by an amount which is proportional to $\vec{v}_{\vec{k}}$, e.g.,

$$f_{\vec{k}} - f_{\vec{k}}^{\circ} = \frac{\vec{v}_{\vec{k}}^{\circ} \dfrac{\partial f_{\vec{k}}^{\circ}}{\partial T} \nabla T - \ell \dfrac{\partial f_{\vec{k}}^{\circ}}{\partial \epsilon_{\vec{k}}} \vec{E}}{\int (1-\cos\theta) Q((\vec{k}-\vec{k}'),\theta) d\Omega} \qquad \text{Eq. (1)}$$

An explanation of the notation must now be given. $Q((\vec{k}-\vec{k}'),\theta)\, d\Omega$ is a differential transition probability which is the probability that an electron of momentum $\hbar\, \vec{k}$ is scattered through an angle θ into solid angle $d\Omega$, θ being the angle between $\vec{k}$ and $\vec{k}'$, the transition probability per unit time for the process $\vec{k} \to \vec{k}'$, i.e. an electron in state $\vec{k}$ being scattered into state $\vec{k}'$ is written

$$P_{\vec{k}}^{\vec{k}'} \, d\vec{k}' = f_{\vec{k}}(1-f_{\vec{k}}) Q_{\vec{k}}^{\vec{k}'} \, d\vec{k}'. \quad Q_{\vec{k}}^{\vec{k}'} \text{ is } Q[(\vec{k}-\vec{k}'),\theta]$$

in vector form. The factor $f_{\vec{k}}(1-f_{\vec{k}})$ is a result of the fact that electrons obey fermi statistics and thus for the process $\vec{k} \to \vec{k}'$, $f_{\vec{k}}$ accounts

for an electron being in state $\underset{\rightarrow}{k}$ and $(1-f_{\underset{\rightarrow}{k}})$ accounts for the state $\underset{\rightarrow}{k}'$

being unoccupied. $f^o_{\underset{\rightarrow}{k}}$ is the unperturbed fermi distribution of electrons

and $f_{\underset{\rightarrow}{k}}$ is the perturbed distribution function. $\underset{\rightarrow}{v}_{\underset{\rightarrow}{k}}$ is the velocity of an

electron in state $\underset{\rightarrow}{k}$. ∇T is the gradient of the temperature in the crystal.

$\underset{\rightarrow}{E}$ is the applied electric field. e is the electron charge. $\epsilon_{\underset{\rightarrow}{k}}$ is the

energy of an electron in state $\underset{\rightarrow}{k}$. Because the deviation in the distribu-

tion function is proportional to $\underset{\rightarrow}{v}_{\underset{\rightarrow}{k}}$, the trial function should be written

in the form

$$\underset{\rightarrow}{\Phi}_{\underset{\rightarrow}{k}} = \underset{\rightarrow}{v}_{\underset{\rightarrow}{k}} \cdot \underset{\rightarrow}{u} \qquad\qquad \text{Eq. (2)}$$

for insertion in the variational expression for the resistivity. $\underset{\rightarrow}{u}$ is

the phonon velocity. The influence of $\underset{\rightarrow}{\Phi}_{\underset{\rightarrow}{k}}$ is seen in the expression which

defines the perturbed fermi distribution

$$f_{\underset{\rightarrow}{k}} \equiv f^o_{\underset{\rightarrow}{k}} - \underset{\rightarrow}{\Phi}_{\underset{\rightarrow}{k}} \frac{\partial f^o_{\underset{\rightarrow}{k}}}{\partial \epsilon_{\underset{\rightarrow}{k}}} \qquad\qquad \text{Eq. (3)}$$

The term $-\dfrac{\partial f^o_{\underset{\rightarrow}{k}}}{\partial \epsilon_{\underset{\rightarrow}{k}}}$ which is equal to $f^o_{\underset{\rightarrow}{k}}(1-f_{\underset{\rightarrow}{k}})/kT$ has a sharp maximum at

the fermi surface and thus $P^{\underset{\rightarrow}{k}}_{\underset{\rightarrow}{k}} \, d\underset{\rightarrow}{k}'$ is finite only for electron states

within about kT $(\sim \frac{1}{40} \text{ eV})$ of the fermi surface.

Recall that the electrons which are involved in the transport process

are divided into two groups. A group in the s-band with nearly spherical

fermi surface and normal free electron energy $E_{\underset{\rightarrow}{k}}$. The other group is in

the d-band whose fermi surface is complex since it is composed of sub-

bands and here the fermi velocity is much lower. In this discussion

electron transitions are produced by lattice vibrations, i.e. electron-

phonon interactions, where only normal processes $\underset{\rightarrow}{k} \pm \underset{\rightarrow}{q} = \underset{\rightarrow}{k}'$ as contrasted

with U-processes $\underset{\rightarrow}{q} = \underset{\rightarrow}{k} - \underset{\rightarrow}{k}' \pm \underset{\rightarrow}{g}$ are considered. $\underset{\rightarrow}{g}$ is a reciprocal lattice

vector and $\vec{q}$ is a phonon wave vector.

Upon insertion of the trial function, Eq. (2), into the variational

expression for the electrical resistivity

$$\rho = \frac{\frac{1}{kT} \iiint \left(\overline{\Phi}_{\vec{k}} - \overline{\Phi}_{\vec{k}'}\right)^2 P_{\vec{k}\ \vec{q}}^{\vec{k}}\ d\vec{k}\ d\vec{k}'\ d\vec{q}}{\left| \int \ell\ v_{\vec{k}}\ \overline{\Phi}_{\vec{k}}\ \frac{\partial f_{\vec{k}}^{\circ}}{\partial \epsilon_{\vec{k}}}\ d\vec{k}\ \right|^2} \qquad \text{Eq. (4)}$$

the numerator can be separated into three terms each divided by the same

denominator. The three terms in the numerator are:

a) $< \overline{\Phi}_s,\ P\overline{\Phi}_s >$ corresponding to electron scattering from s to s

states.

b) $< \overline{\Phi}_s,\ P\overline{\Phi}_d >$ corresponding to s to d state scattering.

c) $< \overline{\Phi}_d,\ P\overline{\Phi}_d >$ corresponding to d to d state scattering.

The notation $< \overline{\Phi}_s,\ P\overline{\Phi}_d >$ is used which means

$$\frac{1}{2} \iint \{\phi_s(\vec{k}) - \overline{\Phi}_s(\vec{k}')\}\ P_{\vec{k}}^{\vec{k}'}\ \{\overline{\Phi}_d(\vec{k}) - \overline{\Phi}_d(\vec{k}')\ \}\ d\vec{k}\ d\vec{k}'$$

Each of the matrix elements (a), (b) and (c), divided by the same denomi-

nator, contributes to the total resistivity. The denominator can be

written

$$|< \overline{\Phi},\ P(E=1)\ \overline{\Phi} >|^2 =$$

$$\{ \frac{1}{4\pi^3} \int \ell\ \vec{v}_{\vec{k}} \cdot \vec{v}_{\vec{k}} \cdot \vec{u}\ \frac{\partial f_{\vec{k}}^{\circ}}{\partial \epsilon_{\vec{k}}}\ d\ G\ \frac{d\epsilon_{\vec{k}}}{hv} = \left(\frac{\ell}{12\pi^3 h}\right)^2 \{ v_s G_s + v_d G_d \}^2 \qquad \text{Eq. (5)}$$

where $P(E=1)$ is the transition probability in unit applied electric field, G_s and G_d are the areas of the fermi surfaces and v_s, v_d the velocities for the two bands. The plausible assumption that $v_s \gg v_d$ can be made and although G_d may be comparable to G_s the term $v_d G_d$ can be neglected compared to $v_s G_s$. Thus, most of the current is carried by the electrons in the s-band.

The contribution to the total resistivity due to s-s scattering processes, ρ_{ss}, is unaffected by the presence of a full or partially full d-band. The matrix element for this process, $< \phi_s, P\phi_s >$, would be expected to be about the same as in normal monovalent metals. In the presence of a partially filled d-band, the contribution to the total resistivity due to s-d scattering process, ρ_{sd}, would be significant since ρ_{sd} can be written

$$\rho_{sd} \sim \frac{9\pi h}{2\ell^2 mNkT v_s^2 G_s^2} \iint \frac{(v_s-v_d)^2 \{(\vec{k}-\vec{k}')\cdot\vec{e}\}^2 \{I_{sd}(\vec{k}-\vec{k}')\}^2 dG_s \, dG_d}{(1-\exp-\frac{hv}{kT})(\exp\frac{hv}{kT} - 1)} \quad \text{Eq. (6)}$$

where m is the electron mass in s-band,

N is number of electrons in s-band per unit volume.

K is Boltzmann's constant

$\vec{e}$ is the polarization vector of the phonons.

Now, ρ_{sd} will be different from ρ_{ss} by a factor

$$\frac{\rho_{sd}}{\rho_{ss}} \sim \frac{\{I_{sd}(\vec{k}-\vec{k}')\}^2}{\{I_{ss}(\vec{k}-\vec{k}')\}^2} \quad \text{Eq. (7)}$$

$I(\vec{k}-\vec{k}')$ is a quantity having the dimensions of an energy but depends on the magnitude of the scattering vector $\vec{k}-\vec{k}'$. When the value of the function

$I_{sd}(\underline{k}-\underline{k}')$ which appears in Eq. (6), for the s-d process has a value comparable to that in an s-s process, the contribution to the total resistivity by s-d scattering should be greater than ρ_{ss} by about the ratio of the density of states in the s and d bands. Hence, the increase in resistance of transition metals with respect to normal monovalent metals should be proportional to this factor.

The calculation of the electronic energy bands in a tungsten crystal has been performed by Manning and Chodorow[23] using a Wigner-Seitz-Slater cellular method. The density of states obtained by them may be used to indicate the plausibility of Mott's theory of electron transport in transition metals. The density of states as calculated for tungsten by Manning and Chodorow and with ordinate and abscissa scales transformed by Wilson[24] is shown in Fig. 32. The position of the fermi level corresponding to six s+d electrons for tungsten and five s+d electrons for tantalum are indicated by the vertical lines. Although the density of states as shown was calculated for tungsten, it should be essentially the same for tantalum which immediately precedes tungsten in the third long series of the periodic table. In the figure, bands marked I through V are the five sub-bands of the d-band and VI corresponds to the s-band in the crystal. The density of states of band VI (the s-band) and the d-sub band V have an appreciable value to high energies which indicates considerable overlap of the respective electron wave functions in the crystal. The electrons in states of these two bands can be expected to behave as nearly free electrons. Furthermore, the electrons in band I will play no part in the transport process, since these states are far below the fermi level. According to Mott's theory, as summarized previously, the resistivity of tantalum with respect to tungsten should be in the same proportion as the ratio of
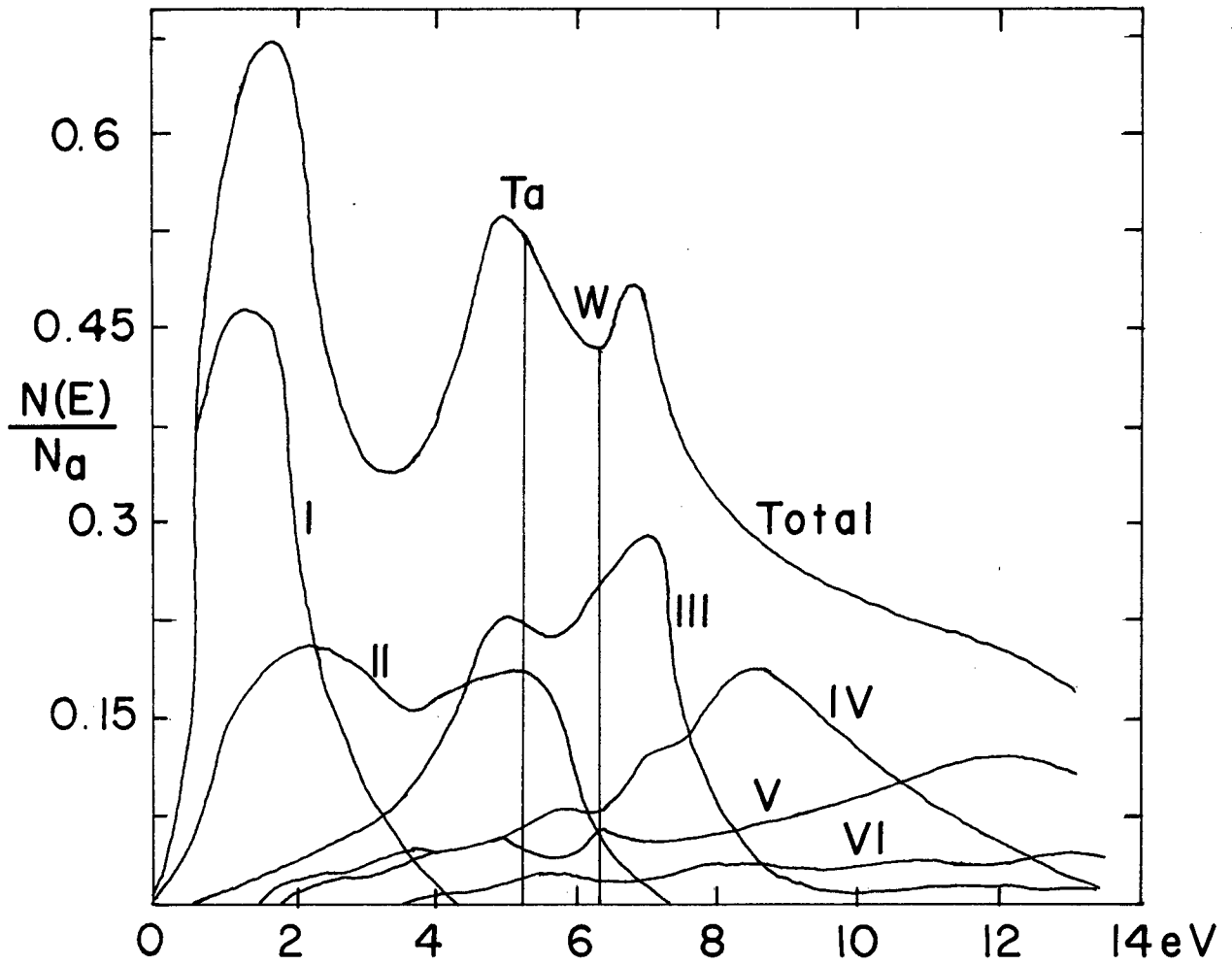
THE DENSITY OF STATES PER
ATOM IN TANTALUM AND TUNGSTEN
from M.F. MANNING and M.I. CHODOROW

MUB-4435

Fig. 32

density of states of those electrons having d-character to those having s-character. The ratio can be taken from Fig. 32 at the fermi level for tantalum and tungsten. The electron in bands II, III and IV will have d-character and those in bands V and VI will behave as being nearly free, i.e. s-character.

Before a comparison between the density of states ratio to the observed resistivities can be made, the thermal contribution to the resistivity must be factored out, since the thermal contribution will be different for the two metals. Mott and Jones[25] have shown that the different amplitudes of thermal vibrations of the ions at a given temperature can be corrected for by the factor

$$\frac{\sigma}{M\theta^2}$$

where σ is the conductivity of a unit cube, M is the mass of the vibrating ion and θ is the Debye temperature of the crystal. For comparative purposes, it is the conductivity of a fixed number of ions that is of interest. This is accounted for by inserting the radius of the ion into the denominator of the above expression, thus giving the result

$$\frac{\sigma}{M\,r\,\theta^2}$$

for the normalized conductivity. Using the values given in Table X by Mott and Jones[25] and dividing by the respective radii, the normalized conductivity for tantalum is 0.54 and for tungsten 0.73. These values give a normalized resistivity ratio

$$\frac{\rho_{Ta}}{\rho_W} = 1.3.$$

The density of states in bands II, III and IV divided by the density of states in bands V and VI at the fermi level for Ta give a value

$$\left.\frac{n(E)d}{n(E)s}\right|_{Ta} = 0.63$$

The similar ratio at the fermi level for tungsten is

$$\left.\frac{n(E)d}{n(E)s}\right|_{W} = 0.48$$

The ratio

$$\frac{\left.\frac{n(E)d}{n(E)s}\right|_{Ta}}{\left.\frac{n(E)d}{n(E)s}\right|_{W}} = \frac{0.63}{0.48} = 1.3$$

shows quite good agreement with the observed resistivity ratios of tantalum and tungsten. This result suggests that Mott's model is essentially correct.

A qualitative prediction of the resistivity behavior as a function of alloy composition in the Ta-W series could be made from the density of states as shown in Fig. 31 only if the following conditions were satisfied:

a) the alloy series forms a random solid solution, i.e. no composition deviations as observed in tha Ta-Mo series,

b) a method of normalizing the temperature contribution to the resistivity can be derived.

These same conditions would apply to the Nb-Mo series if one were to calculate the density of states for Mo or Nb. Condition (b) could be met by measuring the lattice parameters and the elastic coefficients as a function of alloy composition. An average ion mass and radius could be taken for the alloy for M and r respectively. The Debye temperature for each alloy can be calculated from the determined elastic coefficients.[25] The residual resistivity could be factored out as was done for Ta-Mo in Fig. 6. The failure to satisfy condition (a) is an inherent property of

the alloy series Ta-Mo and probably also for Nb-Mo, Ta-W and Nb-W. Such

deviations from random solid solution composition would surely produce

electronic charge density deviations in the crystal and the affect of

these on the transport properties would be difficult to account for.

The task of calculating the density of states for the Ta-Mo or Nb-W

alloy series would be formidible, since, among other factors, the poten-

tial of the ion cores of the alloy constituents differ from each other

considerably.

The observed behavior of the resistivity of the Ta-Mo alloy series

as shown in Fig. 6, where the residual resistivity has been factored out,

is the result of a non-linear change in the elastic coefficients and

variation of $\frac{n(E)d}{n(E)s}$ with alloy composition as well as composition devia-

tions. The amount each of these factors contribute to the observed

resistivity in Fig. 6 must remain unknown until at least the elastic

coefficients have been determined as a function of alloy composition.

There is an interesting observation concerning a connection of the

resistivity $\rho_{273°K}-\rho_{4.2°K}$ of Ta and Mo and the compliances S_{11}. The

ratio of resistivities is about equal to the ratio of compliances, e.g.

$$\frac{(\rho_{273°K} - \rho_{4.2°K})_{Ta}}{(\rho_{273°K} - \rho_{4.2°K})_{Mo}} \overset{\circ}{=} \frac{(S_{11})_{Ta}}{(S_{11})_{Mo}} \quad \text{being 2.43 and 2.42 respectively.}$$

This is reasonable since the thermal amplitude of vibration of the ion

would be a function of a combination of the S_{ij}, with the longitudinal

phonons having maximum effect for scattering electrons.

The behavior of the resistivity as a function of alloy composition

in the Ta-Mo alloy series as shown in Fig. 6 indicates that there is a

marked change in $\frac{n(E)d}{n(E)s}$ and/or in the elastic coefficients near the

compositions, Mo-20 Ta, Mo-50 Ta and Ta-12 Mo since there is a marked

change in the slope of the curve at these compositions. For this reason,

these alloy compositions should merit special attention in future studies.

IV. CONCLUSIONS

1. The Ta-Mo alloy single crystals cleave under tensile loads in the composition range Mo-19 Ta to Mo-58 Ta on {100} planes at 273°K.

2. The critical resolved shear stress for plastic flow is a non-linear function of alloy composition. The increase in the shear stress for flow is the result of an increase in the Peierls-Nabarro friction of a dislocation which occurs through composition deviations on {100} or {110}, alloying and changes in the elastic coefficients.

3. The Ta-Mo alloy series has a bcc crystal structure showing no long range or short range order with dimension > 300 Å, or intermediate phases.

4. The lattice parameter versus alloy composition shows a positive deviation from Vegard's Law for all compositions from Mo-18 Ta to pure Ta.

5. The composition on {100} planes deviates from a random solid solution composition for alloys in the range Mo-19 Ta to Mo-50 Ta. These alloys show cleavage at 273°K which appears to be dependent on the shear stress on the cleavage plane {100}.

6. The proposed mechanism of cleavage is as follows. Cleavage occurs due to a violation of the strain energy restrictions on the elastic coefficients in a local region of the crystal. Alloying and the existence of crystallographic composition deviations change the elastic coefficients, in the range of alloys which cleave, to values which marginally fulfill the restrictions imposed on them by the necessity of a positive definite strain energy. The presence of a critical number of dislocations in a local region produces changes in the values of the elastic coefficients such that the strain energy restrictions are violated in this region. The crystal is then energetically unstable and cleaves on the crystallographic plane which releases the maximum strain energy.

7. Marked changes occur in the density of electron states in the d and s band and/or in the elastic coefficients at the composition Mo-20Ta, Mo-50 Ta and Ta-12 Mo.

ACKNOWLEDGMENTS

The author is most grateful for the encouragement and support from Professor Gareth Thomas during his supervision of the research. The constructive criticism offered by Professor Jack Washburn has led to a deeper understanding of the complexities of this research and the author therefore wishes to thank him for it. I wish to thank Mrs. Pat Cookson and Mrs. Joan Forney for their diligence and promptness in the typing of both drafts of this thesis.

This research was done under the auspices of the United States Atomic Energy Commission.

APPENDIX I

Comparison of the Elastic Compliances of Nb, Ta, Mo and W

There are some interesting observations to be made through a comparison of the elastic coefficients of the elements Nb, Ta, Mo and W. The elastic compliances and the margin of fulfillment of the strain energy restrictions on the compliances are shown in Table A1. It is quite evident from columns 5 and 6 that the margin of fulfillment of the restrictions on the compliances decreases going down column 1 from Nb to W. If the absolute value of S_{12} of W were to change by only 0.56, the strain energy restrictions would be violated. It is very likely that changes in S_{12} of W produced by changes in temperature are responsible for the appearance of the β form and also the fact that the ductile-brittle transition temperature of W is the highest of these four elements.

The elastic compliances in some crystallographic directions of interest are shown for these four elements in Table A2. A plausible reason for complete ductility in the Nb-Ta alloy series is based upon the observation that the compliances under tension and shear in important directions have relatively large values for these elements. Further, the margin of fulfillment of the strain energy restrictions on the compliances is comparatively large for both elements.

The alloy series Mo-W is reported[1] to be ductile at all alloy compositions. The plausible reason for this mechanical behavior is based upon the observation that the compliances to tension and shear in important crystallographic directions have about the same values for these elements even though they are relatively small. The closeness of the values of

TABLE A1

Elastic Compliances (cm^2/d) times 10^{13}

Element	S_{11}	$-S_{12}$	S_{44}	$(S_{11}-|S_{12}|)^*$	$(S_{11}+2S_{12})^*$	References
Nb	6.60	2.33	35.0	4.27	1.94	Amer. Inst. Phys. Handbook (1963).
Ta	6.78	2.47	11.98	4.31	1.84	C.S. Hartley, ASD-TDR-63-870 (1963).
Mo	2.8	0.78	9.1	2.02	1.24	M.J. Druyvesteyn, Physica 8, 439 (1941).
W	2.57	0.729	6.60	1.84	1.11	Amer. Inst. Phys. Handbook (1963).

* A measure of fulfillment of elastic strain energy restrictions, i.e.

$S_{11} > |S_{12}|$, $S_{11} + 2S_{12} > 0$ and $S_{44} > 0$.

TABLE A2

Elastic compliances under tension parallel to and
torsion about some crystallographic directions in
units of centimeters^2/dyne multiplied by 10^{13}

Element	ℓ_i	$\frac{1}{E}$ tension in [hkℓ]	$\frac{1}{G}$ torsion about [hkℓ]
Ta	[100]	6.78	12.0
	[110]	5.16	8.73
	[111]	4.67	7.67
	[112]	5.16	8.76
Mo	[100]	2.8	9.1
	[110]	3.3	10.1
	[111]	2.3	10.4
	[112]	3.3	10.1
Nb	[100]	6.60	35.0
	[110]	10.85	43.5
	[111]	12.32	46.4
	[112]	10.85	43.5
W	[100]	2.57	6.60
	[110]	2.57	6.60
	[111]	2.57	6.60
	[112]	2.57	6.60

Mo and W in Table A2 would predict that excursions from random solid solution compositions would be minor as compared to Ta-Mo, Nb-Mo and Nb-W. The observation that W is very nearly elastically isotropic is consistent with the latter predictions. W is anisotropic in the fourth significant figure and is probably anisotropic in the elastic coefficients of higher order. The author would predict that there may be a ductile to brittle transition below 273°K in the W-Mo alloy series because of the small margin of fulfillment of the strain energy restrictions of both W and Mo.

The alloy series Ta-W, Nb-W, Nb-Mo cleave at high alloy compositions. The observation that the directional compliances under tension and shear, as shown in Table A2, differ appreciably for the components of these alloy series strongly suggests that relatively large deviations from random solution composition may occur in these alloys. Furthermore, since the margin of fulfillment of the elastic strain energy restrictions on the compliances is relatively small for Mo and W, it is probable that the margin becomes even smaller by alloying and composition deviations. It is plausible, that in these alloy crystals the change in the elastic compliances produced by the presence of an increasing number of dislocations is sufficient to violate the restrictions on the compliances in some region of the crystal with the result that the crystal becomes energetically unstable and cleaves.

The verification of such predictions would result from a determination of the elastic coefficients and their dependence upon alloying and temperature for these alloys.

APPENDIX II

Calculation of the Impurity Level as a Function of $\rho_{4.2°K}$ for a Ta Single Crystal.

A relationship between the specific electrical resistivity and the volume density of impurities in a metal crystal is desired. Such a relationship can be obtained by appealing to formal transport theory as will be shown below.

The macroscopic electrical conductivity is defined by

$$\underset{\rightarrow}{J} = \sigma \underset{\rightarrow}{E} \qquad \text{Equation 1}$$

$\underset{\rightarrow}{J}$ is the current

$\underset{\rightarrow}{E}$ is the applied electric field

σ is the electrical conductivity, a second rank

tensor which reduces to a scalar in the cubic

system due to symmetry.

The electrical conductivity can be written

$$\sigma = \frac{n e^2 \tau}{m} \qquad \text{Equation 2}$$

where   n is the number of conduction electrons per

unit volume

e is the charge on an electron

m is the electron mass

τ is the relaxation time, i.e., the time inter-

val between electron scattering events.

A mean free path can be defined as the distance traveled between scattering events, e.g.,

$$\Lambda = \tau \bar{v} \text{ or } \tau = \frac{\Lambda}{\bar{v}} \qquad \text{Equation 3}$$

where $\bar{v}$ is the velocity of an electron at the fermi surface. The mean free path is more directly related to the distribution of scattering objects in the solid and would obey a relation such as

$$\Lambda = \frac{1}{Ni \ Q}$$ Equation 4

where Ni is the density per unit volume of point obstacles of total scattering cross section Q. Thus, the electrical conductivity can be written

$$\sigma = \frac{n \ e^2 \ \Lambda}{m \ \bar{v}} = \frac{n \ e^2}{m \ \bar{v} \ Q \ Ni}$$ Equation 5

by using Equations 3 and 4. Rearranging Equation 5, Ni is

$$Ni = \frac{n \ e^2}{m \ \bar{v} \ \sigma \ Q} = \frac{n \ e^2 \rho}{m \ \bar{v} \ Q}$$ Equation 6

since the resistivity $\rho = \frac{1}{\sigma}$.

In order to apply Equation 6 one must be able to obtain a realistic value for Q. It is the evaluation of Q which causes some difficulty, since Q is a function of the difference in the valencies of the matrix and the impurity, the scattering angle and the efficiency of the conduction electrons in screening the point charge introduced in the crystal by the impurity. Ziman[26] has shown that the differential scattering cross section of an impurity can be written

$$Q(\theta) = \left(\frac{2MZ\ell^2}{\hbar^2}\right)^2 \left(\frac{1}{|\ \vec{K} - \vec{K}'\ |^2 + q^2}\right)^2$$ Equation 7

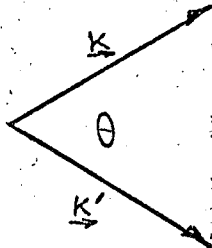The total cross section Q is obtained by integration, e.g.

$$Q = 2\pi \int_0^\pi (1 - \cos \theta) \ Q(\theta) \sin \theta \ d \theta$$

The definitions of the parameters in Equation 7 are as follows:

Z is the difference in valencies of the matrix atoms and the impurity,

θ is the angle between the incident and scattered electron wave

vector, e.g.

from which one obtains the relation $|\underset{\rightarrow}{k} - \underset{\rightarrow}{k'}| = 2 |\underset{\rightarrow}{k}| \sin \frac{\theta}{2}$, $\frac{1}{q}$ is the

screening length, i.e. the range of influence of the perturbing charge

is reduced to about this value due to the screening ability of the

conduction electrons.

At 4.2°K scattering at small values of θ would predominate.

Therefore, since $|\underset{\rightarrow}{k} - \underset{\rightarrow}{k'}|$ appears to higher order in Equation 7 it can

be neglected. Upon performing the integration of Q (θ), the expression

for the total cross section is given by

$$Q = 4\pi \left(\frac{2MZ\ell^2}{\hbar^2} \right)^2 \left(\frac{1}{q^2} \right)^2 \qquad \qquad \text{Equation 8}$$

The values used to compute Q and Ni and their justification, when

necessary, will now be given.

Z is defined as being the difference in valency between the atoms

of the matrix and that of the impurity. When located in an interstitial

site of the crystal, the total ion potential of the impurity should be

used to determine Z.[26] Therefore, interstitial impurities are the

major scatterers at 4.2°K. The most probable interstitial impurities

in Ta are carbon, nitrogen and oxygen. For the ionic potential of

the impurity the value of seven is taken, i.e. the mean between carbon

and oxygen. The question arises as to what is the valency of tantalum.

In the context of electrical transport properties, it is clearly the number of electrons per atom that are involved in the transport process. Therefore, the number of electrons in band VI and the d-subband of Fig. 32 is to be taken as the valency of tantalum. The total area under curve V corresponds to two electrons per atom and likewise for curve VI. For Ta in Fig. 32, band V is about one-quarter filled and band VI is about one-fifth filled, giving the result $(\frac{1}{4})$ 2 plus $(\frac{1}{5})$ 2 or 0.9 electrons per atom which carry the current. The difference in the valencies is thus 6.1 for the case of interstitial impurities. The high value of Z for interstitials indicates that they are very effective scatterers as compared to substitutional impurities where Z is in the range of 1 to 2.

The number of conduction electrons per unit volume in Ta is

$$n = (0.9)(16.6)(\frac{1}{180.88})(6.023 \times 10^{23})$$

$$n = 4.96 \times 10^{22}.$$

The conduction electrons in Ta do not behave as free electrons due to the finite value of the matrix element connecting s and d states. This fact is accounted for by taking for the mass of the electron the mass of a free electron multiplied by a weighting factor. Therefore, since the density of d-states at the fermi surface in tantalum is large and the fermi surface is complex, the effective mass of the conduction electron is about 1.5X(free electron mass) or

$$m^* \approx (1.5)(9.04 \times 10^{-28} \text{ g}) = 1.35 \times 10^{-27} \text{ g}.$$

The specific resistivity of a tantalum crystal at 4.2°K, written

ρ 4.2°K

$\rho_{4.2°K}$, is 1.27×10^{-10} Ω cm from Table I. This value is in mks units and must be changed to esu units for computation. Therefore, $\rho_{4.2°K} = 1.27 \times 10^{-10}$ Ω cm $(\frac{1}{9} \times 10^{-11}) = 1.41 \times 10^{-22}$ stat Ω cm. $\hbar$ is $\frac{h}{2\pi} = 1.04 \times 10^{-27}$ ergs. The velocity of an electron at a spherical fermi surface is given by $\bar{v} = \frac{\sqrt{2E_F}}{m^*}$. The value of the fermi energy E_F is taken from Fig. 32 for Ta and is 5.2 eV. Thus,

$$\bar{v} = \left(\frac{(2)\ (5.2\ \text{eV})\ (1.602 \times 10^{-12}\ \text{erg/eV})}{1.35 \times 10^{-27}\ \text{g}} \right)^{1/2} \quad \text{and}$$

$\bar{v} = 1.10 \times 10^8$ cm/s. The charge of an electron, e, in esu is 4.80×10^{-10}. A plausible[27] value for the screening length $(\frac{1}{q})$ is the atomic radius. In Ta, $(\frac{1}{q})$ is 1.43×10^{-8} cm. Using the values given above in Equation 8, the total scattering cross section is found to be $Q = 6.50 \times 10^{-14}$ cm^2. Substituting the computed value of Q and the values for the other parameters in Equation 6 one obtains for Ni, the density of scatterers per unit volume of crystal, $Ni = 1.67 \times 10^{14}$. By dividing Ni by the number of atoms per unit volume one obtains the atomic fraction of scatters, e.g. $\frac{1.67 \times 10^{14}}{5.55 \times 10^{22}} = 3.01 \times 10^{-9}$, which corresponds to three impurity atoms for every 10^9 matrix atoms. More figuratively, this impurity level corresponds to three impurity atoms contained in a cube of matrix atoms of side 10^3 atomic diameters. A short calculation using the atomic volume of tantalum shows that the distance between impurities is about 2000 Å. Although this is an order of magnitude calculation, the value obtained is a maximum since the contribution to the resistivity

16. Ibid, p. 54.

17. H. Röhl, Ann. Physik., $\underline{16}$, 887 (1933).

18. W. Koster and W. Rauscher, Z. Metallkunde, $\underline{39}$, 111 (1948).

19. J. Friedel, Dislocations, (Pergamon Press, London 1964) Ch. XII.

20. Ibid, p. 234.

21. N. F. Mott, Proc. Roy. Soc. A, $\underline{153}$, 699 (1936).

         Proc. Roy. Soc. A, $\underline{156}$, 368 (1936).

22. J. M. Ziman, Electrons and Phonons, (Oxford University Press,

         London, Second Edition, 1962) pp. 376-382.

23. M. F. Manning and M. I. Chodorow, Phys. Rev. $\underline{56}$, 787 (1939).

24. A. H. Wilson, The Theory of Metals, (Cambridge University Press,

         London, Second Edition, 1953) p. 87.

25. N. F. Mott and H. Jones, The Theory of the Properties of Metals

         and Alloys, (Dover Publications, Inc., first published 1936

         by Clarendon Press, Oxford, England) pp. 243-247.

26. J. M. Ziman, Electrons and Phonons, (Oxford University Press,

         London, Second Edition, 1962) pp. 223-228.

27. Ibid, pp. 161-170.